Master's Thesis

Shelving spectroscopy of a UV transition in Dysprosium atoms

presented by

Viraatt Sai Vishwakarma Anasuri

October 25, 2019

Principal Adviser: Prof. Dr. Tilman Pfau

Second Adviser: Prof. Dr. Jörg Wrachtrup

5. Physikalisches Institut
Universität Stuttgart

Declaration

I herewith declare that I have written this thesis independently. I have used no other sources except for the ones cited in this thesis. All statements used from external sources either literally or in content are clearly marked as such. I assure that the thesis has neither completely nor in part been used in a different examination and that the provided electronic version of this thesis is identical to the printed ones.

Stuttgart, 25.10.2019

Viraatt Sai Vishwakarma
Anasuri

Abstract

The subject of this thesis is to characterize a UV transition in Dysprosium at 359 nm, which is an essential preliminary step for the realization of a predicted magic wavelength for the clock transition at 1001 nm to the realize the goal of single-site resolution using quantum gas microscope for ultracold Dy atoms in an UV lattice.
This is achieved by performing laser spectroscopy on atomic Dysprosium in a high vacuum chamber. The UV transition is a relatively weak transition and given that it is predicted to involve a doubly excited state, the detection is done using shelving spectroscopy. By obtaining a high resolution shelving spectrum, the isotopes shifts and the excited state hyperfine constants are obtained. A King plot analysis is performed to estimate the electronic nature of the excited state. An upper bound for the natural linewidth of the transition is estimated from the decay of the excited state atoms.

Contents

1 Introduction

The curiosity to explore nature of mater around us has been an underlying driving force for many research directions. In this quest, understanding new states of matter has been of prime importance for not just intellectual purpose but to eventually find possible applications as well. The experimental observation of Bose-Einstein condensates (BECs) in 1995 [1, 2] and degenerate Fermi gases in 1999 [3] from ultracold dilute gases of alkali atoms paved the way for exploring new states of matter in the quantum regime. Due to a high degree of control of their internal and external degrees of freedom offered by these quantum gases, they form an excellent platform to study quantum effects. Some of the many fascinating phenomena observed in these systems are matter-wave interference [4], vortices in a rotating BEC [5] and superfluidity in strongly interacting Fermi gases [6]. Ultracold atoms in periodic optical lattice potentials provide a platform to mimic solid state physics and is one of the platforms to study quantum simulation [7]. Few examples are the superfluid to Mott insulator transition [8] and the manifestation of Anderson localization [9]. Combined with a quantum gas microscope, which allows imaging and manipulation of single atoms, these systems form an exceptional tool to study strongly correlated many-body physics on a single atom level [10]. Ultracold atoms in optical lattices offer several advantages like the ability to address single-sites, lower energy scales involved and the high degree of control. Ultracold quantum gases are isolated sytems featuring a unique tool to extensively manipulate the internal interactions in the system. The dominant interaction in quantum gases of alkali atoms is short-range isotropic contact interaction, which can be tuned via Feshbach resonances by means of an external magnetic field [11]. The ability to control the interactions in quantum gases hold a key to explore novel quantum states.

The pioneering experiment on achieving a BEC of Chromium atoms in our lab in 2004 [12] marked the beginning of a new field of dipolar quantum gases. The relatively large magnetic dipole moment of Chromium gives rise to a non-vanishing magnetic dipole dipole interaction (DDI) in the BEC [13], which is long-range and anisotropic, in contrast to the short-range isotropic contact interaction. The DDI in dipolar quantum gases is responsible for many novel phenomena. Some of the manifestations of DDI that have been intially observed were magnetostriction [14],

d-wave collapse of the BEC [15] and demagnetization cooling [16]. With the arrival of the quantum gases of Dysprosium [17] and Erbium [18], whose magnetic dipole moment is larger, stronger manifestation of DDI became available. This resulted in observing a long-lived novel state of matter namely, the dipolar quantum droplets, stabilized by quantum fluctuations [19]. These droplets, as the name suggests have properties closely related to a liquid like low compressibility and saturation of peak density. Although the droplets posses a density which is several orders of magnitude smaller than any liquid, it can also exhibit a self-bound behavior [20]. Another interesting manifestation of DDI in dipolar quantum gases is the existence of a roton-maxon character of the excitation spectrum [21], which has been studied experimentally [22]. Due to this roton-like dispersion relation, dipolar quantum gases are a potential prospect to realize a supersolid, which is a quantum mechanical state of matter featuring a solid-like periodic density modulation together with dissipationless superfluid flow. Intial studies of the observed transient dipolar supersolid properties [23–25] provided a starting point to later demonstrate the inherent properties of density modulation and superfluid nature, which were studied and verified by looking at interference effects and collective excitations [26–28].

The long-range anisotropic interaction offered by dipolar atoms combined with the ability to image and manipulate single atoms in lattice potentials offered by a quantum gas microscope is a powerful platform to study strongly correlated many-body phenomena and exotic phases of matter. Hence a quantum gas microscope for Dy is planned to be built, in which ultracold Dysprosium atoms will be trapped in lattice potentials to achieve single-site addressability. In order to increase the dipolar interaction [29], smaller lattice periods are desirable and hence a lattice in the ultraviolet (UV) regime is chosen. A high numerical aperture (NA) microscope objective, based on a solid-immersion lens approach is used to increase the NA of the whole imaging system. But the estimated final optical resolution of this system is not enough to achieve single-site resolution when imaging the atoms in the UV lattice. Hence to achieve single-site resolution, a new super-resolution imaging technique beyond the diffraction limit called the shelving technique, inspired by biological imaging techniques like "Stochastic optical reconstruction microscopy" (STORM), is planned. The idea of this shelving technique is to image the distribution of the atoms in parts, after shelving the other atoms that are not being imaged, to a long-lived excited state. Parts of the distribution of atoms that are imaged are then reconstructed to achieve single-site resolution. For the shelving technique, a long-lived excited clock state in Dysprosium at 1001 nm shall be used [30]. However, for two different states of the atom, optical trapping induces a shift in the atomic transition frequencies and introduces inhomogenity in the transition associated with the spatial profile of the trapping potential [31]. This shift arises from the different frequency dependent ac polarizabilities of the two different states. A solution to this problem is to find a magic wavelength at which the ground state and the excited state have the same polarizability such that effectively the shift can be neglected. Hence, a prerequisite to implement such an imaging technique is a magic wavelength for the ground and excited state of the trapped atoms. Theoretical calculations show a prospect for a magic wavelength for the ground state and the excited state corresponding to the 1001 nm transition in the UV regime around 360 nm. However, the first step to experimentally verify this prediction is an extensive characterization of the ground state transition in the UV regime near the expected magic wavelength. The next step is to then find the optimal magic wavelength by extensive spectroscopy of the clock transition with ultracold atoms.

In this thesis, we present the extensive characterization of the UV transition at 359 nm. The UV transition at 359 nm in Dy was reported to have a natural linewidth of approximately 52 kHz [32] but there is no further characterization of the transition. Theoretical estimations predict the excited state configuration of the UV transition to be a doubly excited state [33], where transition between the ground state and the excited state involves two electrons. This makes the transition rather weak to detect using conventional spectroscopic techniques. Hence we employ the so called shelving spectroscopy as an amplification scheme to detect such a weak transition via a strong transition as the monitor [34, 35]. We choose the strong 421 nm transition in Dy, which has a natural linewidth of approximately 32 MHz [36] as the monitor to detect the UV transition. The work presented in this thesis is organized as follows:

Chapter 2 gives an overview of the investigation system i.e. atomic Dysprosium. Starting with the general properties of Dysprosium relevant to spectroscopy, like vapor pressure and natural abundance, we move on to discuss the atomic energy levels including the hyperfine structure, electronic configurations of the ground state and the excited states corresponding to different transitions and the isotope shifts for transitions between atomic levels for different isotopes.

Chapter 3 describes the theoretical aspects of atom light interaction necessary to understand the results presented in this work. The discussion begins with a simple model of two level atom and the effects of its interaction with laser light, described using optical Bloch equations. We then describe the phenomenon of absorption, the spectral line shape and line broadening effects. A discussion on the aspects of laser spectroscopy including an overview of the conventional techniques used is followed by estimating the response of shelving spectroscopy.

Chapter 4 describes the apparatus used to implement shelving spectroscopy. We start with the characterization of the laser set-up and the calibration of the frequency scan. To conclude, we discuss the spectroscopy set-up which includes a high vacuum chamber with an atomic beam.

Chapter 5 finally focuses on characterization of the UV transition obtained by shelving spectroscopy. Beginning with the emphasis on the need for shelving spectroscopy, we discuss the success of this method by obtaining a spectrum. As a part of the characterization of the transition, we measure the isotope shifts and perform a King plot analysis to estimate the electronic nature of the excited state. We also extract the excited state hyperfine constants for both the fermionic isotopes and the hyperfine trnasitions frequencies. We then discuss an estimate to the upper bound of the natural linewidth of the transition and describe the effect of changing control parameters on the shelving spectrum. Finally we discuss the uncertainties in our measurements.

The thesis comes to an end by concluding the results and giving an outlook for the improvement of the current experiment and future prospects in chapter 6.

2 Dysprosium

This chapter describes relevant properties of the system under investigation i.e. atomic Dysprosium, especially with regard to laser spectroscopy. The chapter starts with a few general properties like the vapor pressure and isotopes of Dysprosium. Using laser spectroscopy, we investigate transitions between atomic energy levels. Section 2.2 starts with the description of the electronic configuration for the ground state and the excited states corresponding to a few relevant transitions. Further, we present the various contributions resulting in the hyperfine structure of the energy levels. The hyperfine structure lifts the degeneracy of energy levels and the transitions between the hyperfine states can be addressed using spectroscopy. The chapter concludes with a discussion on the factors responsible for shifts in the transition frequency for different isotopes and the King plot analysis. Isotope shift contributions obtained using a King plot analysis contain information regarding the electronic nature of the transition.

2.1 General properties

The element Dysprosium (Dy) has an atomic number of 66 and belongs to the lanthanide series in the periodic table. Dy is solid at room temperature and a melting point of $T = 1412\,°\mathrm{C}$ [37]. The most abundant stable isotopes of Dy and some of their properties are listed in Table 2.1.

One of the properties of interest in laser spectroscopy of atoms is the vapor pressure. The vapor pressure $P(T)$ of Dy, as a function of temperature T, expressed in millibar is given by the Antoine equation,

$$P(T) = 10^{a-\frac{b}{c+T}}, \tag{2.1}$$

where a,b,c are empirical constants, specific to an element [38]. For Dy, the empirical constants are $a = 6.92, b = 10169.5$ and $c = 36.94$. The resulting vapor pressure as a function of temperature is shown in Figure 2.1.

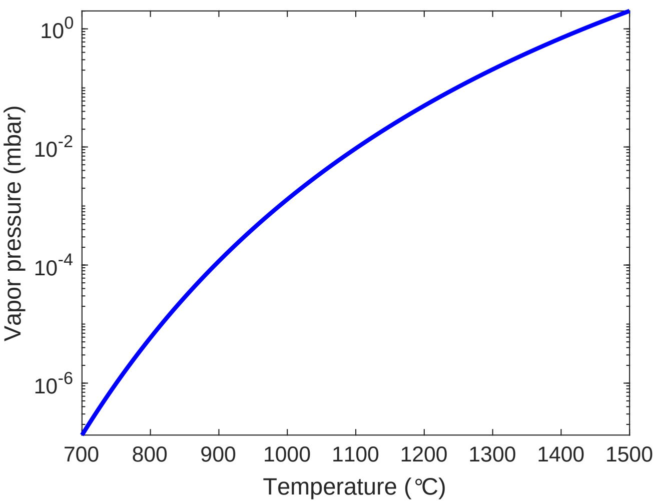

Figure 2.1: Vapor pressure of atomic Dy expressed as a function of temperature

Table 2.1: Properties of the most abundant stable isotopes of Dy [39].

Isotope	Mass(amu)	Natural abundance (%)	Statistics
^{160}Dy	159.93	2.34	boson
^{161}Dy	160.93	18.91	fermion
^{162}Dy	161.93	25.51	boson
^{166}Dy	162.93	24.90	fermion
^{164}Dy	163.93	28.18	boson

2.2 Atomic energy levels

2.2.1 Electronic configuration

From the theory of quantum mechanics, it is known that the energy levels of an atom are quantized and the wavefunction of the electrons in an atom can be described by appropriate quantum numbers. According to Madelung's rule, Dy has a ground state electronic configuration of $[\mathrm{Xe}]4f^{10}6s^2$, and has an open $4f$ shell. Using Hund's rules, we can obtain the ground state configuration. The four unpaired f shell electrons lead to an orbital angular momentum represented by a quatum number $L = 6$ and the total electronic spin represented by a quantum number $S = 2$. The orbital angular momentum can couple to the total spin via magnetic interaction termed as spin-orbit coupling leading to a total angular momentum represented by quanutm number $\mathbf{J}$, responsible for the fine structure

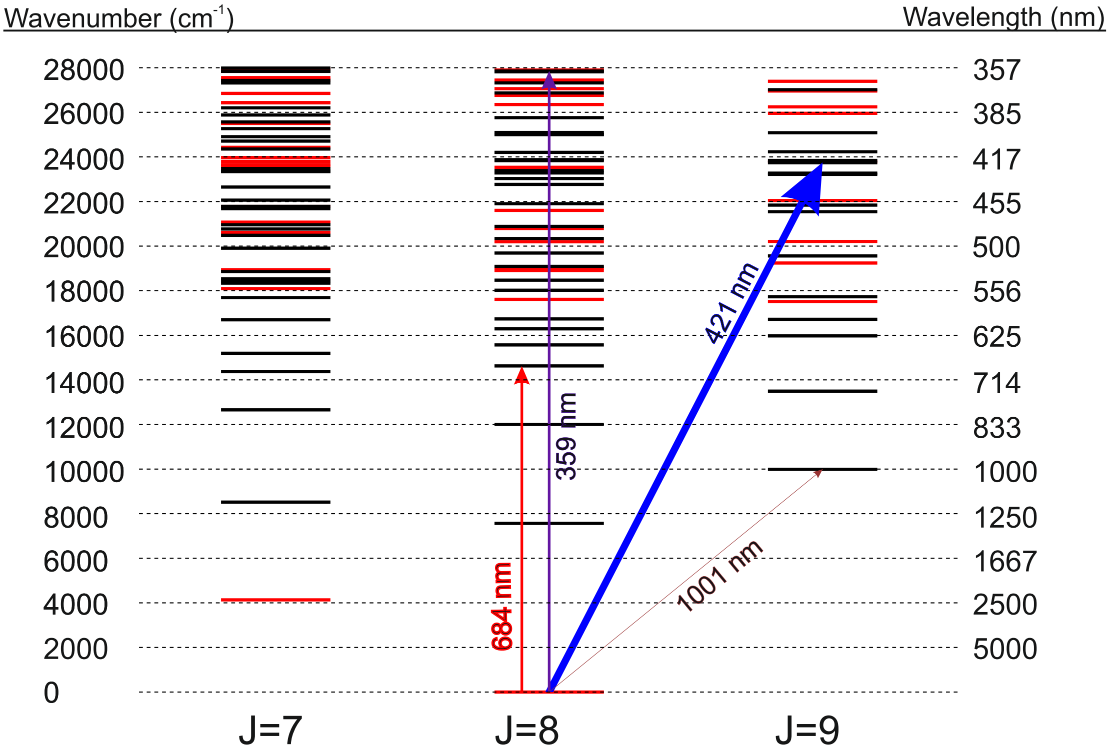

Figure 2.2: Level structure of Dy and a few relevant transitions. The levels with odd (even) parity are shown in black (red). The linewidth of the transition is proportional to the thickness of the represented lines

energy splitting of atomic levels [40]. For the ground state of Dy, the total angular momentum is given by $|\mathbf{J}| = |L + S| = 8$. In the term symbol notation i.e. $^{2S+1}L_J$, the electronic configuration of the ground state of Dy is written as $^5I_8$.
Another important quantity is the parity of a state given by $\pi = -1^l$, where l is the azimuthal quantum number. Orbitals p,f,... with $l = 1, 3, ...$ have an odd parity. An atomic state has an odd parity if an odd number of electrons occupy these orbitals. Ground state of Dy has an even parity. A large angular momentum of Dy results in a high magnetic moment of $\mu_m = 9.93\,\mu_B$. Together with the element Terbium, Dy has the highest magnetic moment of all stable elements. Dy exhibits a rich and complex level structure due to the submerged shell configuration. A part of the level structure of Dy with a few relevant transitions are shown in Figure 2.2 [41]. The characteristics of a few transition are listed below :

- The 421 nm transition is from the $4f^{10}6s^2(^5I_8)$ ground state to the $4f^10(^5I_8)6s6p(^1P^o_1)$ excited state. The excited state has an odd parity and the transition is characterized by an outer shell transition as one $6s$ electron is excited to $6p$ state. This is the strongest recorded cycling transition of atomic Dysprosium with a linewidth $\Gamma = 32.2\,\mathrm{MHz}$ and an upper limit to the branching ratio of $1 : 10^5$ [42].

- The 684 nm transition is from $4f^{10}6s^2(^5\mathrm{I}_8) \rightarrow 4f^9(^6\mathrm{H}^\mathrm{o})5d6s^2(^5\mathrm{I}^\mathrm{o}_8)$. The excited state has an odd parity and the transition is characterized by an inner shell transition as one $4f$ electron is excited to $5d$ state. The linewidth was measured as $\Gamma = 95\,\mathrm{kHz}$. The upper bound to the branching ratio was measured to be $1 : 10^2$. [43]

- The 1001 nm transition is from $4f^{10}6s^2(^5\mathrm{I}_8) \rightarrow 4f^9(^6\mathrm{H}^\mathrm{o})5d6s^2(^7\mathrm{I}^\mathrm{o}_9)$. The excited state has an odd parity and the transition is characterized by an inner shell transition as one $4f$ electron is excited to $5d$ state. The linewidth was theoretically predicted to be $\Gamma = 53\,\mathrm{Hz}$ [30, 44].

In this work, we are going to study a UV transition in Dy at $\lambda = 358.946\,\mathrm{nm}$ [32] in air. The Einstein A coefficient was measured to be $0.326\,\mathrm{s}^{-1}$ and hence the linewidth $\Gamma = A/2\pi \approx 51.9$ kHz [32].

- This is a $4f^{10}6s^2(^5\mathrm{I}_8) \rightarrow 4f^9(^6\mathrm{H}^\mathrm{o})5d^2(^3\mathrm{P})(^8\mathrm{I}^\mathrm{o})6s$ transition [45][1]. The excited state has an odd parity. This transition, unlike the two previously discussed transitions, involves two electrons-one $4f$ electron and one $6s$ electron in the ground state are involved in the transition to $5d^2$ excited state. Such an excited state is the so-called doubly excited state and is a manifestation of the electron-electron interaction [46–49]. A mean-field (Hartree-Fock) description assumes that the electrons evolve independently in a central potential and neglects the electron-electron interaction. In such a model, the independent-particle quantum numbers prove inappropriate to characterize the doubly excited states. Hence to treat the electron correlations, a description beyond the mean-field is required. Doubly excited states were observed in a seminal experiment by Madden and Codling (1963) [50] who observed a strong asymmetric absorption profile of helium using synchrotron radiation. In the case of helium, the energy of this doubly excited state is beyond the first ionization limit and hence caused an ionization of the atom. Doubly excited states in such a case are called autoionizing states. An understanding of the origin of the celebrates asymmetric profile (known as Fano resonances) was provided by Fano [51], who justified that it involves interference between a discrete state and one belonging to a continuum [52]. Autoionizing states were

---

[1] NIST atomic spectra database `https://www.nist.gov/pml/atomic-spectra-database`

also discovered in the alkaline earth atoms by UV absorption spectroscopy, using multi step laser excitation [53]. In the case of Dysprosium, the first ionization potential is at 47901.7(6) cm^{-1} [54], which is well above the UV transition at 27851.43 cm^{-1}, and hence is not an autoionizing state. The consequences on the spectral properties of such a transition to a doubly excited state within the ionization limit is to be investigated.

2.2.2 Hyperfine structure of energy levels

The nucleus, owing to its internal structure has an angular momentum represented by the quantum numer I, also called the nuclear spin. For Dy, unlike the bosonic isotopes, the fermionic isotopes posses a nuclear spin of $I = 5/2$. The interaction of the electronic charge density with the nuclear spin I results in a total angular momentum, represented by a quantum number $\mathbf{F} = |I - J|, ..., |I + J|$. This leads to a further splitting of energy levels called the hyperfine splitting. Hyperfine splitting has its origin in the interaction of higher order electromagnetic multipoles of the nucleus, with the electromagnetic field produced by the electron at the nucleus. By the symmetry arguments of parity and time-reversal, and by neglecting higher order multipole moments we can confine our discussion to the two lowest orders of this interaction. These are the interaction of the nuclear magnetic dipole moment and the nuclear electric quadrupole moment with the electromagnetic field produced by the electrons [55]. These interactions can be treated using perturbation theory and the full calculations can be found in [55]. Here, we shall follow a qualitative overview and discuss the results.

Magnetic dipole interaction

The interaction Hamiltonian of a nuclear magnetic moment μ_{I} interacting with the magnetic field B_{el} produced by electrons is given by

$$H_{\mathrm{MD}} = -\mu_{\mathrm{I}}.B_{\mathrm{el}} \tag{2.2}$$

This assumes that μ_{I} and B_{el} are independent in their nature[2]. For an isolated energy level with quantum number J, it follows that $\mu_I \propto I$ and can be expressed as

$$\mu_{\mathrm{I}} = g_{\mathrm{I}}\mu_{\mathrm{N}}I, \tag{2.3}$$

---

[2] Analogous to electric dipole, we assume that μ_{I} depends only on the co-ordinates of the nucleus and B_{el} depends only on the electronic co-ordinates.

where, g_I is the nuclear g factor and μ_N is the nuclear magneton. As an interesting consequence, in contrast to the magnetic moment of electron[3], nuclear magnetic moment can be parallel or anti-parallel to I meaning that g_I can be positive or negative depending on how magnetic moments of protons and neutrons couple inside the nucleus [56]. Within our assumptions, $B_\mathrm{el} \propto J$ and hence the Hamiltonian can be written as

$$H_\mathrm{MD} = A\,\mathbf{I}\cdot\mathbf{J}, \tag{2.4}$$

where A is the magnetic hyperfine coupling constant, $A \propto \mu_\mathrm{I}/I, B_\mathrm{el}$ and is determined experimentally. The energy splitting can be calculated by estimating B_{el} and by calculating the expectation value of the Hamiltonian and is given by,

$$\Delta E_\mathrm{MD} = \frac{A}{2}(F(F+1) - I(I+1) - J(J+1)) = A\,K. \tag{2.5}$$

This shows us that there is a splitting of the hyperfine levels labeled by F, which lifts the $(2F+1)$-fold degeneracy. The transitions between different F levels follow the electric dipole selection rules i.e $\Delta F = 0, \pm 1$ & $F = 0 \nrightarrow F = 0$. The magnetic hyperfine constant A gives the splitting between the levels and it follows that,

$$\Delta E_\mathrm{MD}(F) - \Delta E_\mathrm{MD}(F-1) = AF. \tag{2.6}$$

This is the so called interval rule which states that the energy splitting between adjacent levels is proportional to the larger F of the two levels.

So far, we have only considered a point sized nucleus. One consequence on the hyperfine structure due to the finite size of nucleus is the so called Bohr-Weisskopf effect [57], leading to a hyperfine anomaly. One would expect that, for two isotopes, the ratio of A factors is given by the ratio of their respective μ_I/I. However, it is observed that $A_1/A_2 = (\mu_I/I)_1/(\mu_I/I)_2\,(1+\Delta)$, where Δ is the hyperfine structure anomaly parameter for the isotopes 1 and 2 in the same energy level. For the isotopes of Dy, assuming that there is no hyperfine anomaly in the ground state [58], the anomaly parameter for the excited state can be approximated as

$$\Delta \approx \frac{A_e(163)}{A_e(161)}\frac{A_g(161)}{A_g(163)} - 1, \tag{2.7}$$

where A_e and A_g represent the excited state and ground state constants respectively of the corresponding isotope. These values are to be determined experimentally. When the measured ratio of A_e values for the isotopes is close to the ratio of A_g values, $\Delta \approx 0$ and the anomaly is suppressed.

---

[3] $\mu_\mathrm{J} = -g_\mathrm{J}\mu_\mathrm{B}J$

Electric quadrupole interaction

The electrostatic interaction between a proton at position $\mathbf{r_n}$ and an electron at position $\mathbf{r_e}$ is given by,

$$H_E = \frac{-e^2}{4\pi\epsilon_0|\mathbf{r_e} - \mathbf{r_n}|} \tag{2.8}$$

The total electrostatic interaction between the nucleus and the electron can be obtained by summing up over all the protons. We have so far considered that the nucleus is a point charge ($r_n \ll r_e$) and hence has a spherically symmetric charge distribution. Deviations from its spherical symmetry can be introduced by attributing multipole electric moments to the nucleus. Assuming separation of the coordinates[4], the Hamiltonian can be expanded in powers of r_n/r_e and is written in terms of spherical harmonics. Calculating the expectation value of the Hamiltonian gives the electric quadrupole energy splitting as

$$\Delta E_{EQ} = B\frac{\frac{3}{2}K(2K+1) - I(I+1)J(J+1)}{2I(2I-1)J(2J-1)}, \tag{2.9}$$

where B has to be determined experimentally and

$$K = \frac{1}{2}(F(F+1) - J(J+1) - I(I+1)) \tag{2.10}$$

The total hyperfine splitting is therefore obtained by summing up both the contributions and is given as

$$\Delta E_{HFS} = \Delta E_{MD} + \Delta E_{EQ} = AK + B\frac{\frac{3}{2}K(2K+1) - I(I+1)J(J+1)}{2I(2I-1)J(2J-1)} \tag{2.11}$$

The dependence of the electric quadrupole interaction on F is different from that of the magnetic dipole interaction. Hence the electric quadrupole interaction results in a departure from the interval rule. The hyperfine structure for the ground state of the two stable abundant fermionic isotopes of Dysprosium calculated using equation 2.11 and taking the values of A_g, B_g from [59], are shown in Figure 2.3.

The hyperfine structure for ^{161}Dy in ground state is inverted compared to ^{163}Dy which is due to the fact that A has a negative sign [59] and this reveals information regarding the internal structure of the nucleus as discussed according to equation 2.3.

---

[4] Assuming that electronic and nuclear coordinates are independent of each other by considering $r_e > r_n$.

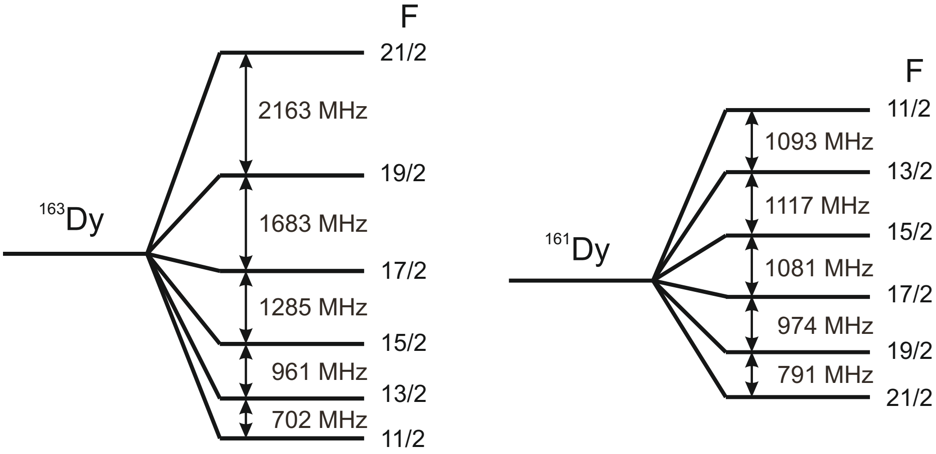

FIGURE 2.3: The ground state hyperfine structure for ^{163}Dy and ^{161}Dy

2.2.3 Isotope shift for transitions

So far, we have discussed the energy levels and their hyperfine structure. Following the selection rules, transitions among the energy levels can be driven with the appropriate incident radiation. It is observed that the transition frequency between two energy levels is different for different isotopes of the element. This difference is called the isotope shift for a transition between two energy levels. The isotope shift is the difference in the transition frequency with respect to the transition frequency of a reference isotope. The nuclear contribution to the isotope shit arises from the finite mass and extended charge density distribution of the nucleus. Like in the previous section, we are going to present a qualitative overview and the full calculations can be found in [55, 60].

Mass shift

In the Bohr model of an atom, assuming an infinitely heavy nucleus, the energy of atomic levels is proportional to the mass of an electron m_e. The effects of a nucleus with finite mass M, are accounted for, by introducing a reduced mass for the electron $m = \frac{m_e M}{m_e + M}$. This treatment should be extended to the Schrödinger equation to account for the so called normal mass shift (NMS). For two isotopes with atomic masses A_1,A_2 ($A_2 > A_1$), the frequency difference due to normal mass shift for a transition i is givenby

$$\Delta\nu_{i\,\mathrm{NMS}}^{A_2,A_1} = M_{i\,\mathrm{NMS}} \frac{A_2 - A_1}{A_1 A_2}, \tag{2.12}$$

where the NMS factor

$$M_{i\,\mathrm{NMS}} = m_e \nu_i / m_p = \nu_i / 1836.15 \tag{2.13}$$

and ν_i is the transition frequency. There is another contribution to the mass shift coming from the correlation between the motion between pair of electrons called the specific mass shift (SMS) given by

$$\Delta\nu_{i\,\mathrm{SMS}}^{A_2,A_1} = M_{i\,\mathrm{SMS}} \frac{A_2 - A_1}{A_1 A_2}, \tag{2.14}$$

where $M_{i\,\mathrm{SMS}}$ is the SMS factor. The calculation of SMS is challenging, especially for many-electron atoms as it involves correlation between motion of pair of electrons. The success of the calculation depends on the accuracy of the many-electron wave function i.e. for 66 electrons in Dy.

Field shift

Isotope shift arising from a variation of the charge density distribution of the nucleus of different isotopes is called the field shift (FS). The measurement of field shifts gives the information about the size and shape of a nucleus as a function of its neutron number. The electric monopole interaction between nucleus and the electron adopted for a finite sized nucleus gives a departure from pure Coulomb interaction. As a probe for the nuclear electric charge distribution, the s-electron density at the nucleus is evaluated[5], which requires a relativistic approach. The field shift can be calculated as

$$\Delta\nu_{i\,\mathrm{FS}}^{A_2,A_1} = E_i f(Z) \lambda^{A_2,A_1}, \tag{2.15}$$

where E_i is the parameter related to the non-relativistic electron charge density at the nucleus, $f(Z)$ is the relativistic correction factor, and λ^{A_2,A_1} is the parameter related to the change in the mean-square nuclear charge radius. The calculation of FS depends on the accuracy of the electronic charge distribution at the nucleus and information regarding the difference in nuclear charge distributions for the isotopes. The observed isotope shift is to a very good approximation, the sum of NMS, SMS and FS.

King plot

As we have discussed, different contributions to the isotope shift contain intrinsic information regarding the nuclear structure and its effects on the transition between

---

[5] Because the charge density of s-electrons in non-vanishing at the nucleus. FS can only be observed for transitions involving electrons with non-vanishing charge density at the nucleus

Table 2.2: Isotope shits $\Delta\nu_{IS}$ with respect to the transition of the ^{164}Dy and hyperfine coefficients A,B for the ground-state (G.S.) and for the excited-states (E.S.) of the 421 nm and 684 nm transition.

State	Isotope	A [MHz]	B [MHz]	ν_{IS} [MHz]	Refs.
	^{161}Dy	-116.2322	1091.5748		
G.S.	^{163}Dy	162.7543	1153.8684		[59]
	^{161}Dy	-86.90	1747.4	1635	
E.S. (421 nm)	^{163}Dy	121.62	1844.9	616.3	[36]
	^{161}Dy	-108.84	2251	-2099	
E.S. (684 nm)	^{163}Dy	152.56	2357	-823	[43]

the electronic states. The overall isotope shifts for a transition can be measured using spectroscopy but, to investigate the various contributions to the measured isotope shifts, we require the isotope shifts of another transition. For two transitions i and j, it follows that [61]

$$\Delta\nu_i^{A_2,A_1} = \frac{E_i}{E_j}\left(\Delta\nu_j^{A_2,A_1} - \Delta\nu_{j\,\text{MS}}^{A_2,A_1}\right) + \Delta\nu_{i\,\text{MS}}^{A_2,A_1}, \tag{2.16}$$

where $\Delta\nu_{\text{MS}}^{A_2,A_1} = \Delta\nu_{\text{NMS}}^{A_2,A_1} + \Delta\nu_{\text{SMS}}^{A_2,A_1}$. This implies that for two different transitions i and j, the plotted isotope shifts for pairs of isotopes A_1 and A_2 would be linear. The slope of this line would give the ratio of field shift parameters $\frac{E_i}{E_j}$ and the intercept allows to calculate the SMS. This method of estimating the SMS and FS by plotting the measured isotopes shifts was introduced by W.H. King [62] and such a plot is called King plot. To calculate the SMS of a transition, the SMS of a reference transition should be known and typically the SMS is difficult to calculate as it depends on the accuracy of the many-electron wave function. However, the SMS can be estimated using a semi-emperical relation for a pure $ns^2 \rightarrow nsnp$ transition [61] as $\Delta\nu_{i\,\text{SMS}}^{A_2,A_1} \approx (0 \pm 0.5)\Delta\nu_{i\,\text{NMS}}^{A_2,A_1}$. Bauche (1969) showed using Hartree-Fock calculations that large negative SMS arise in transition of the type $4f^n - 4f^{n+1}$ [62].

For a $\Delta F = 0$ transition between ground state g and excited state e, the frequency difference [6] is given by

$$\Delta\nu = (A_e - A_g)K + (B_e - B_g)\frac{\frac{3}{2}K(2K+1) - I(I+1)J(J+1)}{2I(2I-1)J(2J-1)} + \Delta\nu_{\text{IS}}, \tag{2.17}$$

---

[6] All the shifts are represented with respect to the same transition

where $\Delta\nu_{\mathrm{IS}}$ is the isotope shift for the transition to the excited state. The isotope shifts and the hyperfine constants for two transitions are mentioned in Table 2.2.

Deviations of the King plot from linear behavior reveal a wealth of information. The non-linear corrections to the King plot can arise from various factors such as relativistic effects in isotope field shifts, the nuclear polarizability and many body effects among others [63]. These corrections are within the framework of the Standard Model of particle physics. Interestingly, nonlinearities can also arise from the effect of a new hypothetical scalar boson and hence was proposed as a direction towards study of new physics beyond the Standard Model [64].

3 Atom-light interaction

In this chapter, we are going to discuss the theoretical aspects of atom-light interaction in the context of spectroscopy and estimate the relevant quantities with regard to the measurements presented later in this thesis. We start with a simple two-level atom and describe the effects of its interaction with near-resonant light, using optical Bloch equations. We then describe the collective response of several atoms comprising an atomic medium to arrive at the phenomenon of absorption and describe the spectral lineshape of absorption. Section 3.3 describes various factors that contribute to the line broadening of a spectral profile. The next section describes the aspects of implementing spectroscopy. Starting with single beam methods and a brief description of Doppler-free methods, we focus on electron shelving spectroscopy, which is demonstrated in this work as a powerful tool to detect weak transitions. Shelving spectroscopy is an amplification scheme to detect a weak transition using a strong transition as a monitor. To conclude, we describe the general principle of shelving spectroscopy and give an estimate of the expected spectroscopic signal using a similar formalism as that of a two-level atom.

3.1 Two level atom

3.1.1 Atom-light interaction Hamiltonian

In understanding the atom-light interaction, a semi-classical approach is adopted. We consider a classical quasi-monochromatic light field interacting with a quantum mechanically described atom. A further simplification is done when we consider an atom with two discrete energy levels which can be justified as we only consider near resonant transitions and hence the transitions to other levels can be neglected. Assuming the incident radiation to be a coherent laser beam of the form

$$\boldsymbol{E}(t) = \boldsymbol{\epsilon} E_0 \cos(\omega t) = \boldsymbol{\epsilon} \left(E_{ge} e^{i\omega t} + E_{eg} e^{-i\omega t} \right), \tag{3.1}$$

with amplitude E_0, $E_{ge} = E_{eg}^* = \frac{E_0}{2}$, center angular frequency ω and polarization vector $\boldsymbol{\epsilon}$. The Hamiltonian of a non-interacting and unperturbed single atom with

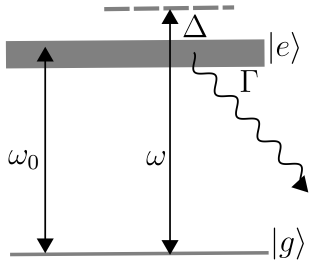

FIGURE 3.1: Atom with ground state $|g\rangle$ and excited state $|e\rangle$, with an energy difference of $\hbar\omega_0$ and with a decay rate of excited state as Γ, interacting with light of frequency ω, detuned by Δ.

a ground state $|g\rangle$ and excited state $|e\rangle$, with corresponding eigenenergies $E_g = \hbar\omega_g$ and $E_e = \hbar\omega_e$, is given by

$$H_A = E_g \, |g\rangle \langle g| + E_e \, |e\rangle \langle e| \, , \tag{3.2}$$

such that $H_A \, |i\rangle = E_i \, |i\rangle$. Assuming that the ground state energy is zero, the bare atomic Hamiltonian can be reduced to $H_A = \hbar\omega_0 \, |e\rangle \langle e|$ and in matrix from is represented as,

$$H_A = \begin{pmatrix} 0 & 0 \\ 0 & \hbar\omega_0 \end{pmatrix} . \tag{3.3}$$

The Hamiltonian describing the interaction between light and the atom, in the dipole approximation is given by [65]

$$H_{int} = -\boldsymbol{d} \cdot \boldsymbol{E} = \begin{pmatrix} 0 & d_{ge}E_{ge} \\ d_{eg}E_{eg} & 0 \end{pmatrix} , \tag{3.4}$$

where $\boldsymbol{d} = e \cdot \boldsymbol{r}$ is the electric dipole moment[1], given by electric charge e times the position $\boldsymbol{r}$. The total Hamiltonian of the atom-light system is then given by,

$$H = H_A + H_{int}. \tag{3.5}$$

The interaction between atom and light renders the interaction Hamiltonian off-diagonal in the atomic states basis and hence the states $|i\rangle$ are no longer the eigenstates of the coupled system.

---

[1] Without loss of generality, it is assumed that $\boldsymbol{d} \, || \, \boldsymbol{\epsilon}$.

3.1.2 Density matrix formalism

A pure quantum state is described by the state vector $|\psi\rangle = \sum_i c_i |i\rangle$, with complex coefficients c_i. To represent an atomic ensemble which is a statistical mixture of different states, a density matrix formalism is needed. A mixed quantum state can be represented by a density matrix ρ given by,

$$\rho = \sum_{i,j} \rho_{ij} |i\rangle \langle j| \,. \tag{3.6}$$

The diagonal terms ρ_{ii} referred to as populations, form a probability distribution and quantify the probability of atom in state $|i\rangle$. The off-diagonal terms ρ_{ij} referred to as coherences, describe the superposition between the states $|i\rangle$ and $|j\rangle$. The density matrix is Hermitian and under the condition that population is conserved, $\mathrm{Tr}(\rho) = 1$. For the case of a two level atom, the density matrix is written as

$$\rho = \begin{pmatrix} \rho_{gg} & \rho_{ge} \\ \rho_{eg} & \rho_{ee} \end{pmatrix} \tag{3.7}$$

3.1.3 Dynamics of the system

The time evolution of the density operator can be obtained from the Schrödinger equation, $i\hbar\partial_t |\psi(t)\rangle = H |\psi(t)\rangle$ and is given by [65]

$$\partial_t \rho(t) = \frac{-i}{\hbar}[H, \rho(t)]. \tag{3.8}$$

This is referred to as the von Neumann equation and it describes the coherent evolution of the system. However, the atoms can undergo several decoherence processes like collisions, self broadening and Doppler broadening among others [66, 67]. Spontaneous emission by the atoms is an important decoherence process which gives a limit to the lifetime of the population in the excited state. In the density matrix formalism, a dechorence process of the system can be included by introducing the Lindblad master equation [68] given by

$$\partial_t \rho(t) = \frac{-i}{\hbar}[H, \rho(t)] + L(\rho(t)), \tag{3.9}$$

where $L(\rho(t))$ is called the Lindblad operator. The Lindblad operator for a decay between two states $|i\rangle$ and $|j\rangle$ at a decay rate Γ_{ij} is expressed as

$$L(\rho) = -\frac{1}{2} \sum_{i,j} \Gamma_{ij} \left(C_{ij}^{\dagger} C_{ij} \rho + \rho C_{ij}^{\dagger} C_{ij} \right) + \sum_{i,j} \Gamma_{ij} C_{ij} \rho C_{ij}^{\dagger}, \tag{3.10}$$

where $C_{ij}^{\dagger} = |i\rangle\langle j| = C_{ji}$ is the transition operator [69, 70]. This form can be extended in a similar way to the dephasing processes [71]. For a two level atom, a decay from excited state $|e\rangle$ to ground state $|g\rangle$ at a rate Γ_{eg} is represented by the Lindblad operator as

$$L = \Gamma_{eg} \begin{pmatrix} \rho_{ee} & -\frac{\rho_{ge}}{2} \\ -\frac{\rho_{eg}}{2} & -\rho_{ee} \end{pmatrix}. \tag{3.11}$$

3.1.4 Rotating frame and rotating wave approximation

To evaluate the total Hamiltonian, a transformation into the co-rotating frame of reference, rotating at the laser frequency ω is needed. This is done using a unitary transformation

$$U = e^{-\frac{iH_L t}{\hbar}} = \begin{pmatrix} 1 & 0 \\ 0 & e^{-i\omega t} \end{pmatrix}, \tag{3.12}$$

where H_L is the Hamiltonian describing the photons in the light field. The density matrix is transformed as

$$\sigma = U^{\dagger}\rho U \qquad \begin{pmatrix} \sigma_{gg} & \sigma_{ge} \\ \sigma_{eg} & \sigma_{ee} \end{pmatrix} = \begin{pmatrix} \rho_{gg} & \rho_{ge}e^{-i\omega t} \\ \rho_{eg}e^{+i\omega t} & \rho_{ee} \end{pmatrix}. \tag{3.13}$$

The transformation for the Hamiltonian is obtained by expressing the time evolution of the transformed density matrix [69] and is expressed as

$$\partial_t \sigma(t) = \frac{-i}{\hbar}[H_{RF}, \sigma] = \frac{-i}{\hbar}[U^{\dagger}HU - i\hbar U^{\dagger}\partial_t U, \sigma(t)]. \tag{3.14}$$

The Hamiltonian in the rotating frame is given by

$$H_{RF} = U^{\dagger}HU - i\hbar U^{\dagger}\partial_t U = \begin{pmatrix} 0 & \frac{-d_{ge}}{2}(E_0 + E_0^{*}e^{-2i\omega t}) \\ \frac{-d_{eg}}{2}(E_0 e^{-2i\omega t} + E_0^{*}) & \hbar(\omega_0 - \omega) \end{pmatrix}. \tag{3.15}$$

In the rotating wave approximation, the terms describing an oscillation at twice the light frequency ω are neglected as they average to zero on the interaction time scale. The Hamiltonian in the rotating frame and using the rotating wave approximation is then expressed as

$$H_{RWA} = \begin{pmatrix} 0 & \frac{\Omega_{ge}}{2} \\ \frac{\Omega_{ge}^{*}}{2} & -\Delta \end{pmatrix}, \tag{3.16}$$

where $\Omega_{i,j} = -\frac{d_{ij} \cdot E_{ij}}{\hbar}$ is referred to as the Rabi frequency which quantifies the strength of the atom-light coupling and $\Delta = \omega - \omega_0$ is called the detuning. Moreover, $\Omega_{ij} = \Omega_{ji}^{*}$. To express the full master equation in the rotating frame, the Lindblad

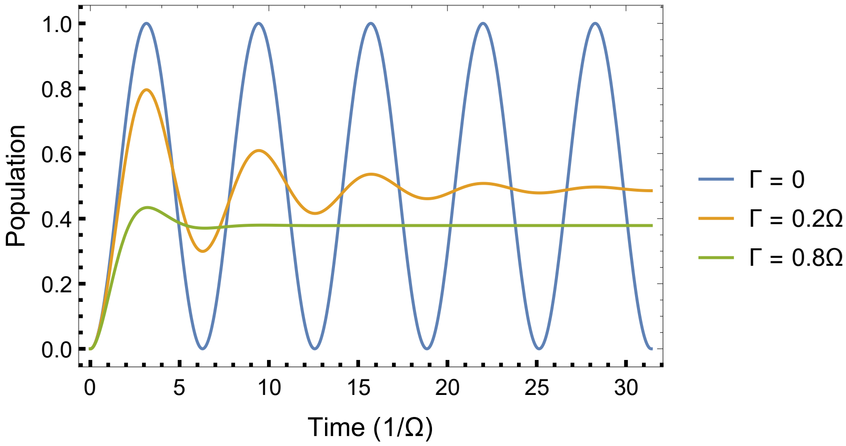

Figure 3.2: Population in the excited state as a function of time in the units of Rabi frequency.

operator has to be transformed into rotating frame analogously [69]. The Lindblad operator in the rotating frame is given by

$$\tilde{L}(\sigma) = \Gamma_{eg} \begin{pmatrix} \sigma_{ee} & -\frac{\sigma_{ge}}{2} \\ -\frac{\sigma_{eg}}{2} & -\sigma_{ee} \end{pmatrix}. \tag{3.17}$$

In the rotating frame of reference, the master equation written in its component form is given by,

$$\dot{\sigma}_{gg} = -\frac{i}{2}(\Omega_{ge}\sigma_{eg} - \Omega^*_{ge}\sigma_{ge}) + \Gamma_{eg}\sigma_{ee} \tag{3.18}$$

$$\dot{\sigma}_{ge} = -\frac{i}{2}(\Omega_{ge}\sigma_{ee} - \Omega_{ge}\sigma_{gg}) - (\frac{\Gamma_{eg}}{2} + i\Delta)\sigma_{ge} \tag{3.19}$$

$$\dot{\sigma}_{eg} = +\frac{i}{2}(\Omega^*_{ge}\sigma_{ee} - \Omega^*_{ge}\sigma_{gg}) - (\frac{\Gamma_{eg}}{2} - i\Delta)\sigma_{eg} \tag{3.20}$$

$$\dot{\sigma}_{ee} = +\frac{i}{2}(\Omega_{ge}\sigma_{eg} - \Omega^*_{ge}\sigma_{ge}) - \Gamma_{eg}\sigma_{ee} \tag{3.21}$$

This set of equations are called the optical Bloch equations which describe a transition in the two level atom caused by near-resonant light, and the subsequent decay due to spontaneous emission. This is a set of three independent equations as, $\dot{\sigma}_{ge} = \dot{\sigma}^*_{eg}$. Assuming that the atom is initially in ground state i.e $\sigma(t \leq 0) = \begin{pmatrix} 1 & 0 \\ 0 & 0 \end{pmatrix}$ this set of eqations can be solved [56], leading to a general solution for the excited state population σ_{22} is shown in Figure 3.2

In the case of no spontaneous decay, the population in the excited state shows undamped oscillation with the characteristic Rabi frequency called the Rabi oscilation. Depending on the strength of the spontaneous decay, on shorter time scale, the

Rabi oscillation is damped. However, for times $t \gg \Gamma^{-1}$, called the steady-state, σ_{22} shows a negligible time dependence and the population reaches a constant value. The population in the excited state, for the steady-state condition is given by

$$\rho_{ee} = \frac{s/2}{1+s}, \tag{3.22}$$

where $s = \frac{2\Omega^2/\Gamma^2}{1+2\Delta^2/\Gamma^2}$ is called the saturation parameter and a strong driving field with $\Omega \to \infty$ tends to equalize the populations in ground and excited state i.e $\rho_{ee} \to 1/2$. As intensity is related to the Rabi frequency as $\frac{I}{I_{sat}} = \frac{2\Omega^2}{\Gamma^2}$ [56],on resonance, the saturation intensity given by

$$I_{sat} = \frac{\pi h c \Gamma}{3\lambda^3}, \tag{3.23}$$

is the minimum intensity that tends to equalize the population.

3.2 Absorption of light

So far we have considered the interaction of a single two-level atom with light. In order to extend the discussion to the collective response of several atoms constituting an atomic medium, like that of an atomic beam or an atomic vapor, we consider the dielectric response of the medium [65, 72]. The polarization density of an atomic medium is given by

$$\boldsymbol{P} = \epsilon_0 \chi \boldsymbol{E} = \boldsymbol{\epsilon} \epsilon_0 \chi \left(E_{ge} e^{i\omega t} + E_{eg} e^{-i\omega t} \right), \tag{3.24}$$

where χ is called the dielectric susceptibility. In a medium where the interactions between atoms are negligible, the polarization density can also be derived from the total dipole moment. This can be obtained by calculating the expectation value of the dipole operator. In the density matrix formalism this can be written as

$$\boldsymbol{P} = N \mathrm{Tr}(\boldsymbol{d} \cdot \boldsymbol{\sigma}) = N(d_{eg} e^{-i\omega t} \sigma_{eg} + d_{ge} e^{i\omega t} \sigma_{ge}), \tag{3.25}$$

where N is the density of atoms. By comparing the time dependent coefficients of equation 3.24 and equation 3.25 and considering the steady state solution of σ_{ge}, the expression for a complex dielectric susceptibility [73] can be derived to be

$$\chi = \frac{N d_{eg}}{\epsilon_0 E_{eg}} \sigma_{ge} = \frac{N d^2}{\epsilon_0 \hbar} \left(\frac{i\Gamma/2 + \Delta}{\Delta^2 + \Gamma^2/4 + \Omega^2/2} \right), \tag{3.26}$$

The real and imaginary part of the susceptibility, which are plotted in Figure 3.3, have distinct interpretations and are related by Kramers-Kronig relations. The

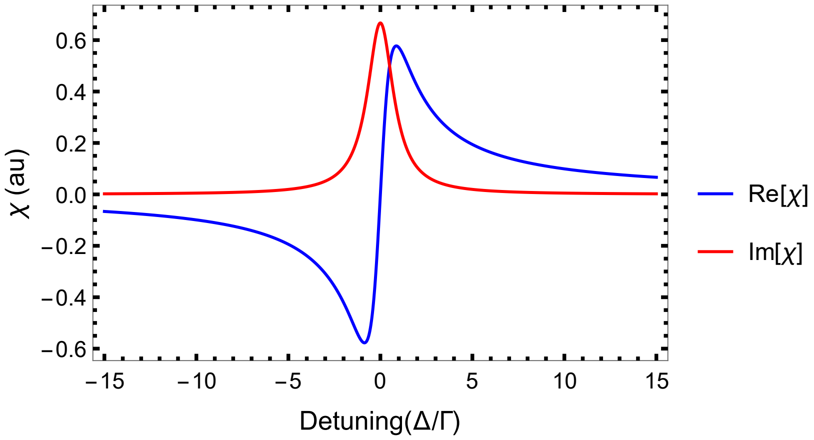

FIGURE 3.3: Real and Imaginary part of the susceptibility plotted for the case of steady state and $\Gamma = \Omega$.

real part exhibits a dispersive feature while the imaginary part gives a Lorentzian absorption profile with full width at half maximum (FWHM) $\Delta\omega$ of,

$$\Delta\omega = \Gamma\sqrt{1 + \frac{2\Omega^2}{\Gamma^2}} = \Gamma\sqrt{1 + \frac{I}{I_{sat}}}. \tag{3.27}$$

It is to be noted that the absorption profile of the medium has a characteristic lineshape with a finite width called the linewidth. For $I \ll I_{sat}$ the FWHM is given by the spontaneous decay rate (also called natural line width) of the transition between the two levels of the atom.

3.3 Line broadening

3.3.1 Homogeneous broadening

In equation 3.11, we introduced a decay coming from the spontaneous emission which affects the populations and the coherences like spontaneous emission. This, as we have seen has a broadening effect on the spectral lineshape. There can also exist other decoherence mechanisms which effect only the coherences like atom-atom collisions. These can be phenomenologically introduced by writing the off-diagonal decay terms in the density matrix (3.11) as $\gamma = \Gamma/2 + \gamma_{dp}$, where γ_{dp} descibes dephasing processes like collisions [73]. Decoherence processes, which affect all atoms alike lead to a homogeneous broadening of the spectral profile for example pressure broadening arising from the collisions of atoms.

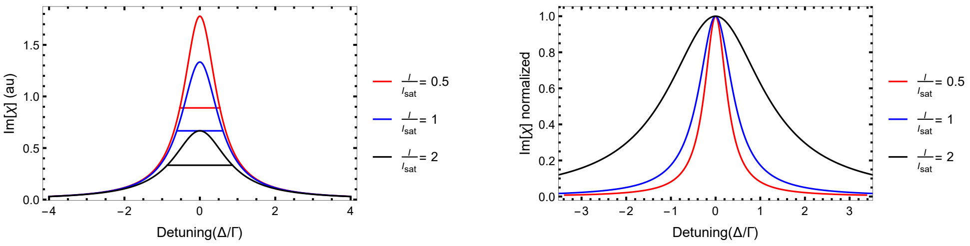

(A) Im[χ] (B) Normalized Im[χ]

FIGURE 3.4: (left)The absorption profile plotted for different intensities as a function of detuning. As the intensity increases, the amplitude decreases and the FWHM increases. (right) Each absorption profile is deliberately normalized to the same value to clearly look at the FWHM.

Power broadening

Power broadening is an example of homogeneous broadening, which we have already come across in equation 3.27. It is to be noted that the linewidth of the absorption profile increases with intensity and is plotted in Figure 3.4. Power broadening occurs because, on resonance, saturation leads to a decrease in absorption but away from resonance, saturation doesn't lead to significant change in absorption. Hence for a fixed density of atoms, this decrease in amplitude should be compenstaed by an increase in the FWHM [56].

3.3.2 In-homogeneous broadening

Doppler broadening

Apart from the homogeneous case, where the effect on all atoms is identical, there also exist broadening mechanisms which affect different classes of atoms in the ensemble differently. An example is Doppler broadening. So far we have only considered atoms at rest but in thermal equilibrium at temperature T, atoms can have different velocities, which are describes by the thermal velocity distribution. In the reference frame of the atom, moving with velocity v, the atoms experience a shifted frequency ω as compared to the rest frame frequency ω_0 given by

$$\omega = \omega_0 + \overrightarrow{\boldsymbol{k}} \cdot \overrightarrow{\boldsymbol{v}}, \tag{3.28}$$

where k is the wave vector of the incident light. It is the component of velocity along the direction of the wave vector that leads to a Doppler shift. The atoms with velocity v, prefer to absorb the light with the detuning

$$\Delta = \omega - \omega_0 = \overrightarrow{\boldsymbol{k}} \cdot \overrightarrow{\boldsymbol{v}}. \tag{3.29}$$

In 1D, the fraction of atoms with velocity in the range v to $v + dv$ is given by the 1D Maxwell-Boltzmann distribution

$$f(v_\alpha)dv_\alpha = \sqrt{\frac{m}{2\pi k_B T}} \exp\left(-\frac{mv_\alpha^2}{2k_B T}\right) dv_\alpha \quad \alpha = x, y, z, \tag{3.30}$$

By integrating over the solid angle, one can obtain the probability distribution of atomic speeds given by

$$f(v)dv = \left(\frac{m}{2\pi k_B T}\right)^{3/2} 4\pi v^2 \exp\left(-\frac{mv^2}{2k_B T}\right) dv \tag{3.31}$$

The most probable speed $v_p = \sqrt{\frac{2k_B T}{M}}$ is where the probability distribution has a maximum and is the speed most likely to be possessed by an atom. As the velocity is related to the frequency by the relation 3.29, the Doppler broadened intensity profile [56] can be written as,

$$I(\omega) = I_0 \exp\left(-\left(\frac{c(\omega - \omega_0)}{\omega_0 v_p}\right)^2\right), \tag{3.32}$$

which has a Gaussian line shape. The Doppler broadened line has a FWHM of $\Delta\omega_D = 2\omega_0\sqrt{\ln 2}\frac{v_p}{c}$. For a laser beam passing perpendicular to an ideally collimated atomic beam there should not be a Doppler broadening of the spectral profile. However for all practical reasons, the atomic beam has a divergence and this causes a residual Doppler broadening. The residual Doppler width $\Delta\omega_r$ is given by

$$\frac{\Delta\omega_r}{\Delta\omega_D} = \sin\theta, \tag{3.33}$$

where θ is the half angle divergence of the atomic beam, $\Delta\omega_D$ is the Doppler width along the direction of the atomic beam [74].
The combined line shape arising from different broadening effects which can not be neglected, can be described by a convolution of the individual line shapes. For example, the thermal broadening along with the finite lifetime of the excited state is described by a convolution of the Doppler and the Lorentzian profiles given by,

$$I(\omega) = C \int_0^\infty \frac{\exp\left(-(\frac{c(\omega - \omega_0)}{\omega_0 v_p})^2\right)}{(\omega - \omega')^2 + (\frac{\Gamma}{2})^2} d\omega'. \tag{3.34}$$

This is called a Voigt profile.

Transit time broadening

The natural linewidth gives a lower limit to the linewidth of the spectral profile and hence it usually limits the time scale on which the absorption event happens. This is true for atoms at rest. For atoms moving with a velocity v through a beam of light with diameter d, there is a finite interaction time called the transit time $t = d/v$. When $t \gg \Gamma^{-1}$, spontaneous emission process limits the linewidth. However, if $t \sim \Gamma^{-1}$, the transit time limits the linewidth as it determines the interaction time of the atom with the laser beam [75]. This can be understood as a direct consequence of the Heisenberg uncertainty principle $\Delta E \Delta t \geq \hbar$ for the energy and the lifetime of the excited state. When the transit time is comparable to the natural lifetime, this leads to a frequency broadened spectral profile dominated by the transit time broadening.

3.4 Laser spectroscopy of atoms

In order to detect and study transitions between energy levels in atoms, laser spectroscopy techniques are used to obtain the spectral profile. Typically, atoms are illuminated with a laser beam and by detecting the light after interaction, details regarding the transition that were previously discussed, can be inferred from the spectral profile.

3.4.1 Single-beam methods

The simplest spectroscopic techniques involve a single incident laser beam on the atoms. Two of the single-beam methods that are going to be discussed are absorption and fluorescence spectroscopy [76].

Absorption spectroscopy

In absorption spectroscopy, a laser beam is incident on the atoms and the beam is detected after its transmission through the atoms. Hence any absorption of light by the atoms results in a decrease of the intensity of the transmitted beam. By scanning the laser frequency over resonance, the spectral profile with its linewdith can be mapped out. In our experiments we work with an atomic beam inside a vacuum chamber. Hence due to the low pressure, pressure broadening is negligible. The natural linewidth is typically the lower bound to the width of the spectral profile. With an intensity of the incident beam less than the saturation intensity, the dominant broadening mechanism is the Doppler broadening. Recalling equation

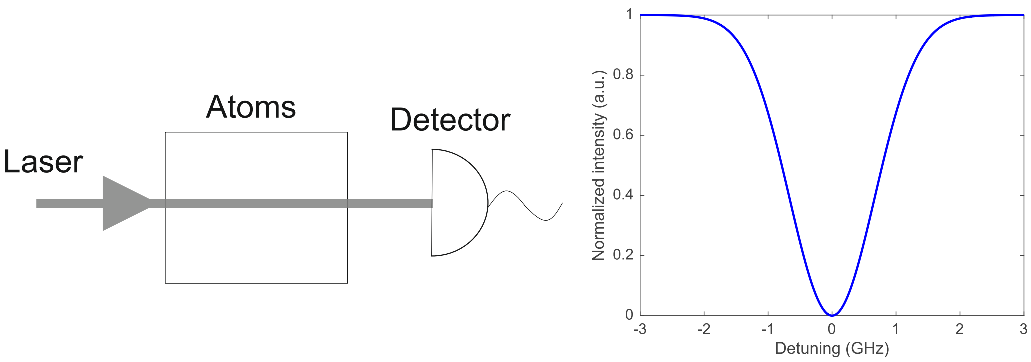

Figure 3.5: A simple absorption spectroscopy set-up and an estimated Doppler broadened profile for atoms with a transition at 421 nm and at a temperature of 1250°C, corresponding to a Doppler width ≈ 1.6 GHz.

3.29, it is only the component of velocity along the direction of the incident beam that contributes to the Doppler broadening. In our experiments, the incident beam is perpendicular to the atomic beam hence any residual Doppler broadening that sets in, is due to the fact that the atomic beam is diverging. Absorption spectroscopy could be a first step in detecting a transition but is limited as the Doppler broadened profile can reveal very little about the transition.

Fluorescence spectroscopy

Atoms after being excited by the incident light, decay back to the ground state by emitting light. In fluorescence spectroscopy, this emitted light is detected. By scanning the laser frequency over resonance, the fluorescence light reveals an identical spectral profile like absorption, but inverted. As the atoms emit light in space over all possible directions, the efficiency in detecting the light at a fixed position is much less compared to absorption spectroscopy. Fluorescence spectroscopy is also limited by Doppler broadening. However, detection of fluorescence light offers a possibility of the direct measurement of the excited state lifetime. This can be achieved by fixing the laser frequency on resonance and then switching off the incident light. Hence, the fluorescence signal would decay with the characteristic decay time corresponding to the lifetime of the excited state. This decay of the fluorescence signal can be detected if the time required to switch off the laser beam, t_{off} and and the detector response time t_{res} both are smaller than the lifetime i.e. $t_{\text{off}}, t_{\text{res}} \ll \Gamma^{-1}$.

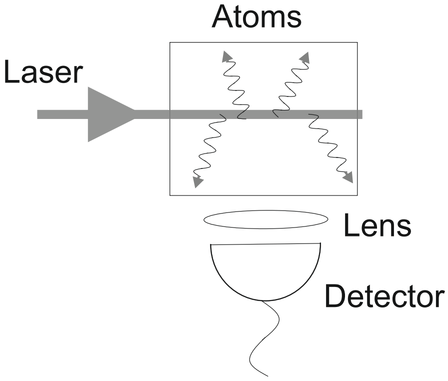

Figure 3.6: A simple fluorescence spectroscopy set-up

A Doppler-free spectroscopy that is not limited by Doppler broadening, can reveal many more interesting features of the atoms like the isotope shifts and hyperfine splitting. Spectroscopic techniques like saturation absorption spectroscopy, two-photon spectroscopy and polarization spectroscopy among others, can be used to reach the Doppler-free regime. These techniques typically use more than one laser beam.

Very weak transitions (small Γ) can not be detected using these conventional spectroscopy methods. Hence to investigate isotope shifts and hyperfine splitting corresponding to such a weak transition, we need a different detection scheme. Therefore, we use the so-called electron shelving spectroscopy in this work which is discussed next.

3.4.2 Electron shelving spectroscopy

History

In the context of high resolution spectroscopy of a single atomic ion, to detect quantum jumps, a narrow line transition (small Γ) was desired [34]. However, the signal to noise ratio of such weak transition limits the resolution. Hans Dehmelt proposed a double resonance scheme to detect such weak trasitions [34] and called it “electron shelvin”. The idea proposed was as an amplification scheme to detect a weak optical fluorescence from an ion’s metastable state using a strong resonance fluorescence as a monitor [35, 77].

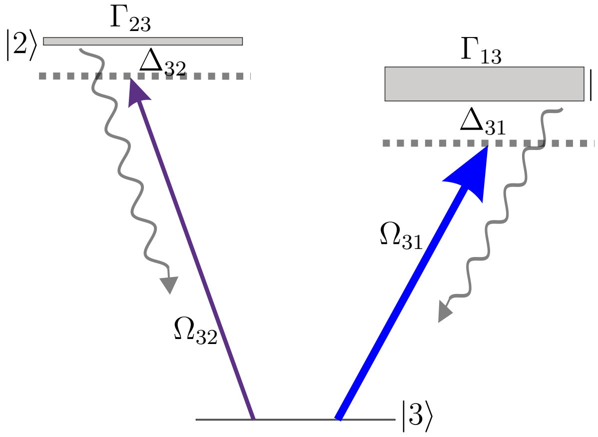

FIGURE 3.7: Three level atom in a V-configuration. The transitions between states $|i\rangle$ and $|j\rangle$ with decay rate Γ_{ij} are driven with Rabi frequencies Ω_{ij} and are detuned with respect to the atomic transition by Δ_{ij}.

Principle

An estimate of the relative strength of a transition is its natural linewidth Γ. Larger Γ means that the atom decays back faster to the ground state. The strength of the transition in terms of the detected spectroscopic signal is given by the rate of emission of photons by the excited atom, also called the scattering rate, given by

$$R_{scat} = \Gamma \rho_{22} = \Gamma \frac{I/I_{sat}}{1 + I/I_{sat} + 4\Delta^2/\Gamma^2}. \tag{3.35}$$

When the laser saturates the transition, $\rho_{22} \to 1/2$, an atom scatters about $\Gamma/2$ photons on average per second. Hence weak transitions scatter less photons and can be difficult to detect.

The idea of electron shelving scheme can be adopted to detect a weak transition. The core idea behind electron shelving method is to use a double resonance scheme involving three energy levels and two transitions with very different lifetimes. The three level scheme involving a ground state $|3\rangle$ and two excited states $|1\rangle$ with Γ_{13} and $|2\rangle$ with $\Gamma_{23}(\Gamma_{13} \gg \Gamma_{23})$ is shown in Figure 3.7.

Both transitions $|3\rangle \to |1\rangle$ and $|3\rangle \to |2\rangle$ are driven with frequencies ω_{31} and ω_{32}, the Rabi frequencies are Ω_{31} and Ω_{32} and the detunings are Δ_{31} and Δ_{32} respectively. The broad transition $|3\rangle \to |1\rangle$ is the one that is detected. When the atoms are resonant only with the broad transition, they scatter a relatively large number of photons and results in an absorption (fluorescence) signal that is easily detected. This broad transition is held on resonance and simultaneously, the other weak transition $|3\rangle \rightarrow |2\rangle$ is scanned over resonance. When the atoms are now resonant with the weak $|3\rangle \rightarrow |2\rangle$ transition, they can also be excited to the state $|2\rangle$, which makes them unavailable for the $|3\rangle \rightarrow |1\rangle$ transition and hence the atoms are “shelved”. When the atoms are shelved, they no longer scatter the photons of the strong $|3\rangle \rightarrow |1\rangle$ transition. This facilitates the detection of one absorbed photon of the weak transition by the absence of many photons of the broad transition. Hence this serves as an amplification scheme to detect a weak transition, with an amplification of approximately Γ_{13}/Γ_{23}, as the weak transition causes the absence of the photons for a typical time of the order of Γ_{23}^{-1}.

Estimating the spectroscopic response

To characterize and estimate the spectroscopic response of the atoms to the shelving scheme, we should consider the optical Bloch equations for a three level system and the dynamic evolution of the system. For a three level system in the V-configuration, the bare atomic Hamiltonian in basis of the three levels, is given by

$$H_0 = \begin{pmatrix} \hbar\omega_1 & 0 & 0 \\ 0 & \hbar\omega_2 & 0 \\ 0 & 0 & 0 \end{pmatrix}, \tag{3.36}$$

here the ground state energy $\hbar\omega_3$ is chosen to be zero. The transitions are driven with two laser beams whose electric field component is described by

$$E_{31} = \frac{1}{2}E_{031}\left(e^{-i\omega_{31}t} + e^{+i\omega_{31}t}\right) \tag{3.37}$$

$$E_{32} = \frac{1}{2}E_{032}\left(e^{-i\omega_{32}t} + e^{+i\omega_{32}t}\right). \tag{3.38}$$

The interaction Hamiltonian in the dipole approximation is given by

$$H_{int} = \frac{1}{2}\begin{pmatrix} 0 & 0 & -d_{13}E_{13} \\ 0 & 0 & -d_{23}E_{23} \\ -d_{31}E_{31} & -d_{32}E_{32} & 0 \end{pmatrix}, \tag{3.39}$$

where $E_{ij} = E_{ij}^*$. In the rotating frame and rotating wave approximation, the total Hamiltonian is given by

$$H = \begin{pmatrix} -\Delta_{31} & 0 & \frac{1}{2}\Omega_{31}^* \\ 0 & -\Delta_{32} & \frac{1}{2}\Omega_{32}^* \\ \frac{1}{2}\Omega_{31} & \frac{1}{2}\Omega_{32} & 0 \end{pmatrix}. \tag{3.40}$$

The detunings are expressed as $\Delta_{31} = \omega_1 - \omega_{31}$ and $\Delta_{32} = \omega_2 - \omega_{32}$. The Rabi frequencies are expressed as $\Omega_{ij} = -d_{ij}E_{ij}/\hbar$ and satisfy the condition $\Omega_{ij} = \Omega^*_{ji}$. The Lindblad operator for the system in the density matrix formalism is, given by

$$L = \begin{pmatrix} -\Gamma_{13}\rho_{11} & -\frac{1}{2}(\Gamma_{13}+\Gamma_{23})\rho_{12} & -\frac{1}{2}\Gamma_{13}\rho_{13} \\ -\frac{1}{2}(\Gamma_{13}+\Gamma_{23})\rho_{21} & -\Gamma_{23}\rho_{22} & -\frac{1}{2}\Gamma_{23}\rho_{23} \\ -\frac{1}{2}\Gamma_{13}\rho_{31} & -\frac{1}{2}\Gamma_{23}\rho_{32} & \Gamma_{13}\rho_{11} + (1-\kappa)\Gamma_{23}\rho_{22} \end{pmatrix}. \tag{3.41}$$

This Lindblad operator is derived from equation 3.10 except for a factor of κ. This factor κ ($0 \leq \kappa \leq 1$) accounts for a fraction of the population of atoms in the excited state $|2\rangle$ to decay back to the ground state. This is to account for the branching ratio in the decay of excited state of the weak transition to the ground state, as there can exist decay channels to other states. The dynamics of the system is described using the Lindblad master equation 3.9 and the master equation in the rotating frame of reference, written in its component form (assuming $\kappa = 1$) is given by

$$\dot{\sigma}_{11} = -\Gamma_{13}\sigma_{11} - \frac{i}{2}\Omega_{31}(\sigma_{31} - \sigma_{13}) \tag{3.42}$$

$$\dot{\sigma}_{12} = +\left(-\frac{\Gamma_{23}}{2} - \frac{\Gamma_{13}}{2} - i\Delta_{31} + i\Delta_{32}\right)\sigma_{12} + \frac{i}{2}(-\Omega_{31}\sigma_{32} + \Omega_{32}\sigma_{13}) \tag{3.43}$$

$$\dot{\sigma}_{13} = \left(-\frac{\Gamma_{13}}{2} - i\Delta_{31}\right)\sigma_{13} - \frac{i}{2}\Omega_{31}(\sigma_{33} - \sigma_{11}) + \frac{i}{2}\Omega_{32}\sigma_{12} \tag{3.44}$$

$$\dot{\sigma}_{21} = \left(-\frac{\Gamma_{13}}{2} - \frac{\Gamma_{23}}{2} + i\Delta_{31} - i\Delta_{32}\right)\sigma_{21} + \frac{i}{2}(\Omega_{31}\sigma_{23} - \Omega_{32}\sigma_{31}) \tag{3.45}$$

$$\dot{\sigma}_{22} = -\Gamma_{23}\sigma_{22} - \frac{i}{2}\Omega_{32}(\sigma_{32} - \sigma_{23}) \tag{3.46}$$

$$\dot{\sigma}_{23} = \left(-\frac{\Gamma_{23}}{2} - i\Delta_{32}\right)\sigma_{23} + \frac{i}{2}\Omega_{31}\sigma_{21} - \frac{i}{2}\Omega_{32}(\sigma_{33} - \sigma_{22}) \tag{3.47}$$

$$\dot{\sigma}_{31} = \left(-\frac{\Gamma_{13}}{2} + i\Delta_{31}\right)\sigma_{31} - \frac{i}{2}\Omega_{31}(\sigma_{11} - \sigma_{33}) - \frac{i}{2}\Omega_{32}\sigma_{21} \tag{3.48}$$

$$\dot{\sigma}_{32} = \left(-\frac{\Gamma_{23}}{2} + i\Delta_{32}\right)\sigma_{32} - \frac{i}{2}\Omega_{32}(\sigma_{22} - \sigma_{33}) - \frac{i}{2}\Omega_{31}\sigma_{12} \tag{3.49}$$

$$\dot{\sigma}_{33} = \Gamma_{1,3}\sigma_{11} - \frac{i}{2}\Omega_{31}(\sigma_{13} - \sigma_{31}) - \frac{i}{2}\Omega_{32}(\sigma_{23} - \sigma_{32}) \tag{3.50}$$

The consequence of introducing κ is that the population of atoms is not conserved and there is a loss of the atoms as they decay from state $|2\rangle$ i.e. $Tr(\dot{\sigma}) = -\kappa\Gamma_{23}\rho_{22}$. If $\kappa = 0$, then all the population in the excited state $|2\rangle$ decays to the ground state $|1\rangle$. In such a case, the population is conserved i.e. $Tr(\dot{\sigma}) = 0$. As discussed in section 3.2, the absorption of light by an atomic medium is described by the imaginary part of the linear susceptibility. The polarization density of the atomic medium is given by

$$\boldsymbol{P} = NTr(\boldsymbol{d} \cdot \boldsymbol{\sigma}) = N(d_{31}e^{+i\omega_{31}t}\sigma_{13} + d_{32}e^{+i\omega_{32}t}\sigma_{23} + d_{13}e^{-i\omega_{31}t}\sigma_{31} + d_{23}e^{-i\omega_{32}t}\sigma_{32}), \tag{3.51}$$

where N is the density of atoms. We also have

$$\boldsymbol{P} = \epsilon_0 \chi \boldsymbol{E} = \chi(\omega_{31})\frac{\epsilon_0 E_{031}}{2}\left(e^{+i\omega_{31}t} + e^{-i\omega_{31}t}\right) + \chi(\omega_{32})\frac{\epsilon_0 E_{032}}{2}\left(e^{+i\omega_{32}t} + e^{-i\omega_{32}t}\right), \tag{3.52}$$

for a three-level atom, $\chi(\omega_{ij})$ describes the linear susceptibility of the atomic medium to the light with frequency ω_{ij}. The broad transition from $|3\rangle \to |1\rangle$ is the transition that is detected. Hence we are interested in $\chi(\omega_{31})$, which is obtained by equating the corresponding terms in the equation 3.51 and equation 3.52 and expressed as

$$\chi(\omega_{31}) = \frac{2Nd_{31}}{\epsilon_0 E_{031}}\sigma_{13}. \tag{3.53}$$

To obtain the characteristic absorption of the $|3\rangle \to |1\rangle$ transition in the presence of a shelving $|3\rangle \to |2\rangle$ transition, we need to solve the master equation to obtain σ_{13}. Assuming that the population is initially in the ground state i.e. $\sigma_{33}(t = 0) = 1$, for interaction time $t \sim \Gamma_{23}$, we need to obtain a general solution i.e. $\sigma_{13}(t)$ as a result $\chi(\omega_{31}) \to \chi(\omega_{31}, t)$ and hence to obtain the observed absorption signal, we need to integrate the imaginary part of $\chi(\omega_{31}, t)$ for all the interaction time i.e.

$$\mathrm{Im}[\chi(\omega_{31})] = \frac{2Nd_{31}}{\epsilon_0 E_{031}}\int_0^t \mathrm{Im}[\sigma_{13}(t)]\mathrm{dt} \tag{3.54}$$

Atoms in motion

So far we have described a three level system of an atom at rest. As discussed in 3.3.2, the atoms in motion with a Maxwell velocity distribution have a Doppler broadened spectral profile. The motion of the atoms can be accounted for by modifying the laser detuning. For a case of two co-propagating beams (along z axis), perpendicular to the atomic beam, the detunigs take the form

$$\delta_{31} = \Delta_{31} + k_1.v_z = \Delta_{31} + \Delta_{\mathrm{D1}} \tag{3.55}$$

$$\delta_{32} = \Delta_{32} + k_2.v_z = \Delta_{32} + \Delta_{\mathrm{D2}}, \tag{3.56}$$

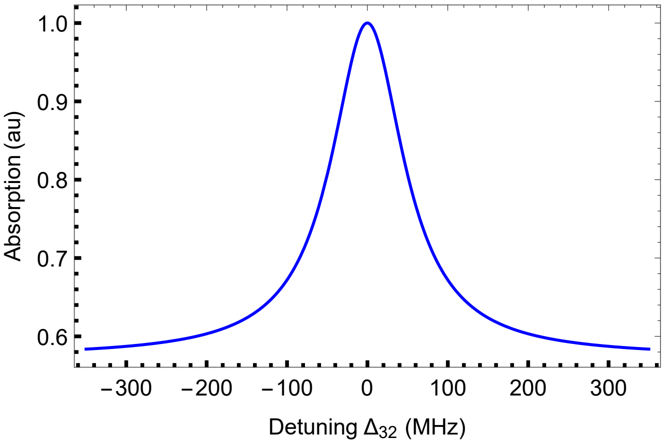

Figure 3.8: Estimated absorption profile for the shelving scheme plotted as function of the UV detuning. For the bare $|3\rangle \rightarrow |1\rangle$ transition, the residual Doppler width is given by $\delta\omega_r \approx 1.2$ GHz. The interaction time is given by $t \approx 7.8$ μs and the corresponding Rabi frequencies are given by $\Omega_{31} \approx 5.2$ MHz, $\Omega_{32} \approx 3.6$ MHz. The obtained profile has a Lorentzian lineshape with a FWHM $\approx$ 145 MHz.

where, v_z is the z component of the velocity of the atoms, k_i is the wave vector of light and Δ_i is the Doppler shift. It is to be noted that,

$$\Delta_{\mathrm{D2}} = \frac{k_2}{k_1}\Delta_{\mathrm{D1}}. \tag{3.57}$$

This equation tell us that the Doppler shift Δ_{D1} corresponding to the $|3\rangle \rightarrow |1\rangle$ transition is related to the Doppler shift Δ_{D2} corresponding to the $|3\rangle \rightarrow |2\rangle$ transition by a factor of their wave vector ratio. To account for Doppler shifts in the optical Bloch equations, the detunings in the master equation Δ_{ij} should be replaced by δ_{ij}. To obtain the contribution of all the atoms with different velocities along the transverse direction, the density matrix elements should be integrated over the distribution of velocities along the z axis. Assuming a Maxwell distribution for the velocity of atoms along the transverse direction, the velocity distribution would be centered around the most probable velocity, which in the transverse direction is zero. Hence it is convenient to integrate over the absorption intensity profile of the bare $|3\rangle \rightarrow |1\rangle$ transition (without shelving) which would directly relate to the velocity distribution of the atomic beam along the transverse direction. The absorption profile of the bare $|3\rangle \rightarrow |1\rangle$ transition take the form

$$I(\delta_{31}) = I_{01} \exp\left(-\frac{\delta_{31}^2}{2\delta\omega_r^2}\right), \tag{3.58}$$

$\delta\omega_r$ is the residual Doppler width of the obtained spectrum of $|3\rangle \rightarrow |1\rangle$ transition. The normalized absorption signal can be expressed as

$$I(\delta_{32}) = I_0 \frac{\int_{-\infty}^{\infty} \exp\left(-\frac{\Delta_{\mathrm{D1}}^2}{2\delta\omega_r^2}\right) \int_0^t \mathrm{Im}[\sigma_{13}(t, \Delta_{\mathrm{D1}})]\mathrm{dt}\ \mathrm{d}\Delta_{\mathrm{D1}}}{\int_{-\infty}^{\infty} \exp\left(-\frac{\Delta_{\mathrm{D1}}^2}{2\delta\omega_r^2}\right) \mathrm{d}\omega} \tag{3.59}$$

The absorption profile for the shelving scheme involving the weak UV transition at 358.9 nm and the broad blue transition at 421 nm, numerically calculated using the corresponding parameters set in the experiment and is shown in in Figure 3.8.

4 Experimental apparatus

In this chapter, we are going to discuss the experimental tools required to perform shelving spectroscopy, using the broad 421 nm (blue) transition as a monitor to detect the UV transition at 359 nm. For performing spectroscopy, a precise knowledege and characterization of various properties of the laser beams is essential. The 421 nm laser set-up and its characterization can be found in [78]. Here, we will discuss the set-up and characterization of the UV laser. We first introduce the general properties of Gaussian beams and discuss the measurements of relevant quantities of the beam and its pointing stability. Section 4.2 describes the spectroscopy set-up. We start with the discussion on the set-up for preparing the laser beams for spectroscopy using various optical components. As we want to perform a frequency scan around the transition frequency, it is important to calibrate the absolute frequency as well as the frequency scan range. This is realized by the means of a wavemeter and an ultra-low expansion cavity. We then discuss about the vacuum chamber where the spectroscopy is performed on an atomic beam. Finally, we conclude with a discussion on the modulation techniques used to detect a weak signal with high sensitivity.

4.1 Laser beam characterization

Gaussian beams

The lasers in our set-up produce beams that are best described by a Gaussian beam, which is the fundamental transverse electromagnetic mode (TEM_{00}). Gaussian beams are obtained as a solution to the paraxial scalar Helmholtz equation [79, 80]. For a beam propagating along the z-axis, the electric field is represented as

$$\boldsymbol{E}(r,z) = E_0 \frac{w_0}{w(z)} \exp\left(-\left(\frac{r}{w(z)}\right)^2 - ik\left(z - \frac{r}{2R(z)}\right) + i\zeta(z) \right), \tag{4.1}$$

where

$$w(z) = w_0\sqrt{1+\left(\frac{z}{z_\mathrm{R}}\right)^2} \tag{4.2}$$

is the Gaussian beam waist at distance z, defined as the radius where the intensity corresponding to the electric field drops to $1/e^2$ of the maximum. The beam has a minimum waist of w_0 and the distance z_R at which the waist increases to $\sqrt{2}w_0$ is called the Rayleigh length given by

$$z_\mathrm{R} = \frac{\pi w_0^2}{\lambda}. \tag{4.3}$$

The radius of curvature of the beam at distance z has the form

$$R(z) = z\left(1+\left(\frac{z_\mathrm{R}}{2}\right)^2\right). \tag{4.4}$$

The Gouy phase, which describes the fact that the field undergoes a π phase shift when passing through the focus is given by

$$\zeta(z) = \arctan\left(\frac{z}{z_\mathrm{R}}\right). \tag{4.5}$$

The half-angle divergence of the beam is given by

$$\theta = \lim_{z\to\infty}\arctan\left(\frac{w(z)}{z}\right) \simeq \frac{\lambda}{\pi w_0}, \tag{4.6}$$

which in the far-field regime i.e. $z \gg z_R$, takes the form

$$\theta = \frac{w_0}{z_\mathrm{R}}. \tag{4.7}$$

In the far-field regime, the beam is well described by geometric optics and the beam waist increases linearly. The numerical aperture (NA) of the Gaussian beam is defined to be $\mathrm{NA} = n\sin\theta$, where n is the refractive index. The intensity profile of a Gaussian beam is given by

$$I(r,z) = I_0\left(\frac{w_0}{w(z)}\right)^2\exp\left(-\left(\frac{2r^2}{w(z)^2}\right)\right), \tag{4.8}$$

for a fixed laser power P, the peak intensity $I_0 = \frac{2P}{\pi w_0^2}$. The laser beam quality can be quantified by the M^2 parameter given by

$$M^2 = \frac{\pi}{\lambda}\theta\, d, \tag{4.9}$$

where d is the beam diameter at the focus. For a Gaussian beam, $d = 2w_0$ and $M^2 = 1$. Typically, laser beams have $M^2 \geqslant 1$. For measuring the M^2 parameter, we need to focus the beam and measure the waist at different positions. For a focused beam, by introducing a M^2 parameter, the expression for the waist takes the form

$$w(z)^2 = w_0^2 + M^4 \left(\frac{\lambda}{\pi w_0} \right)^2 (z - z_0)^2 \tag{4.10}$$

By fitting the above equation to the data, the M^2 parameter of the beam can be extracted. The beam waist can be measured using a beam profiler which is a conventional silicon CCD or CMOS detector. However, imaging UV light can be challenging as the conventional silicon detectors have relatively little response in the UV region and the UV beam can ablate the silicon detector, leading to a persistent damage. This can cause a significant error in the beam waist measurement. Hence we measure the beam waist using the so-called knife-edge method [81]. For a beam propagating along the z direction, progressively clipped by a traversing knife-edge along the x direction, the power that is transmitted onto the detector is given by

$$P(x) = \int_{-\infty}^{\infty} P(y')dy' \int_{-\infty}^{x} P(x')dx' = \frac{P_0}{2} \left[1 \pm \operatorname{erf} \left(\frac{\sqrt{2}(x - x_0)}{w} \right) \right] + c. \tag{4.11}$$

Here, P_0 is the maximum power without clipping, x_0 is the distance at which the power is reduced to half of the maximum, c is an overall offset and $\operatorname{erf}(x)$ is the standard error function. The measured waist using the knife-edge method for the UV beam is shown in Figure 4.1. The knowledge of the waist of beams is essential to determine the intensity of the beam which in-turn is useful for determining the Rabi frequency of the beam using equation 2.2, which gives then strength of the atom-light coupling. The M^2 parameter was measured by focusing the UV beam using a 200 mm lens and measuring the waist at different positions using the knife-edge method and is shown in Figure 4.2. The extracted properties from the fit along x and y directions are given in Table 4.1.

TABLE 4.1: Beam parameters obtained by from the M^2 measurement

Direction	M^2	w_0(µm)	z_0(cm)	z_R(cm)
x	1.013 ± 0.053	59 ± 3	9.7 ± 0.15	3.02 ± 0.26
y	1.214 ± 0.112	50 ± 5	11.54 ± 0.21	2.24 ± 0.43

The obtained M^2 value is well within the specifications. The beam has a focus at different distance along each of the direction which is known as astigmatism, which can be partly corrected using cylindrical lenses.

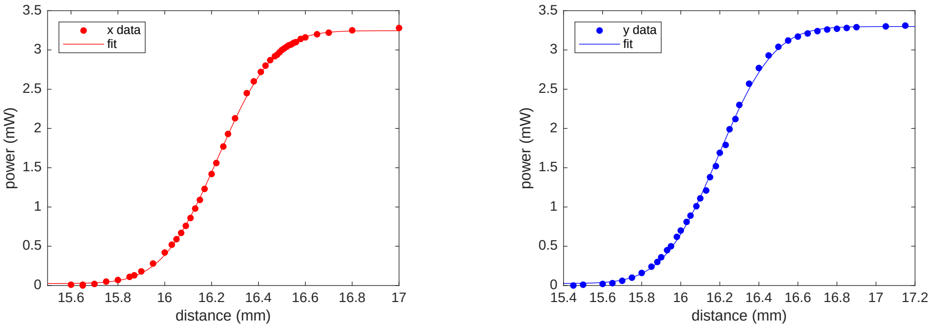

(A) Along x

(B) Along y

FIGURE 4.1: Knife-edge method for measuring the waist of the beam along x and y directions. The beam is elliptical hence the measurement is done along both the transverse directions. By fitting the data using equation 4.11, the waist was obtained to (377 ± 7) µm and (447 ± 15) µm along x and y directions, respectively

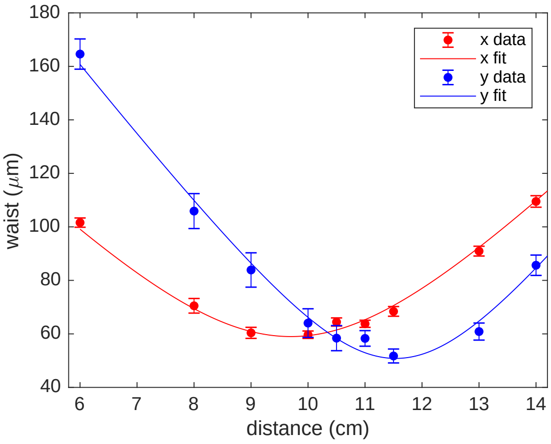

FIGURE 4.2: M^2 measurement for the beam along x and y directions and the fit for data

Pointing stability

The pointing stability of a laser beam is a measure of the drift of the position of the beam over time. Fluctuations in the beam position can arise due to mechanical vibrations and thermal drifts. In the far-field regime, pointing stability is usually quantified by an angle which specifies the tip or tilt of the laser beam from being parallel. This is done by focusing the beam using a lens with a known focal length f and measuring the position of the beam at the geometric focus over time. As we are interested in the UV beam position and as a matter of convenience, the measurements were done using a CCD camera. The position obtained by fitting

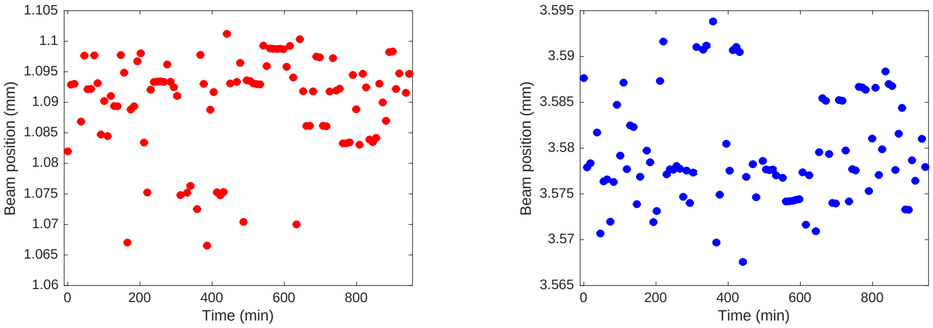

(A) Along x (B) Along y

Figure 4.3: Images of the beam were obtained using a CCD camera every 9 minutes for a period of over 15 hours and by fitting a Gaussian function to the intensity of the obtained images, the peak position of the beam on the CCD camera was obtained

a Gaussian profile for the intensity is shown in Figure 4.3. Assuming that the angular deviation is small, from the standard deviation of the beam position σ, using the relation $\theta = \frac{\sigma}{f}$ the angular deviation of the beam was estimated to be 79 µrad and 58 µrad along the x and y directions, respectively. Figure 4.4 also shows that the pointing fluctuations along both the directions are correlated. These fluctuations can arise from the small random tilts of the optical components like resonator mirrors. The correlation in the beam pointing fluctuations indicate that the fluctuations arise from tilting of the same component.

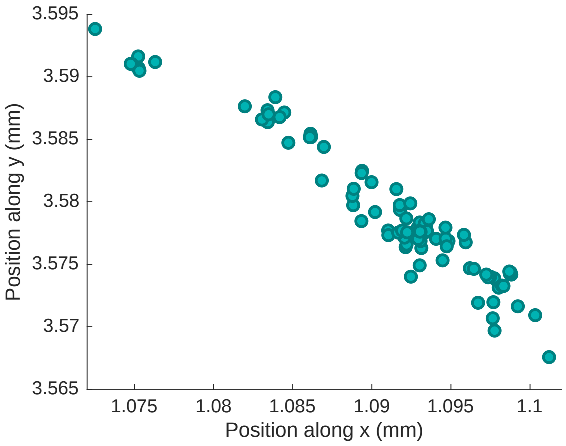

Figure 4.4: Correlation of the beam position along both the directions

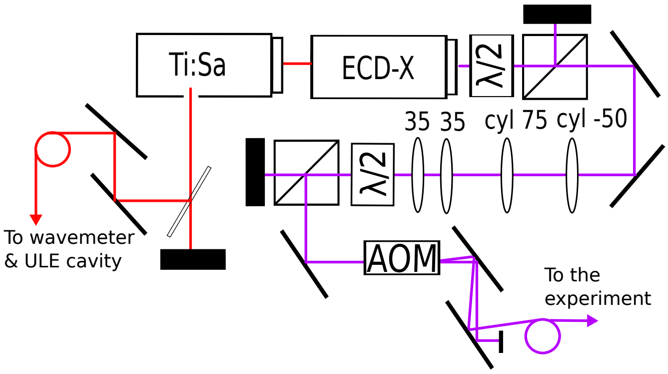

FIGURE 4.5: Schematic representation of the UV beam generation and preparing the beam for performing spectroscopy.

4.2 Spectroscopy set-up

4.2.1 UV laser set-up and characterization

The UV beam is produced in a cascade process. A diode-pumped solid state (DPSS) laser[1] produces a continuous-wave (CW) beam witha power of a 18 W at 532 nm. This is used to pump a titanium-sapphire (Ti:Sa) laser[2], which produces an output beam with a power of 6 W at 724 nm. The Ti:Sa produces a widely tunable wavelength output at high power. The output beam from the Ti:Sa laser is frequency doubled using an external cavity doubler[3] producing a UV beam of 1.9 W at 362 nm. By changing the Ti:Sa wavelength and aligning the doubling crystal, the wavelength in the UV can be adjusted.

The 421 nm beam is also produced in a similar cascade process [76]. The Ti:Sa, pumped by a 532 nm laser, produces a beam at 842 nm which is frequency doubled using a home-built monolithic ring cavity with a frequency doubling crystal.

The power of the generated UV beam coming directly out of the doubling cavity is controlled using a half-wave plate ($\lambda/2$) and a polarization beam splitter cube (PBS)[4]. To correct for astigmatism and ellipticity of the beam, we use a cylindrical lens pair, in the vertical direction. The set-up for spectroscopy is separated from the laser-setup and and the UV light is transferred by a optical fiber[5]. It was found that the efficiency of coupling the UV beam into the fiber is highly sensitive to

---

[1] Sprout-G (Lighthouse photonics)

[2] SolsTis (M squared lasers)

[3] SolsTiS ECD-X (M squared lasers)

[4] Optical components like mirrors, waveplates and PBS cubes are custom made for UV wavelength by LENS-Optics, for 350 – 360 nm. Lenses used are standard Thorlabs.

[5] Schäfter Kirchhoff PMC-E-360Si-2.3-NA012-3-APC.EC-200-P

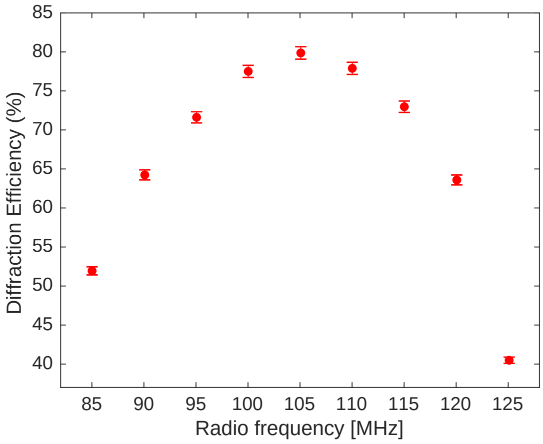

FIGURE 4.6: Diffraction efficiency of the AOM measured as a function of the radio frequency at fixed radio frequency power.

the angle at which the beam is entering the fiber as the beam can not be perfectly collimated. Hence a 1:1 telescope is included to be able to tune the position of the minimum waist of the beam and increase the coupling efficiency. The beam is then guided on to an acousto-optic modulator (AOM), which can modulate the laser beam intensity and frequency using an radio frequency (RF) drive signal based on the acousto-optic effect. For all the applications of AOM[6] thorough this work, a single-pass configuration with an AOM driver board with a 2 W amplifier is used. The first order diffraction efficiency measured at a fixed radio frequency power of 1.89 W and different radio frequencies is shown in Figure 4.6. The diffraction efficiency was measured to be constant for an input laser beam power of upto 400 mW. AOM offers high temporal control of the laser beam. By using the light of the first diffraction order, the light can be switched on and off by turning on and off the RF power. This, as we will see later, is a very important tool for measuring the lifetime of the excited state of the atomic transition. Furthermore, frequency and amplitude can be modulated.

Frequency calibration

As discussed previously, the frequency of the laser needs to be scanned in order to perform spectroscopy. Recalling equation 2.2, the Doppler width, which contributes the largest to the linewidth, is of the order of a few GHz. Hence the required frequency scan range should be able cover the entire Doppler broadened spectrum. This can be achieved by scanning the frequency of the Ti:Sa. Stable and automatic

---

[6] Gooch & Housego I-M110-3C10BB-3-GH27

re-locking of the Ti:Sa frequency is achieved with a Hänsch-Couillard locking scheme and the frequency doubled beam follows the Ti:Sa frequency scan. A web interface controls the fine wavelength tuning, frequency scan range and locking of the laser. To characterize the absolute wavelength tuning, we use a wavemeter[7] to measure the frequency and tune the Ti:Sa to the desired wavelength[8] and then scan around it.

For the relative calibration of the frequency scan, we make use of an ultra-low expansion (ULE) cavity made up of a planar mirror and a mirror with a curvature of 500 mm, seperated by a distance $d = 100.08\,\mathrm{mm}$. The mirror spacers are made out of ULE glass, which has a zero-crossing of the linear thermal expansion coefficient around room temperature at 33 °C. The light from the Ti:Sa is coupled into the ULE cavity and the leak light from the cavity is detected using a photodiode. Standing waves as eigenmodes of the resonator can be detected only for constructive interference condition depending on the frequency of the light. The free spectral range (FSR) of the cavity is defined as the distance between two consecutive cavity peaks i and $i+1$ given by

$$\mathrm{FSR} = \nu_{i+1} - \nu_i = \frac{c}{2d}, \tag{4.12}$$

where c is the speed of light. The FSR of the cavity was measured to be 1.5 GHz [78]. The finesse of the cavity is defined as the ratio of the FSR and the full width at half maximum (FWHM) of the cavity peak and is expressed as

$$\mathcal{F} = \frac{\mathrm{FSR}}{\mathrm{FWHM}} = \frac{\pi\sqrt{\mathcal{R}}}{1-\mathcal{R}}. \tag{4.13}$$

Here, $\mathcal{R} = \sqrt{\mathcal{R}_1\mathcal{R}_2}$ is the combined reflectivity of both cavity mirrors.

Using the linear ramp signal applied to obtain the desired frequency scan and the detected cavity transmission peaks, the frequency scan can be calibrated using the known FSR of the cavity. This is shown in Figure 4.7. The cavity does not only have the fundamental Gaussian mode labeled as 1 but also the higher order Hermite-Gaussian modes labeled 2 and 3. The frequency scan range read out from the control interface of the laser was 4 GHz. Using this read out scan range would yield a FSR of 2.02(5) GHz, as opposed to the known FSR = 1.5 GHz of the cavity. This implies that the total scan range, is smaller by approximately 35% than given

---

[7] TQ8325 Advantest

[8] the wavemeter reads out the wavelength in vacuum and then conversion of wavelength from air to vacuum and vice versa is followed from `http://www.astro.uu.se/valdwiki/Air-to-vacuum%20conversion`

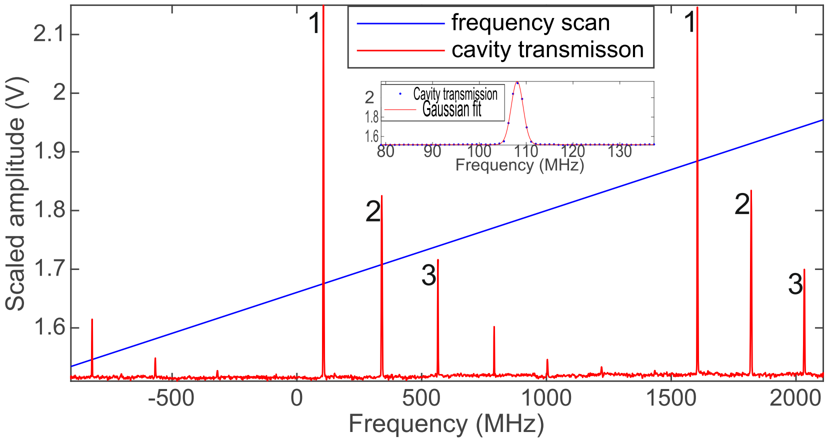

Figure 4.7: Calibration of the frequency scan using the FSR of the ULE cavity transmission peaks. The frequency axis is obtained by calibrating the ramp signal using the FSR of the cavity. Inset: A Gaussian fit for the fundamental peak of the cavity labeled as 1.

by the internal calibration of the laser. Therefore we calibrate the ramp signal using the FSR of the cavity and obtain the frequency axis.

Another aspect concerning the frequency scan is its linearity. The measure of the linear behavior of the frequency scan can be verified by comparing the FSR of higher order modes of the cavity spread across the scan. The measured FSR of the peaks 2 and 3 are 1.480(3) GHz and 1.462(6) GHz, which indicates a non-linearity of the scan with an average deviation of approximately 2.5%. However for the error in the frequency measurements, the extreme case of maximum observed non-linearity of about 3.3 % is used.

By fitting a Gaussian function to the fundamental cavity peak, the FWHM can be extracted and the finesse of the cavity can be estimated. The FWHM of the fundamental cavity peak was determined to be 2.1(6) MHz and the finesse was estimated to be 714±205. The non-linearity in the scan range and the FWHM of the cavity peaks give an estimate of the uncertainty in determining the absolute frequency, which as we shall see later, is useful to state the confidence interval for the isotope and hyperfine shifts.

4.2.2 Shelving spectroscopy set-up

After the previous discussion regarding the UV laser set-up and its characterization, we now discuss the shelving spectroscopy set-up, which is shown in Figure 4.8. For the shelving spectroscopy, we use a broad transition as a monitor to detect a weak transition. In our case, this broad transition is the 421 nm transition (blue) in Dysprosium and we are going to detect the weak UV transition at 359 . Both the beams are fiber coupled to the spectroscopy set-up. We then use a dichroic mirror to overlap these beams and direct them towards the atoms.

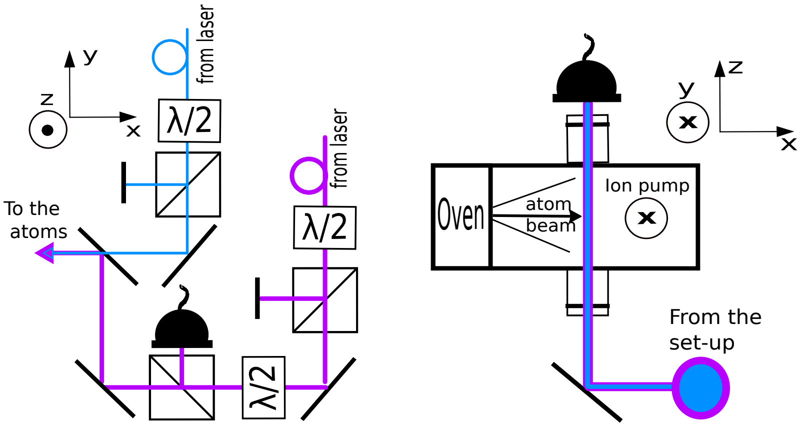

FIGURE 4.8: Schematic representation of the shelving spectroscopy set-up

To produce the atomic beam of Dy, we fill metallic Dy granulate in a molybdenum crucible and place it in an effusion oven which heats up the Dy. The oven is operated at 1250 °C and it has a shutter that can block the atomic beam. The oven is mounted in a vacuum chamber, in which the pressure is pumped down to $p \approx 1 \times 10^{-8}$ mbar. An ion pump is used to maintain the vacuum which is placed perpendicular to the atoms and the light. The laser beams enter the vacuum chamber through a viewport that provides optical access. The laser beams are perpendicular to the atomic beam and are detected using a photo diode. Fluorescence of the atoms can also be detected by using another viewport of the chamber.

Modulation technique

Here, we are going to discuss about a technique used to detect weak signals buried in noise. Conventional amplification to detect a weak signal results in amplification of the noise as well. A higher sensitivity of a spectroscopic signal can be achieved by using modulation techniques, which involves modulating the frequency or the amplitude of the light at a fixed frequency. The detected light is evaluated at the modulation frequency. Typically, technical noise has a main contribution at low frequencies and depends on frequency f as $1/f$. Therefore, modulation technique suppress this noise and other noise contributions that do not fall in the detection frequency band centered around the modulation frequency [82]. This greatly improves the signal-to-noise ratio (SNR). Modulation techniques involve a phase-sensitive detection which is realized using a lock-in amplifier. A lock-in amplifier is a signal processing instrument that performs a multiplication of the modulated input signal with a reference signal at the same modulation frequency, and then applies an adjustable low-pass filter to obtain the desired output. This method isolates the signal at the frequency of interest from all other frequency components. The modulated laser beam is sent through the atomic beam and is detected with a photodiode connected to a lock-in amplifier[9]. The working of a lock-in amplifier for the case of frequency and amplitude modulation is discussed below.

Amplitude modulation

The intensity of the laser beam can modulated by modulating the AOM driving power. Assuming a sinusoidal intensity of the detected laser beam produced by the modulation, using a sinusoidal reference of the form $m \sin(\omega_m t)$, where ω_m is the modulation frequency and m is the modulation amplitude, the detected intensity on the photodiode takes the form

$$I(t) = I_0 \sin(\omega t + \phi). \tag{4.14}$$

Here, ω is the frequency of the detected beam ϕ is the relative phase difference between the input and the reference signal. The product of these two signals gives beats at the sum and difference frequencies.

$$I_b = \frac{I_0}{2} \left(\cos\left[(\omega - \omega_m) t + \phi \right] - \cos\left[(\omega + \omega_m) t + \phi \right] \right). \tag{4.15}$$

The lock-in amplifier evaluates the detection at ω_m and hence the output is

$$I_b = \frac{I_0}{2} \left(\cos[\phi] - \cos\left[(2\omega_m) t + \phi \right] \right). \tag{4.16}$$

Using the adjustable low pass filter, the lock-in amplifier extracts the DC component and by adjusting the phase ϕ, we can optimize the signal to get a direct measure

---

[9] LIA-MV-200-H (FEMTO)

of the transmitted intensity. Hence by modulating the intensity of the beam at a modulation frequency and by using a lock-in amplifier to perform a phase sensitive detection, any unwanted signal oscillating at different frequencies and noise at frequency other than ω_m is eliminated.

Frequency modulation

The laser frequency ω is modulated using a sinusoidal reference signal of the form $m\sin(\omega_m t)$, where ω_m is the modulation frequency and m is the modulation amplitude. This leads to a modulation of the detected intensity on the photodiode taking the form

$$I(t) = I(\omega + m\sin(\omega_m t)). \tag{4.17}$$

We can use a Taylor series expansion around ω to write the intensity as

$$I(\omega+m\sin(\omega_m t)) = I(\omega)+(m\sin(\omega_m t))\frac{\mathrm{d}I}{\mathrm{d}\omega}+\left(\frac{m^2\sin^2(\omega_m t)}{2!}\frac{\mathrm{d}^2 I}{\mathrm{d}\omega^2}\right)+\ldots \tag{4.18}$$

It is assumed that the phase is adjusted to optimize the signal. In the case of frequency modulation, the lock-in amplifier picks out the fundamental Fourier component of this signal at ω_m, hence the other frequency components are neglected. For $m \ll 1$, the detected intensity is proportional to the first derivative of the transmitted intensity at ω. This property to generate derivative signals in spectroscopy, can be used to generate error signals, which in-turn can be used as a feedback to stabilize the laser frequency.

5 Shelving spectroscopy of the 359 nm transition

This chapter describes the extensive experimental characterization of the UV transition by analyzing the obtained spectrum using the shelving method. The chapter begins with a discussion on the need for shelving method to detect the UV transition, where the characteristics of the UV transition are emphasized. Next, we analyze and understand the obtained spectrum. After detecting the transition, we progressively move towards characterization of the transition. First, the isotope shifts of the transition are measured and then a King plot analysis is performed to estimate the electronic nature of the transition. We then analyze the hyperfine transitions of the fermionic isotopes to estimate the excited state hyperfine constants. The lifetime of the excited state is estimated by observing the decay of the atoms. To conclude, we discuss the dependence of the spectral properties on various control parameters and possible sources of uncertainty in the measurements.

5.1 Need for shelving spectroscopy

As discussed previously, we are going to perform shelving spectroscopy of the 359 nm UV transition using the strong 421 nm (blue) transition as a monitor. The shelving spectroscopy is employed because the UV transition could not be detected using conventional single beam methods like absorption and fluorescence spectroscopy even using an amplitude modulation technique. To confirm that this not due to a problem in the spectroscopy set-up and to ensure that the vacuum chamber and the atomic beam are functioning intact, the set-up was tested by performing absorption spectroscopy of the blue transition first. As discussed in section 3.4.2, spectroscopy of the blue transition gives an estimate of the residual Doppler width and the transversal velocity distribution and hence is a prerequisite to perform shelving spectroscopy.

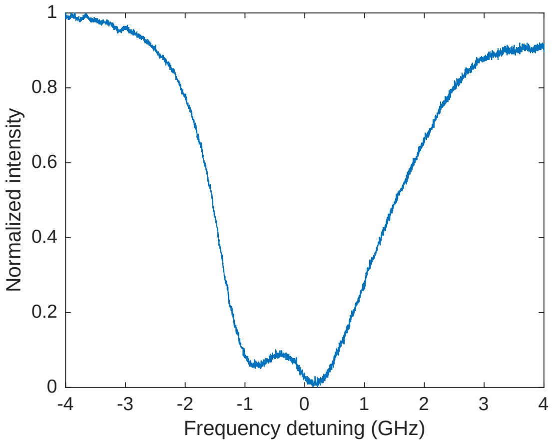

Figure 5.1: The absorption spectrum of the blue transition obtained at an oven temperature of 1250 °C, in a configuration where the laser beam and the atom beam are perpendicular to each other. The two distinct peaks are identified and by estimating the residual Doppler width, information on the transverse velocity distribution can be obtained

An absorption spectrum of the blue transition at an oven temperature of 1250 °C, with the atomic beam perpendicular to the laser beam, was obtained and is shown in Figure 5.1. We see two distinct peaks and we identify the left peak with the transition frequency corresponding to ^{164}Dy. The frequncy difference between these two peaks is approximately 930 MHz, which is close to the isotope shift of ^{162}Dy with respect to ^{164}Dy [36]. However, the other peak is an envelope, which is dominated by the transition frequency corresponding to ^{162}Dy and consists of transitions involving other isotopes and the hyperfine structure.

As discussed in section 3.3.2, in a configuration where the atomic beam and the laser beam are perpendicular, the divergence of the atomic beam causes a residual Doppler width which is given by equation 3.33. The residual Doppler width $\Delta\omega_r$ is smaller than the Doppler width $\Delta\omega_D = 2\sqrt{\log 2}\omega_0 \frac{v_p}{c}$ for the case when the atomic beam is along the direction of the laser beam, by a factor of $\sin\theta$ [74]. By fitting a Gaussian function to the left peak, a residual Doppler width $\Delta\omega_r = (1685 \pm 12)$ MHz was obtained, whereas it is found that $\Delta\omega_D = 1562$ MHz at 1250 °C. In our case, the estimated residual Doppler width is larger and hence the estimation of an angle using the residual Doppler width is not very useful. A better estimate of the width can be obtained if the peaks can be resolved. In an effort to resolve the peaks, the oven temperature was decreased but even at the lowest temperature where we could identify a signal corresponding to absorption, at 1000°C, we could only observe two broad peaks.

During the spectroscopy measurements, over a period of time, a visible layer of Dy got deposited from the atom beam on the viewport that is perpendicular to the atom beam. By estimating the vertical and horizontal distances of the coating on the viewport from the atom beam, the half angle of divergence was calculated to be approximately 76°, which would cause a residual Doppler width of roughly 1515 MHz.

A large divergence of the atomic beam can be attributed to the various reasons concerning the design of the oven. Any large inhomogeneity in the heating of the crucible or a large diameter of the oven aperture would result in an inhomogeneous density profile of the atoms which could be a possible source for a large divergence of the atomic beam. Though the atomic beam shows a large divergence, by obtaining a spectral profile corresponding to the blue transition, we can be sure that the whole spectroscopy set-up is working intact and we have performed the prerequisite step for shelving spectroscopy. We can now investigate as to why the UV transition could not be detected using simple conventional single beam methods.

To estimate the relative strength of the transition, we can compare the number of photons scattered by the blue and the UV transition. Recalling equation 3.35,on an average the number of photons scattered by an atom per second at the saturation intensity is given by $\Gamma/2$. The saturation intensity given by equation 3.23, is 56.4 $\frac{\mathrm{mW}}{\mathrm{cm}^2}$ and 0.15 $\frac{\mathrm{mW}}{\mathrm{cm}^2}$ for the blue and UV transition respectively. The atoms, when undergoing the blue transition, scatter about 1.6×10^7 photons per second whereas while undergoing the UV transition scatter about 2.6×10^4 photons per second at their respective saturation intensities. In the experiment, we have a transit time of about 7.8 μs which leads to roughly 126 photons scattered for the blue transition and less than 1 photon scattered for the UV transition on an average at their corresponding saturation intensities. This makes it challenging to detect the UV transition using single beam methods. Moreover, the branching ratio of the UV transition remains unknown. Hence there is a possibility that the the excited state atom might not decay to the ground state which leads to lesser photons scattered. Another important aspect regarding the nature of this UV transition that we have discussed in section 2.2.1 is the electronic nature of the excited state. The UV transition is from the ground state to a doubly excite state i.e. $4f^{10}6s^2(^5\mathrm{I}_8) \rightarrow 4f^9(^6\mathrm{H}^\mathrm{o})5d^2(^3\mathrm{P})(^8\mathrm{I}^\mathrm{o})6s$. As this transition involves two electrons, the transition strength is rather weak and makes it difficult to detect with conventional spectroscopy techniques.

For all the reasons discussed above, we need a different technique to detect such a transition and this is done using shelving spectroscopy, which is an elegant and powerful amplification scheme to detect weak transitions using a strong transition. From the discussion in section 3.4.2, shelving spectroscopy provides an amplification

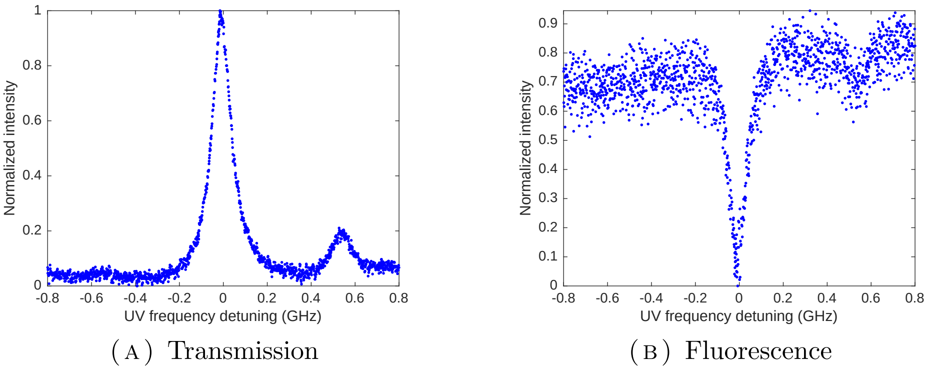

(A) Transmission (B) Fluorescence

FIGURE 5.2: The normalized transmission and fluorescence signals of the monitored blue transition held on a fixed frequency, obtained by scanning the frequency of UV beam around resonance. The spectrum obtained is averaged over about 20 shots. The peaks (dips) in the spectra correspond to the UV transitions of different isotopes and hyperfine levels.

of the order of $\Gamma_{13}/\Gamma_{23} \approx 620$, where $\Gamma_{13} = 32.2$ MHz and $\Gamma_{23} = 51.9$ kHz are the natural linewidth of the broad blue transition and the narrow UV transition respectively.

5.2 Shelving spectrum

Now that we have discussed the need and advantages of shelving spectroscopy, we now discuss the spectrum obtained using shelving spectroscopy. The blue beam is held on a fixed frequency around resonance and the absorption and fluorescence of the blue transition is monitored while the frequency of UV beam is scanned over resonance. To monitor absorption, the detected signal is the transmitted light after interaction with the atomic beam. For the procedure of locking the frequency of the blue beam refer [78]. As a preliminary result, the success of shelving spectroscopy over conventional single beam methods is demonstrated as the spectrum of the UV transition is obtained in both absorption and fluorescence which is shown in Figure 5.2.

The transmission(fluorescence) signal of the blue transition shows a peak (dip) as the UV beam is scanned over resonance. When the atoms are resonant with the UV transition, they are no longer available on resonance for the blue transition due to the long lifetime of the UV excited state, as discussed in section 3.4.2. The frequency is not calibrated using the ULE cavity and moreover, no modulation technique was used. Hence for further discussion on the spectrum, we calibrate the frequency using the ULE cavity and using a modulation scheme to improve

TABLE 5.1: Parameters used in experiment: Power (P), beam waist(σ), Intensity(I), Rabi frequency(Ω)

beam	P(mW)	σ(mm)	I(mW/cm^2)	Ω(MHz)
Blue	0.1	1.49	2.9	5.2
UV	53	1.55	1405.9	3.6

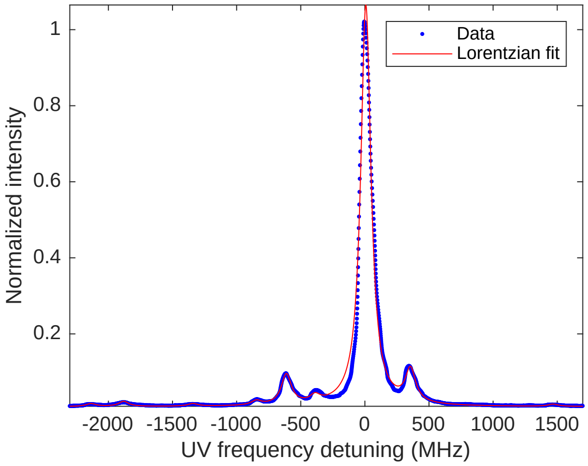

FIGURE 5.3: The transmission of the blue beam obtained by fixing the blue frequency on resonance corresponding to he transition to ^{164}Dy. The transmission signal detection is improved compared to the previous spectrum by using amplitude modulation technique and a lock-in amplifier to detect. The data is fit with a model consisting of nine Lorentzian functions for the nine detected peaks. The obtained spectrum is averaged over about 30 shots

the signal-to-noise ratio (SNR). The parameters used in obtaining the shelving spectrum are shown in Table 5.1.

UV beam of a larger waist was used to increase the interaction time with the atoms and a smaller blue beam was overlapped with the UV beam. A large power of the UV beam was used to increase the intensity and hence the Rabi frequency, which should lead to a stronger atom-light coupling and hence a better signal. An amplitude modulation technique was implemented by chopping the UV beam by modulating the radio frequency power used to drive the AOM at 23 kHz and a lock-in amplifier was used to improve the SNR of the detected transmission of the blue beam. The lock-in amplifier signal for the frequency of the blue beam fixed on resonance with the transition frequency corresponding to ^{164}Dy is shown in Figure 5.3. The lock-in amplifier signal increases the SNR of the transmission signal, so that new peaks at other frequencies can be identified. The frequency is calibrated using the Gaussian modes of the ULE cavity as discussed in section 4.2.1.

Each peak corresponds to a UV transition from the ground state to the excited state corresponding to one of the bosonic isotopes or the hyperfine levels of the fermionic isotopes. By fitting the data to a sum of nine Lorentzian functions with same width, the full width half maximum (FWHM) was estimated to be (96 ± 1) MHz. The estimation of the width of the peak as discussed in section 3.4.2, is obtain from the contribution of all the atoms with different velocities along the transverse direction. On the other hand, the amplitude of a peak is proportional to the density of atoms contributing to the specific transition and this in turn depends on two factors. One is the natural abundance of the isotopes, which is fixed. The other factor is due to the velocity distribution of atoms. Recalling 3.29, for the case of perpendicular atomic and laser beams, the atoms with velocity component v_z along the beam, tend to absorb the light with the detuning $\Delta = \omega - \omega_0 = k|v_z|$. As we monitor the blue beam, the velocity class that is addressed is selected by the corresponding blue detuning. When the frequency of the blue beam ω is fixed to a blue transition frequency ω_0, atoms with $v_z = 0$ are more probable to absorb the blue beam. Along the transverse direction, $v_z = 0$ is the most probable speed and the highest probability distribution for the number of atoms and hence the largest absorption signal. As the UV transition is detected by the absence of the scattered photons of this blue absorption, this implies that the amplitude of the observed UV peaks depend upon the detuning of the blue beam.

In the spectrum shown in Figure 5.3, as the blue frequency is held on resonance with the transition frequency corresponding to ^{164}Dy and as ^{164}Dy is the most abundant isotope, unambiguously the dominant transition in the shelving spectrum would be that of the UV transition corresponding to ^{164}Dy and we can clearly assign it. The other peaks correspond to other isotopes and their realtive amplitude is small and hence to determine the isotope shifts and the hyperfine splitting of the UV transition, the blue beam should be detuned to the resonance frequencies of each of the respective transitions.

5.3 Determination of isotope shifts and hyperfine splitting

5.3.1 Determining the resonance blue frequency for transition corresponding to ^{164}Dy

As discussed in the previous section, to determine the isotope shifts and the hyperfine splitting, we need to detune the blue beam frequency to the respective transition with respect to the ^{164}Dy transition. The isotope shifts and the hyperfine

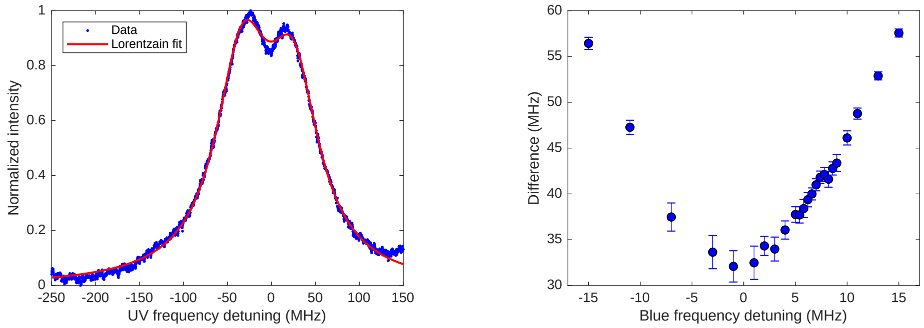

(A) Transmission

(B) Distance between the peaks

Figure 5.4: (A) The transmission of the blue beam fixed approximately on resonance, in the presence of an additional retro-reflected UV beam. The signal shows two peaks with an overlap. (B) The difference in the position of the two peaks as function of the detuning of the blue beam. The error in determining the position of the peak is obtained by fitting a sum of 2 Lorentzain peaks to the data. The difference does not go to zero but shows a minimum approximately at 32 MHz

splitting of the blue transition are known accurately [36]. Hence we need to determine the absolute position of the resonant blue transition of ^{164}Dy. To do this, the blue beam is fixed approximately at the resonance frequency and the UV beam after passing through the vacuum chamber is retro-reflected back onto the atoms while detecting the blue transition by shelving method. The spectrum thus obtained is shown in Figure 5.4. For a fixed detuning of the blue beam, the two UV beam propagating anti-parallel to each other, give rise to two peaks for the same transition frequency corresponding to ^{164}Dy. On blue resonance, ideally, there should only be a single peak. By accurately tuning the blue beam frequency, and by observing the transmission signal, we can identify the resonance position of the transition corresponding to ^{164}Dy. However as we plot the difference in the position of the peaks obtained by fitting the data to a Lorentzian function, it is observed that the difference doesn't go to zero but shows a minimum at approximately at 32 MHz. There could be a possible misalignment of the retro-reflected beam but 32 MHz is very large to be explained just due to misalignment. This is reminiscent of an avoided crossing. However, to comment any further on this feature, involves considering posssible interference effects between various interaction and transition pathways between the 3 atomic levels and the 3 beams and we are not going to discuss it here. The accurate resonance position could not be determined but it was estimated approximately.

Using the known isotope shifts and the hyperfine splitting of the blue transition [36],

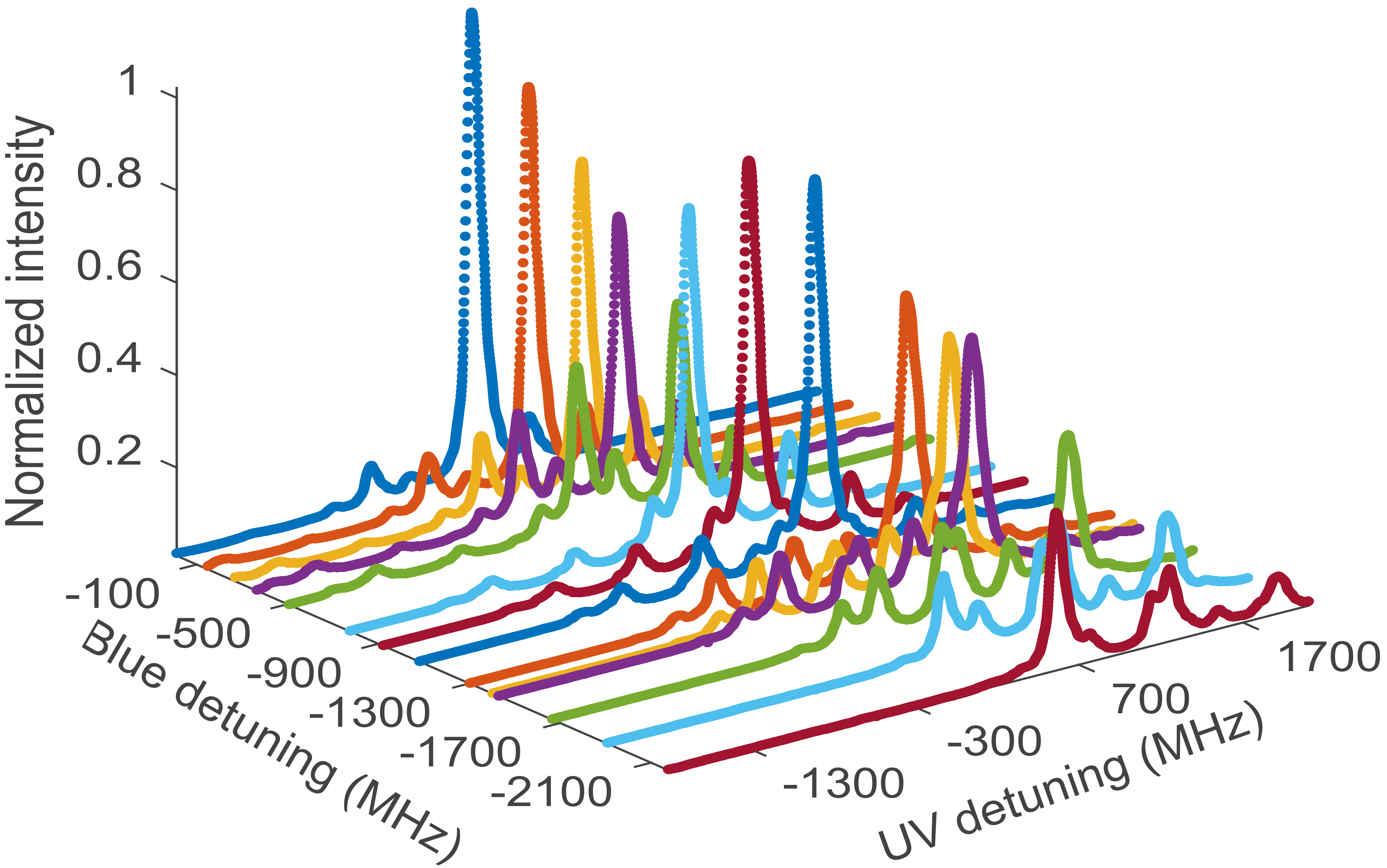

Figure 5.5: The transmission of the blue beam for different blue frequency detuning. For each blue frequency detuning, the UV frequency is scanned over resonance

the detuning of the blue beam can be varied to obtain a peak for the corresponding UV transition. A spectrum thus obtained by scanning UV frequency around resonance for each blue frequency detuning is shown in Figure 5.5.

There were 15 identified peaks[1]. The amplitudes and the positions of each of these peaks for different blue detuning is shown in Figure 5.6 According to equation

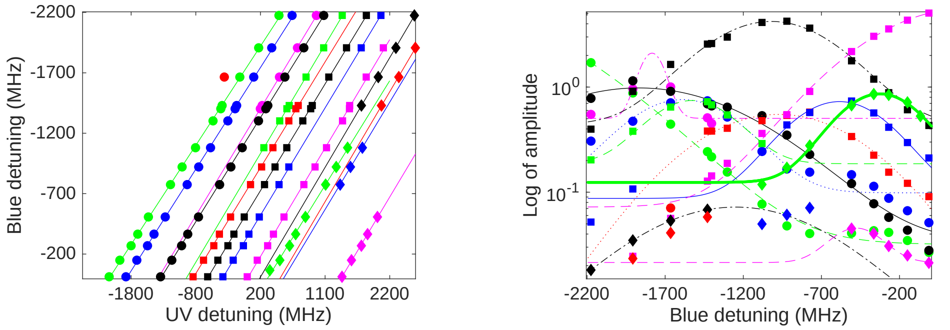

(A) Position of identified peaks

(B) Amplitude of identified peaks

FIGURE 5.6: (A) The position of the 15 identified peaks on the UV frequency plotted as a function of the blue detuning. A linear model it used to fit the data and the slope as expected is given by the wavevector ratio. (B) The amplitudes of identified peaks plotted on a logarithmic scale as a function of blue detuning. Across the blue detuning, the peaks trace out the velocity distribution and hence the data is fit with a Gaussian function.

3.57, detuning of blue would correspond to a frequency shift in the position of the peak by a factor of the ratio of the wavevectors. By fitting a linear model to the position of the peaks, a slope of 0.88(3) was obtained which is close to the wavevector ratio 0.85. As we are changing the blue detuning, the individual peaks would show a residual Doppler broadening as a function of the blue detuning and hence each of the peak is fit using a Gaussian function. This is not a very accurate determination of the residual Doppler broadening as there are only few data points and in some cases, there is insufficient data. However within this framework, the residual Doppler broadening was estimated to be (789 ± 243 MHz).

With the shelving method, the expected linewidth is given by the linewidth of the blue transition with the factor of the ratio of the wavevectors i.e. $\frac{k_{UV}}{k_B}\Gamma_B \approx 38\,\mathrm{MHz}$. However, the FWHM of the shelving spectrum, estimated by fitting a sum of Lorentzian functions to all the UV transition peaks for each blue detuning, is 99(4) MHz. This can be due to the contribution to the peak coming from not only

---

[1] the amplitude and the position of the peaks were identified using the MATLAB function "findpeaks" on the condition that the minimum prominence of a peak is greater than the noise

the zero velocity class atoms but the whole velocity distribution and possible power broadening effects.

5.3.2 General procedure for assigning a peak

Fifteen peaks were identified across the whole spectrum, which need to be assigned to their respective transitions. In general, to assign a peak corresponding to the UV transition from a specific isotope or a hyperfine level, the blue beam is fixed on resonance to address the transition with the same level. When both the beams are resonant to the transition involving the same isotope or the hyperfine level, the amplitude of the peak corresponding to this transition should be large. However, as we are scanning the UV frequency across resonance, due to the factor of natural abundance, along the UV detuning of this spectrum, this peak might not have the highest amplitude compared to the other peaks. Hence we observe the spectrum across the blue resonance, to identify the maximum of this peak. For the sake of convenience, the spectrum shown in Figure 5.5 is represented as a color plot in Figure 5.7. To track the position of a peak across the blue detuning, the linear fits to the position of the peaks shown in Figure 5.6(A) are plotted on top of the spectrum. The calculated blue resonance frequency for a transition is indicated as a marker on the y axis along which we have to identify the intensity maximum of a peak and assign to the transition involving the same isotope or hyperfine level. If there exists an identified peak, which is indicated by of the linear fit to the position of peaks, and this peak exhibits a maximum in intensity, which is identified by observing the amplitudes across the blue resonance, it implies that both the beams are addressing the same zero velocity class ground state atoms and hence the maximum in intensity across the blue frequency. The peak is then assigned to the UV transition of the corresponding isotope or the hyperfine level that is being addressed by the blue beam and this is finally indicated as a marker on the x axis. To summarize the procedure used to assign a peak,

- The calculated blue resonance frequency corresponding to an isotope or a hyperfine level is indicated, along which identified peaks have to be spotted.

- The identified peaks within the spectrum are traced using the linear fits to the position of the peaks, then we look at the intensity across the blue detuning to check if it has a maximum.

- If there exists a maximum in intensity across the blue detuning around the marked resonance position, then we assign the peak to a UV transition to the corresponding isotope or hyperfine level and then finally this is indicated on the UV frequency.

5.3.3 Assigning the bosonic isotope peaks

As a first step, it is relatively easy to assign the UV transition corresponding to the three bosonic isotopes as they exhibit no hyperfine structure. Two of them ^{164}Dy and ^{162}Dy have natural abundance more than any other isotope and hence will have larger intensity. We have already assigned the UV transition corresponding to ^{164}Dy and the corresponding resonance position along the blue and UV frequency is fixed to zero. The UV transition corresponding to ^{162}Dy and ^{160}Dy are assigned via the general procedure outlined above. The blue resonance frequency corresponding to each of the isotopes is indicated on the blue detuning. For the sake of convenience, only linear fits to the position of three relevant peaks are shown in Figure 5.7. These three peaks exhibit a maximum along the blue detuning around the respective blue resonance frequency. Hence the UV transitions corresponding to ^{162}Dy and ^{160}Dy are assigned. The isotope shifts $\Delta\nu_{i-j} = \nu_i - \nu_j$, for the bosonic isotopes ^{162}Dy and ^{160}Dy of the UV transition are obtained as $\Delta\nu_{164-162} = -414\,\mathrm{MHz}$, $\Delta\nu_{164-160} = -856\,\mathrm{MHz}$ and $\Delta\nu_{162-160} = -442\,\mathrm{MHz}$.

The outline of the further procedure to characterize the transition is as follows

- As three isotope shifts are measured, a King plot analysis is performed, which is the first step from which the electronic nature of the transition is predicted and the isotope shifts of the fermionic isotopes are calculated.
- We then identify atleast two hypefine transitions via the general procedure outlined above, to be able to calculate the excited state hyperfine constants.
- Using the calculated hyperfine constants and the isotope shifts, the frequency shifts for other hyperfine transitions are predicted. With the help of the general procedure, we verify if there exists a peak that exhibits a maximum and if it is unassigned yet.

If the predicted peak positions match a measured peak which exhibits a maximum and which is yet unassigned, this would be a strong validation of the calculated isotope shifts and the hyperfine constants. The success of the entire procedure can be demonstrated if we can clearly assign a peak whose position is predicted.

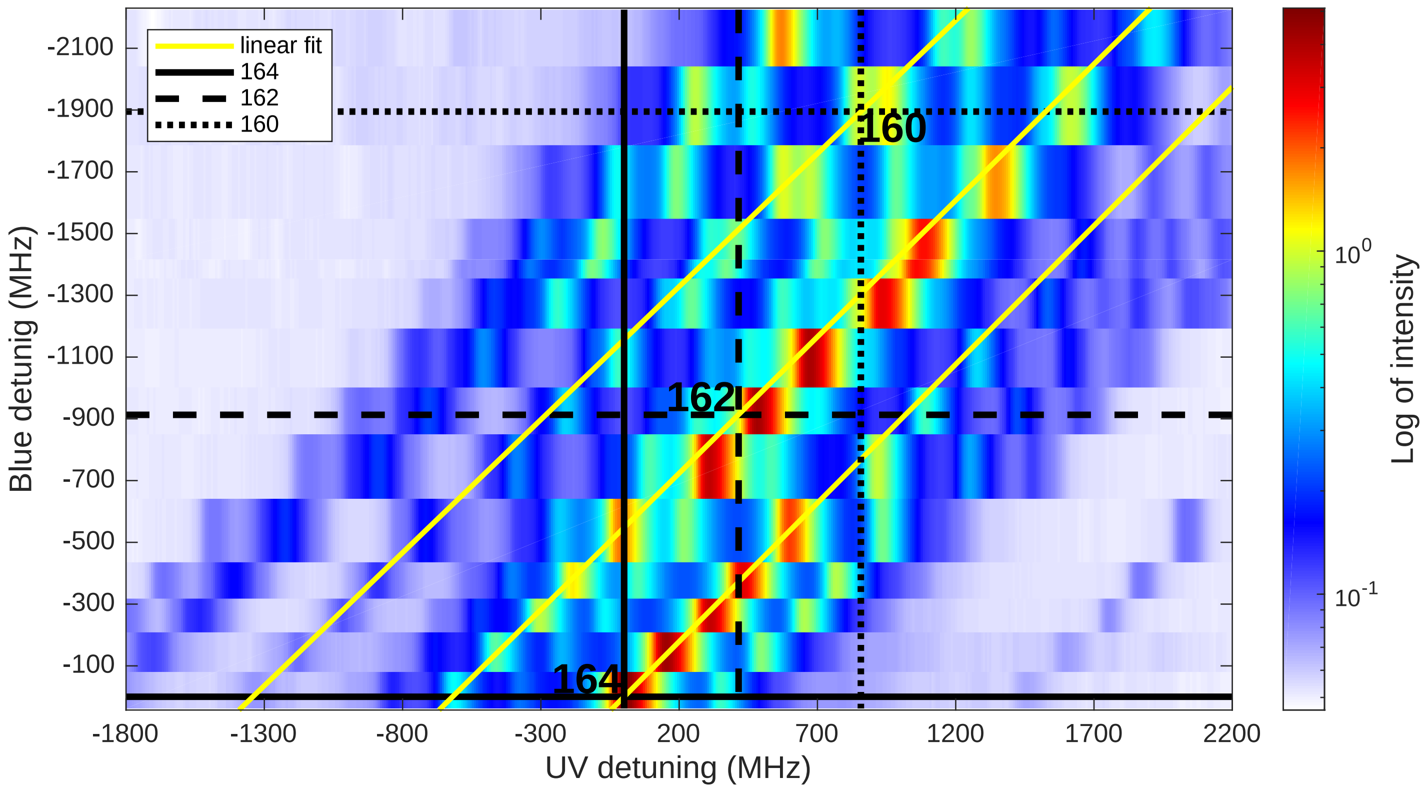

Figure 5.7: Shelving spectrum obtained by scanning the UV transition frequency for different blue detuning same as in Figure 5.5 but represented using a color plot. The zero position along blue and UV frequency is fixed to the resonance of corresponding to the transition of ^{164}Dy. The notation is such that 164 indicates the transition frequency for ^{164}Dy. The horizontal markers are indicators to the blue resonance frequency. The transitions involving the same ground states are identically marked on the x and y axis as an aid to identify a peak. Linear fits to the identified peak positions are indicated to track a peak across the spectrum. After assigning a peak as outlined in the general procedure, the UV resonance frequency is indicated by the corresponding vertical markers.

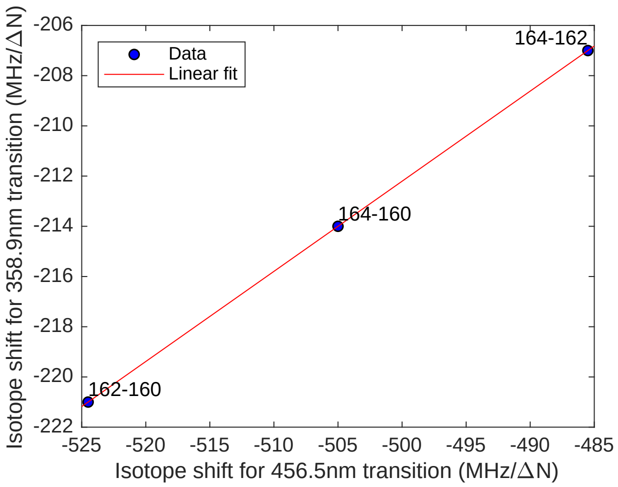

FIGURE 5.8: The isotope shifts for the bosonic isotopes normalized with difference in mass number, of the UV transition plotted with a reference transition to obtain a King plot. The data is fit with a linear model.

5.3.4 Isotope shifts and King plot analysis

As mentioned above,a King plot analysis for the measured isotope shifts for the bosonic isotopes is performed using the isotope shifts corresponding to a reference transition to obtain information on the electronic nature of the UV transition. As discussed in section 2.2.3, the reference transition should correspond to a pure $(ns^2 - nsnp)$ excite state. Hence the 456.509 nm transition is chosen and the respective isotope shifts are shown in Table 5.3. The isotope shift is normalized with the difference in mass numbers and a King plot is obtained and is shown in Figure 5.8. From a linear fit to the data, the slope and the intercept were obtained as 0.359 and -32.72 MHz respectively. The slope gives the ratio of field shift (FS) parameters i.e. $\frac{E_{359}}{E_{457}} = 0.359$. The normal mass shift (NMS) for two isotopes $\Delta\nu_{i\,\mathrm{NMS}}^{A_2,A_1}$ can be analytically calculated using equation 2.13. The NMS was calculated to be $\Delta\nu_{457\,\mathrm{NMS}}^{164,162} = 26.95$ MHz and $\Delta\nu_{359\,\mathrm{NMS}}^{164,162} = 34.27$ MHz for both the transitions respectively. Using the empirical relation for the specific mass shift (SMS) $\Delta\nu_{457\,\mathrm{SMS}}^{164,162} = 7$ MHz for the 457 nm transition [61] and the value of the intercept, the SMS for the 359 nm transition was estimated to be $\Delta\nu_{359\,\mathrm{SMS}}^{164,162} = -87.52$ MHz. For the sake of comparison, the ratio of FS parameters and the SMS for two other transitions in Dy at 421 nm and 684 nm, estimated using the same 457 nm transition is shown in Table 5.2.

Large negative mass specific shifts (larger than the NMS) are indicative of a transition involving a change in the f electron shell [61] and a positive ratio of

Table 5.2: Comparision of the ratio of FS parameters and the SMS for i =421 nm, 684 nm and 359 nm estimated using the j =457 nm reference transition

Transition i	$\frac{E_i}{E_j}$	$\Delta\nu_{i\,\mathrm{SMS}}^{164,162}$ (MHz)
421 nm [36]	0.920	11
684 nm [43]	-1.6	-534
359 nm	0.359	-88

Table 5.3: Isotope shifts for the 456.509 nm and the 358.946 nm transition expressed in MHz

Transition	$\Delta\nu_{164-163}$	$\Delta\nu_{164-162}$	$\Delta\nu_{164-161}$	$\Delta\nu_{164-160}$
456.509 nm [61]	-660	-971	-1744	-2020
358.946 nm	-270	-414	-724	-856

the field shift parameters is indicative of a transition involving a change in the s electron shell [36]. Conclusively, the 421 nm transition corresponds to a $(4f^{10}6s6p)$ excited state and the 684 nm transition corresponds to a $(4f^{9}5d6s^{2})$ excited state. The SMS for the 359 nm transition is large and negative whereas the ratio of the field shift parameter is positive. Hence the excited state of this transition can not be conclusively categorized under the know configurations. The theoretical calculations on the prediction of the excited state configuration of the various transitions in Dy was done by J.F. Wyart (1974) [33] in which the excited state of the 359 nm transition was predicted to be doubly excited with the configuration $4f^{9}5d^{2}6s$. As there do not exist any direct theoretical predictions on the trends of SMS and ratio of FS parameters for a doubly excited state involving an f shell electron and a s shell electron, we can not conclude but speculate that the results obtained above are indicative of an $4f^{9}5d^{2}6s$ excited state. From the King plot, using the linear fit, the isotope shifts of the fermionic isotopes can now be determined. All the isotope shifts for the UV transition are shown in Table 5.3.

.

5.3.5 Hyperfine structure

The fermionic isotopes exhibit a hyperfine structure, which can be addressed by laser spectroscopy. As the UV transition is a $\Delta J = 0\,(J = 8 \rightarrow 8)$ transition, the strongest transition between the hyperfine levels is expected to be that which does not change the nuclear spin i.e. a $\Delta F = 0$ transition. This would lead to six hyperfine transitions for each isotope and a hence total of 12 peaks. The assignment of all the 12 peaks, using the general procedure is not possible as these peaks are

Table 5.4: Hyperfine coefficients A and B for the excited state of 359 nm transition

Isotope	A_e (MHz)	B_e (MHz)
^{161}Dy	-101.608	803.224
^{163}Dy	142.669	826.745

closely spaced and have a relatively small amplitude. The frequency shift for the hyperfine transition is given by equation 2.17 as

$$\Delta\nu = (A_e - A_g)K + (B_e - B_g)\frac{\frac{3}{2}K(2K+1) - I(I+1)J(J+1)}{2I(2I-1)J(2J-1)} + \Delta\nu_{\mathrm{IS}}, \quad (5.1)$$

The A and B coefficients of the ground states of the isotopes are given in Table 2.2 and the isotope shifts for the UV transition are determined from the King plot analysis. If the transition frequency corresponding to atleast two hyperfine states of each fermionic isotopes can be assigned, then equation 2.17 can be solved for the excited state coefficients A_e and B_e, which can be used to calculate the position of other peaks. This estimation can then be combined with the general assignment procedure to confirm the position of the peak.

Two hyperfine transition peaks for ^{163}Dy and ^{161}Dy were assigned using the general procedure similar to the bosonic isotopes and are shown in Figure 5.9 and Figure 5.12, which will be described in detail in the next section. Using the frequency shifts of the assigned hyperfine levels, the ground state hyperfine constants and the isotope shifts determined from the King plot analysis, the hyperfine coefficients A_e and B_e coefficients for the excited state were calculated and are shown in Table 5.4 . The ratio of ground state A and B coefficients are $\frac{A_g(163)}{A_g(161)} = -1.4003$ and $\frac{B_g(163)}{B_g(161)} = 1.0561$. The calculated ratios for the excited state of the UV transition are $\frac{A_e(163)}{A_e(161)} = -1.4041$ and $\frac{B_e(163)}{B_e(161)} = 1.0293$ are close to the ground state ratios hence the hyperfine anomaly is negligible. Using the obtained excited state coefficients A_e and B_e, the position of the other peaks can be predicted. These calculated positions of the peaks can be combined with the general assignment procedure to look for the maximum of the peak across the blue detuning and confirm the assignment of a peak.

Hyperfine structure of ^{163}Dy

As there are transitions from the different hyperfine levels of each fermionic isotope, the convention followed is such that a hyperfine transition peak indicated, for

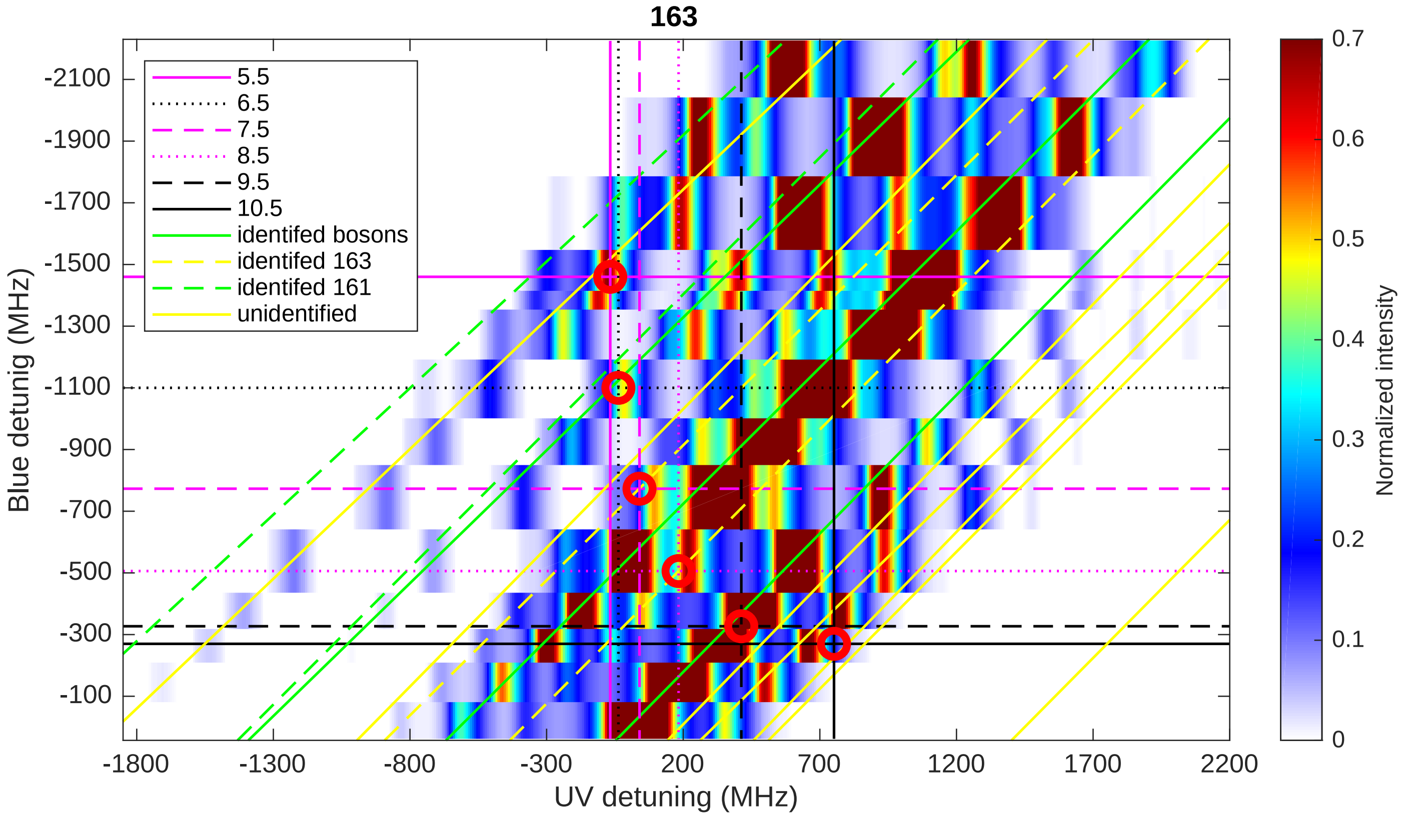

Figure 5.9: Assignment of the hyperfine transitions of ^{163}Dy. The peaks assigned using the general procedure are the F = 7.5 and F = 8.5 transitions. The calculated positions of the peaks of other *F* transitions are indicated. The intersection of the identical markers indicate that both the transitions are addressing the isotope or hyperfine level and are marked as an aid. A fit passing through this intersection indicates the presence of an identified peak. If this identified peak exhibits a maximum in intensity close to this intersection, then the peak is assigned as a transition to the corresponding isotope or hyperfine level.

example as 163 5.5 means that the peak corresponds to a hyperfine transition of ^{163}Dy from $F = 5.5 \rightarrow 5.5$. The identified peaks with positions from lower to higher higher frequency are indicated with increasing number.

As already mentioned first we need to clearly assign atleast two hyperfine transitions as a starting point. For ^{163}Dy, we were able to assign two hypefine transitions corresponding to $F = 7.5$ and $F = 8.5$ via the general procedure and are shown in Figure 5.9. The measured frequency shifts were used to calculate the excited state hyperfine constants. The other hyperfine transitions were calculated using equation 2.17 and marked on the spectrum to check for the maximum of a peak.

We now have a closer look at the spectrum. At the frequency corresponding to the blue and the UV resonance, which is indicated by the intersection of horizontal and vertical markers, both the transitions address the same ground state, where we expect a maximum in intensity. If there is an identified peak, indicated by the fit to the positions of the peaks, and this peak shows a maximum in intensity around this peaks position then the hyperfine transition is identified.

The validation of this method to assign the peaks is justified as the calculated position of the $F = 5.5$ peak corresponds clearly to the maximum of an observed peak in the spectrum and hence this peak is assigned. This goes on to justify the calculated hyperfine constants and the calculated isotope shifts

The calculated positions of other peaks corresponding to $F = 6.5, 9.5, 10.5$ do not clearly indicate the maximum of a peak in the spectrum and hence we take a closer look at the individual spectra at blue detunings around resonance. The UV peak positions follow the ratio of wavevectors for the corresponding blue detuning. For the sake of convenience, when refering to the 3D plots in the context of assignment of hyperfine transitions, the UV frequency axis is adjusted accordingly with the wavevector ratio for the peak positions across the blue detuning to be at the same position. The peaks are numbered in the order of identification from low to high UV frequency detuning.

For the case of $F = 6.5$ and $F = 9.5, 10.5$, this is shown in Figure 5.10 and Figure 5.11. In the case of F = 6.5, the calculated position is close the peak assigned to ^{160}Dy, which could not be resolved within the framework of our set-up but the possibility of existence of a peak can not be ruled out. In the case of F = 9.5, the calculated position falls on the tail of the peak assigned to ^{164}Dy. The asymmetry in the spectral profile of ^{164}Dy due to a relatively larger broadening towards the tail, in the direction of the calculated position of the peak of the could be a possible indication of the existence of a peak, which can not be resolved. There is an unassigned peak close to the calculated position of F = 10.5. Although their positions differ by about 100 MHz, this is assigned. This is justified as we will see later in section 5.6 that this difference is within the experimental error.

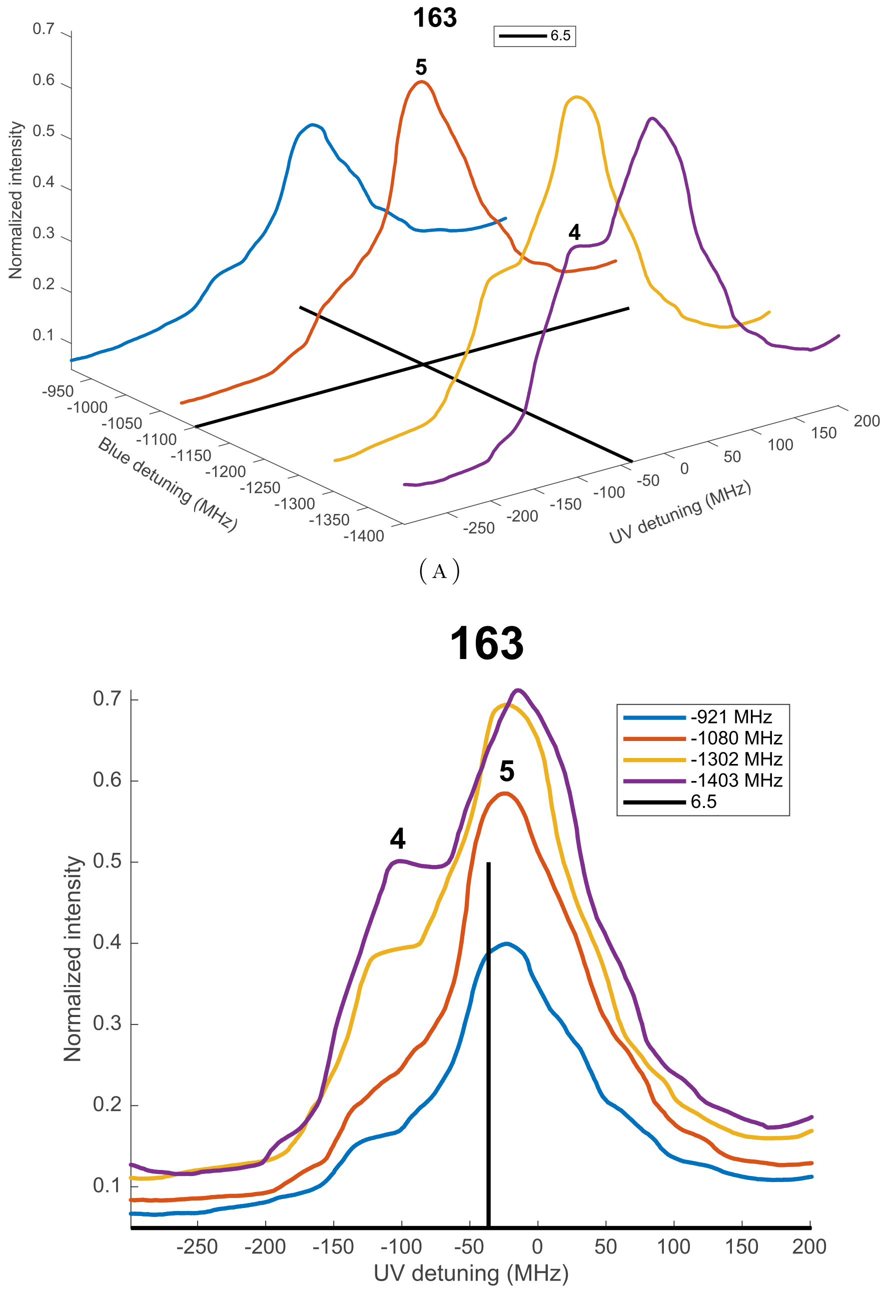

(A)

(B)

Figure 5.10: Shelving spectra for blue detunings around the resonance position corresponding to F = 6.5 of ^{163}Dy. For convince, the UV frequency positions are made to overlap using the wave vector ratio and the corresponding blue detuning. The identified peaks are indicated with the order of peak number idetified from low to high UV frequency detuning. Peak 4 is assigned to F = 9.5 of ^{161}Dy and peak 5 is assigned ^{160}Dy. The calculated position is very close to an assigned peak of ^{160}Dy, which could not be resolved

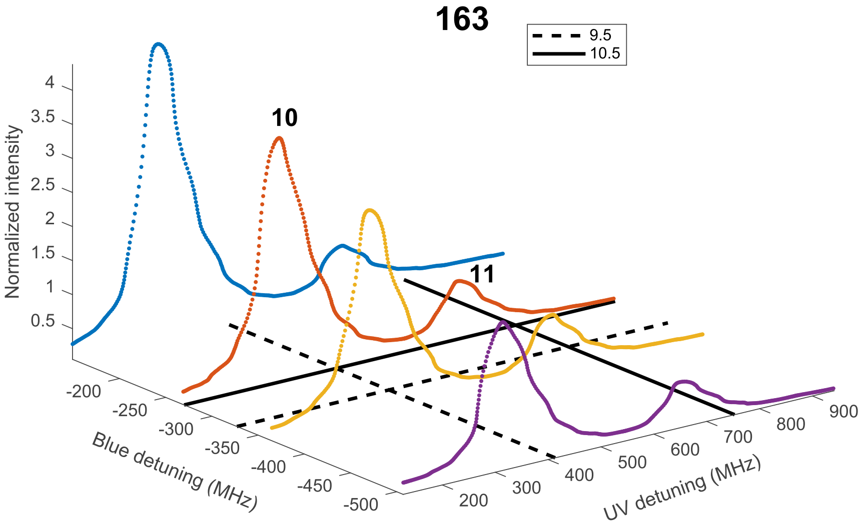

(A)

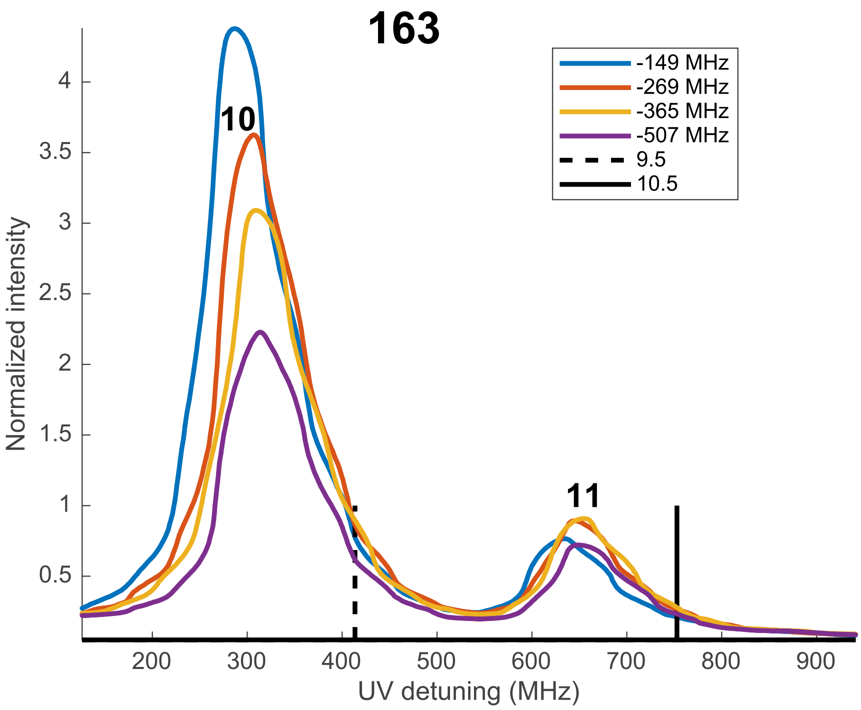

(B)

Figure 5.11: Shelving spectra for blue detunings around the resonance position corresponding to F = 9.5, 10.5 of ^{163}Dy. For convince, the UV frequency positions are made to overlap using the wave vector ratio and the corresponding blue detuning. The identified peaks are indicated with the order of peak number idetified from low to high UV frequency detuning. Peak 10 is assigned to ^{164}Dy but peak 11 remains unassigned and within the experimental error, discussed later, this is assigned to F = 10.5 transition

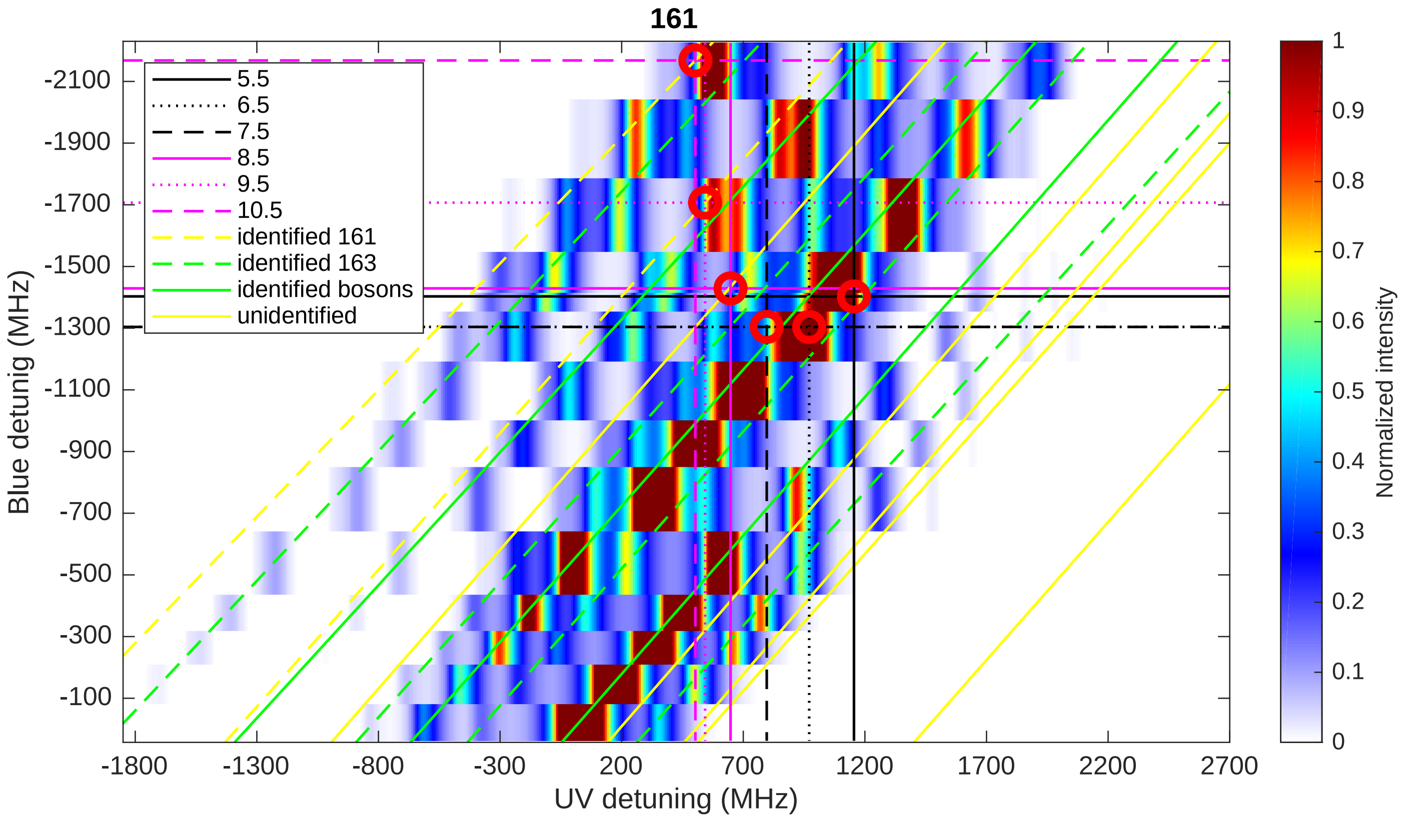

Figure 5.12: Assignment of the hyperfine transitions of ^{161}Dy. The assigned peaks using the general procedure are the $F = 9.5$ and $F = 10.5$ transitions. The intersection of the identical markers indicate that both the transitions are addressing the same isotope or hyperfine level and this is marked as an aid. A fit passing through this intersection indicates the presence of an identified peak. If this identified peak exhibits a maximum close to this intersection, then the peak is assigned as a transition to the corresponding isotope or hyperfine level.

Hyperfine structure of ^{161}Dy

The assignment for the hyperfine transitions of ^{161}Dy is done using the same procedure as ^{163}Dy and is shown in Figure 5.12. As a first step, we could clearly assign two hyperfine transitions corresponding to $F = 9.5$ and $F = 10.5$ using the outlined general procedure, which forms a starting step. The measured frequencies shifts were used to calculate the excited state hyperfine constants, which in turn were used to predict the resonance frequencies of other peaks.
The calculated position of the $F = 8.5$ peak of ^{161}Dy corresponds explicitly to the maximum of an observed peak and hence this transition is now assigned. Once again this provides additional justification to the calculated hyperfine constants and the isotope shifts and stands as a validation of the entire procedure used to assign the transitions.
To assign the peaks corresponding to $F = 5.5, 6.5, 7.5$, where there is no explicit maximum of a peak that can be identified, as discussed previously, we have a closer look at the individual spectra around the blue resonance. This is shown in Figure 5.13.
The peak corresponding to $F = 5.5$ is close to the peak assigned to $F = 8.5$ of ^{163}Dy, same is the case with $F = 6.5$, which lies close peak assigned to ^{162}Dy. These peaks can not be resolved in the obtained spectrum. The peak corresponding to $F = 7.5$, is at the position where no peak was identified and which shows an evident asymmetry in the spectrum. Although an explicit maximum can not be identified, the existence of a peak at the position can not be denied.

Apart from the hyperfine transitions that can not be resolved, there are a few identified peaks that remain unassigned. Apart from the five most stable and abundant isotopes, there exist two more isotopes ^{158}Dy and ^{156}Dy. By calculating the isotope shift of these isotopes using the King plot, it can be verified if there are if the unassigned transitions correspond to any of these isotopes. As we shall see later, we can not assign any transition corresponding to ^{158}Dy and ^{156}Dy. Moreover, an assumption was made that the most probable transitions are the ones that do not change the nuclear spin i.e. $\Delta F = 0$ transitions. Although less probable, according to the dipole selection rules, $\Delta F = \pm 1$ transitions are still possible. The unassigned peaks also exhibit a very low amplitude compared to the other peaks and hence there is a possibility that these peaks correspond to a transition that changes the nuclear spin. By calculating the hyperfine splitting for $\Delta F = \pm 1$ transitions for both the isotopes, we can check if these peaks can be assigned. The most relevant transitions for both the isotopes are shown in Figure 5.14 and Figure 5.20. The convention is followed such that the respective transition is represented

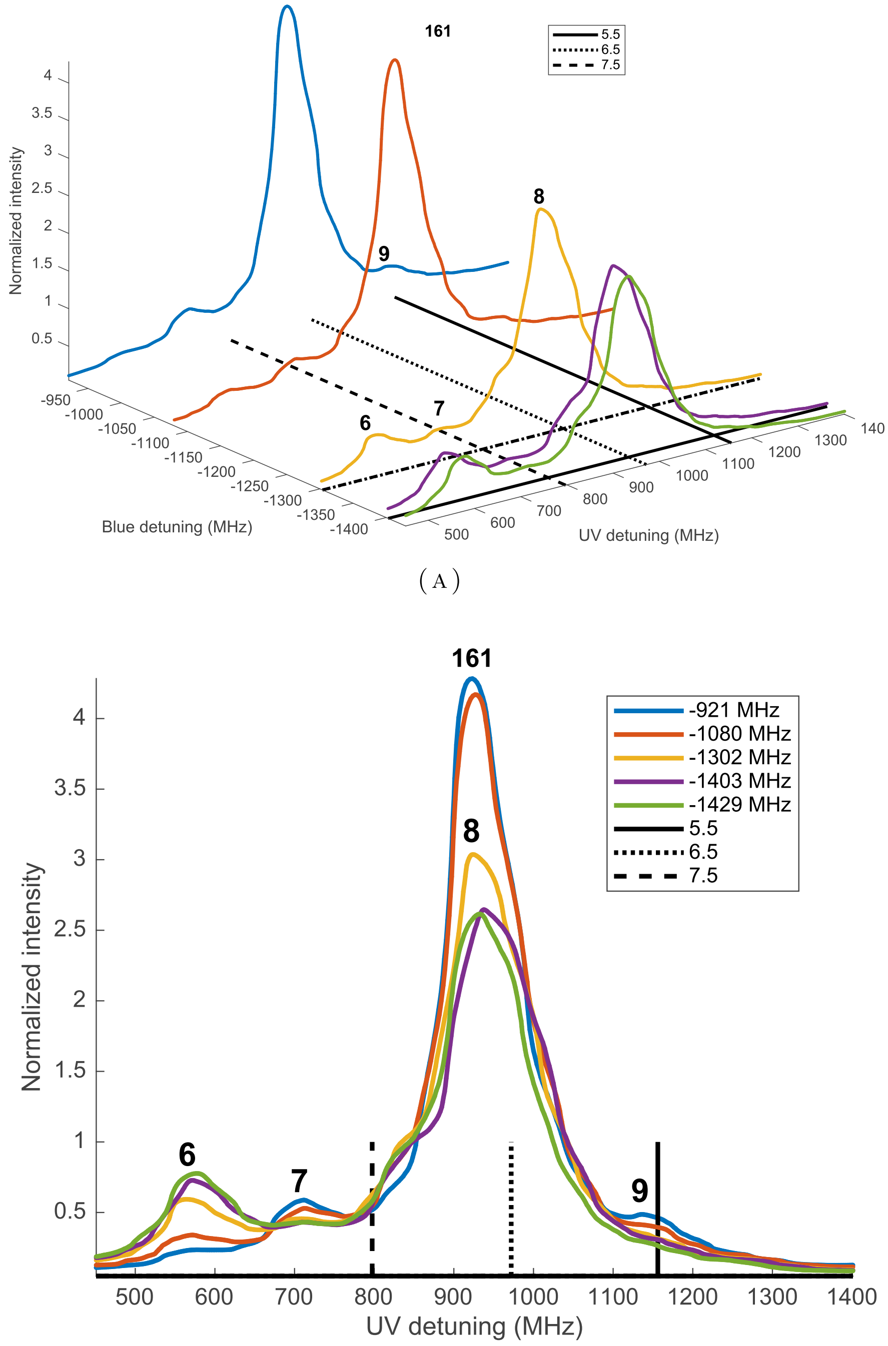

(A)

(B)

Figure 5.13: Shelving spectra for blue detunings around the resonance position corresponding to $F = 5.5, 6.5, 7.5$ of ^{161}Dy. For convince, the UV frequency positions are made to overlap using the wave vector ratio and the corresponding blue detuning. The identified peaks are indicated with the order of peak number idetified from low to high UV frequency detuning. The $F = 5.5, 6.5$ peaks remain unresolved. But the at the position of $F = 7.5$, there is a evidence for the existence of a peak but it cannot be clearly assigned.

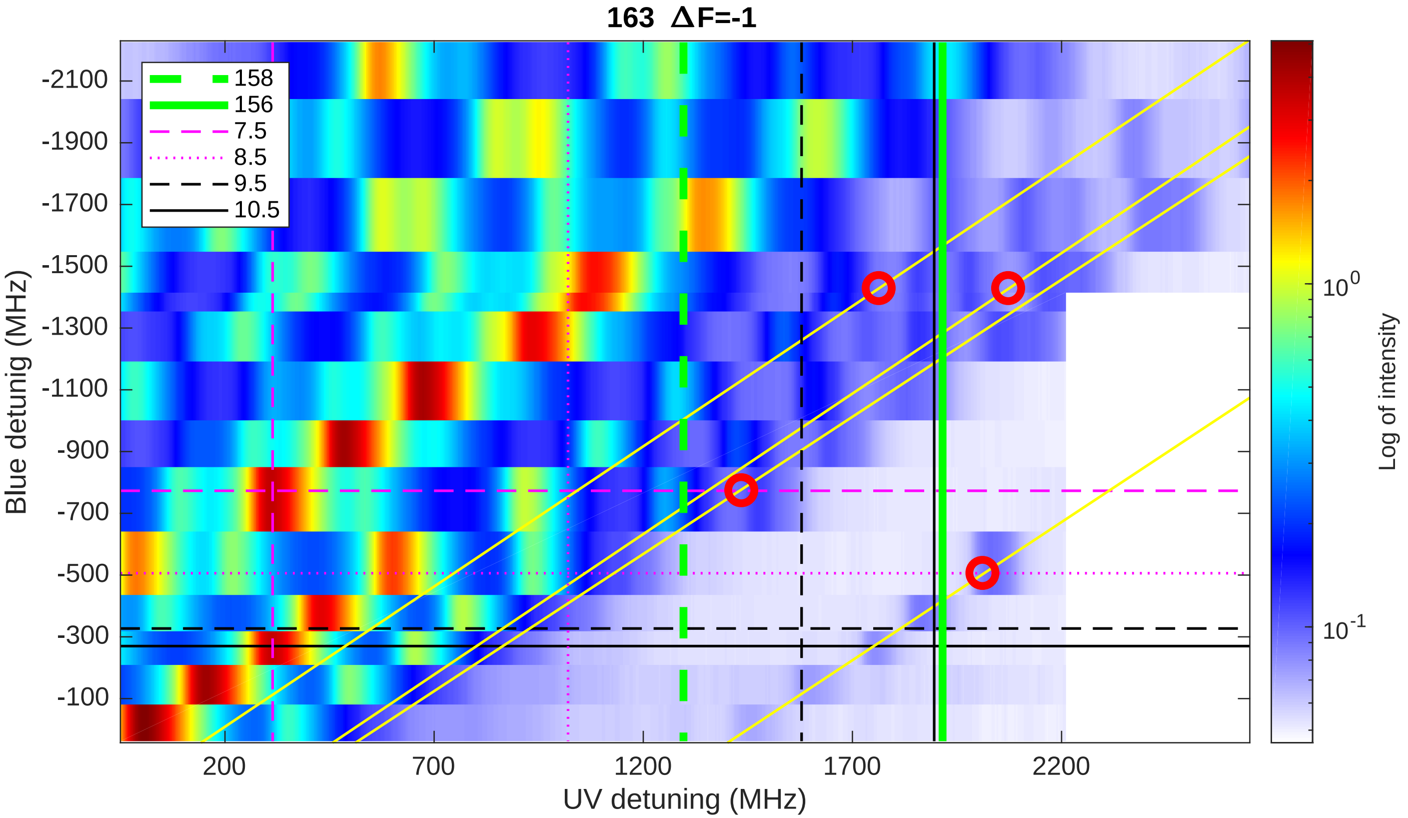

Figure 5.14: The $\Delta F = -1$ transitions for ^{163}Dy with intensity in log scale. The unassigned peaks along with the calculated hyperfine splitting and other isotope shifts are shown. The markers indicated on the linear fits are the positions of the highest intensity observed of the respective peaks. For $F = 8.5 \rightarrow 7.5$, a peak is predicted but the assignment remains elusive as a clear maximum cannot be found.

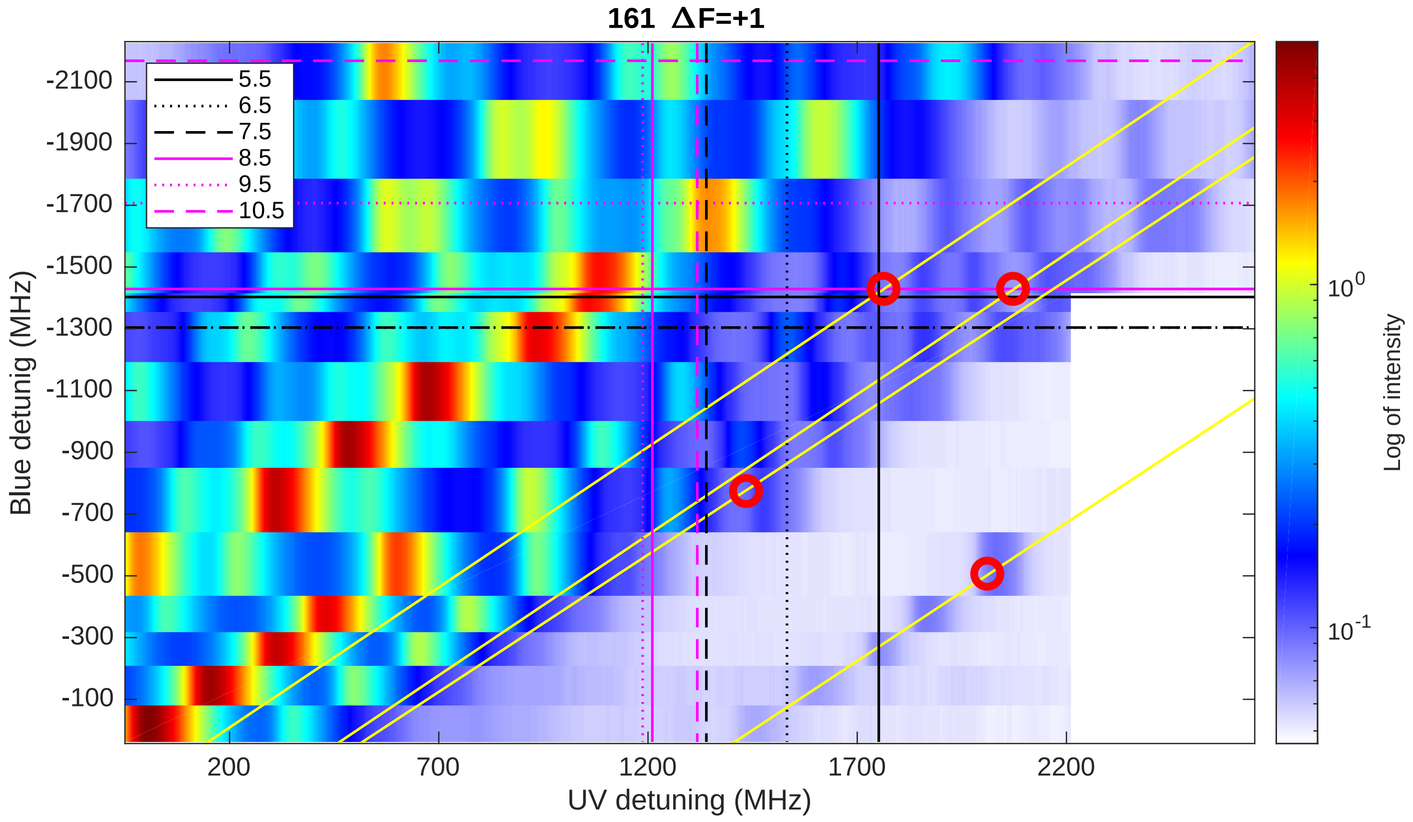

FIGURE 5.15: The $\Delta F = +1$ transitions for ^{161}Dy. The unassigned peaks along with the calculated hyperfine splitting and other isotope shifts are shown. The markers indicated on the linear fits are the positions of the highest intensity observed of the respective peaks. One of the identified peaks is predicted around the transition frequency for $F = 5.5 \rightarrow 6.5$ but as an explicit maximum cannot be identified, the assignment remains ambiguous.

by the ground state F value. For example, for ^{163}Dy, the $\Delta F = -1$ transitions are shown and $F = 7.5$ means a transition from $F = 7.5 \rightarrow 6.5$. Similarly, for ^{161}Dy, the $\Delta F = +1$ transitions are shown and $F = 5.5$ means a transition from $F = 5.5 \rightarrow 6.5$. The isotope shifts of ^{158}Dy and ^{156}Dy for the blue transitions are -2868 MHz and -4300 respectively [36] and the calculated isotope shifts for the UV transitions are indicated in the respective figures. As it can be clearly seen, there is no identified peak around these positions.

In the case of $\Delta F = -1$ transitions for ^{163}Dy, the position fit of one of the identified peaks is close to the $F = 8.5$ transition. For the case of $\Delta F = +1$ transitions for ^{161}Dy, the position fit of one of the identified peaks is close to the $F = 5.5$ transition.

However, we cannot conclude anything about the assignment of these peaks as there we cannot resolve the spectrum to find a maximum of these peaks. There still exist two more observed peaks, that remain unassigned. As of now we cannot speculate any other origin for the existence of these peaks.

Both the assigned and unresovled $\Delta F = 0$ hyperfine transitions of the isotopes are summarized in the Table 5.5.

The hyperfine structure of the excited state corresponding to the UV transition of ^{163}Dy and ^{161}Dy are shown in Figure 5.16.

From 2.6, the interval rule arising purely from the magnetic dipole contribution to the hyperfine structure is given by $\Delta E_{MD}(F) - \Delta E_{MD}(F-1) = AF$. The electric quadrupole interaction leads to a departure from the interval rule as discussed in section 2.2.2. The deviation from the interval rule for ^{163}Dy and ^{161}Dy is summarized in Table 5.6 and Table 5.7 respectively. The departure from the interval rule is a measure of the electric quadrupole interaction constant B.

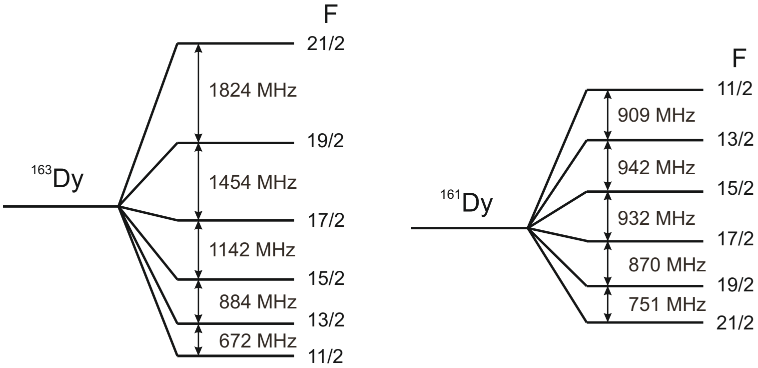

FIGURE 5.16: The hyperfine structure of the excited state corresponding to the UV transition of ^{163}Dy and ^{161}Dy calculated from the measured hyperfine transition frequencies.

TABLE 5.5: Frequency shifts in MHz for the hyperfine transitions for ^{163}Dy and ^{161}Dy. The notation followed is $\Delta\nu_{164-i} = \nu_{164} - \nu_i$

F	$\Delta\nu_{F,164-163}$ (MHz)	$\Delta\nu_{F,164-161}$ (MHz)
5.5	68	-1154
6.5	38	-970
7.5	-39	-795
8.5	-182	-647
9.5	-412	-542
10.5	-750	-502

TABLE 5.6: The departure from the interval rule for ^{163}Dy quantified by the difference in the the calculated frequency shift AF, as predicted by the interval rule and the measured frequency shift for the hyperfine structure of the excited state and expressed.

Interval	Measured (MHz)	Calculated A_eF (MHz)	Departure (MHz)
6.5 – 5.5	672	927	-255
7.5 – 6.5	884	1070	-186
8.5 – 7.5	1142	1213	-71
9.5 – 8.5	1454	1355	98
10.5 – 9.5	1824	1498	326

TABLE 5.7: The departure from the interval rule for ^{161}Dy quantified by the difference in the the calculated frequency shift AF, as predicted by the interval rule and the measured frequency shift for the hyperfine structure of the excited state and expressed.

Interval	Measured (MHz)	Calculated A_eF (MHz)	Departure (MHz)
6.5 – 5.5	-909	-660	-248
7.5 – 6.5	-942	-762	-180
8.5 – 7.5	-932	-864	-69
9.5 – 8.5	-870	-965	95
10.5 – 9.5	-751	-1067	315

5.4 Characterizing the dependence of the spectrum on various parameters

Here, we are going to discuss the dependence of the properties of observed spectrum, especially the FWHM, on various beam parameters and temperature. It is straight forward to expect that the peak amplitude decreases on decreasing the blue or

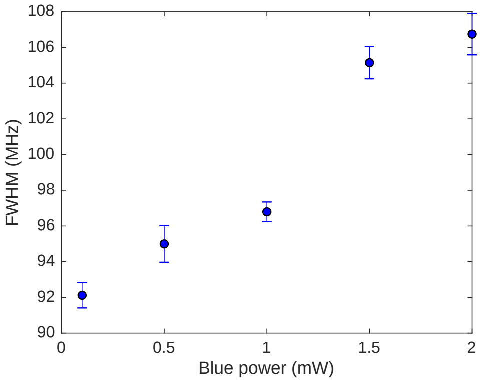

Figure 5.17: Dependence of the FWHM of the peak corresponding to ^{164}Dy on the blue beam power, at an oven temperature of 1250 °C and UV beam power of 50 mW.

the UV beam power and also on decreasing the temperature. For the blue beam parameters used in the experiment, the intensity approaches the saturation intensity for a beam power of about 1.94 mW. To have a signal with good SNR as well as to not power broaden it, the blue beam power is chosen less than 1.94 mW. The dependence of the FWHM of the transition corresponding to ^{164}Dy on reducing blue power is shown in Figure 5.17.

It is observed that the FWHM does not show a very strong dependence and decreases on decreasing the blue power. Hence the blue beam power is fixed at 0.1 mW so that we have a good SNR and a low FWHM. Although the shelving method is not a true Doppler free spectroscopy, it is definitely in the sub-Doppler broadening regime. Hence we would expect a very weak dependence of the FWHM of the spectrum on changing oven temperature and this is shown in Figure 5.18. To check for any saturation effects on the shelving spectrum caused due to the UV beam power, the FWHM and the amplitude of the ^{164}Dy peak are shown in Figure 5.19. As there are no visible saturation effects on the peak amplitude and the FWHM does not strongly depend on the UV beam power. The UV beam power is chosen to be the maximum. One thing that has to be mentioned about the FWHM estimated for all the cases is by fitting a Lorentzian function to the peak. However for these measurements, the ULE cavity transmission peaks were not used for the frequency calibration and hence it is more useful to look at the overall trend. Any drifts in the center position of the UV frequency, would lead to significant errors as the scan is considerably non-linear.

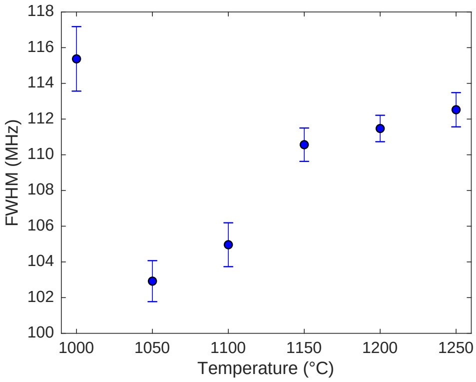

Figure 5.18: Dependence of the FWHM of the peak corresponding to ^{164}Dy on the temperature of the oven at blue beam power of 0.5 mW and UV beam power of 50 mW.

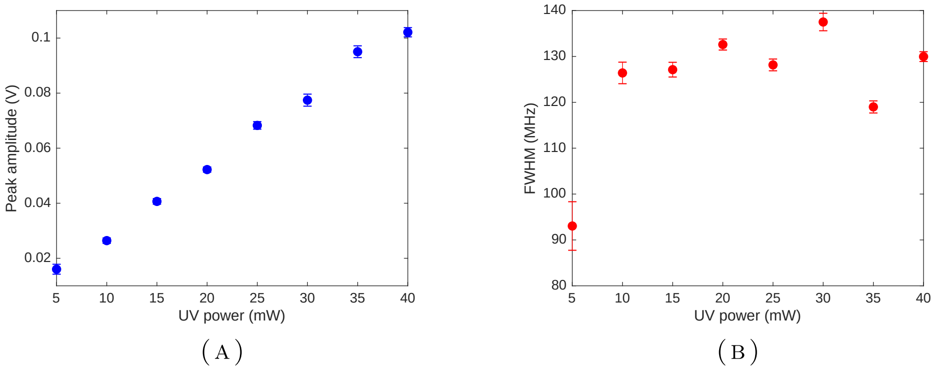

(a)

(b)

Figure 5.19: The dependence of the peak amplitude and the FWHM of the ^{164}Dy transition peak with changing UV power at a blue beam power of 0.5 mW.

5.5 Estimating the lifetime of the excited state

As discussed in section 5.3, using shelving method, the minimum FWHM that can be achieved is approxiamtely 38 MHz. Hence, using the shelving method, the natural linewidth of the transition or the lifetime τ of the excited state of the UV transition cannot be directly measured. To obtain a direct estimate of the lifetime of the excited state, we employ a different method. Apart from the blue beam on resonance, the UV beam frequency instead of being scanned is now held on resonance with the ^{164}Dy transition. When the UV beam is switched off, the atoms from the excited state corresponding to the UV transition decay and now exclusively scatter only the blue beam. Hence the transmission signal would decay because of the increased absorption of the blue beam. This decay of the atoms

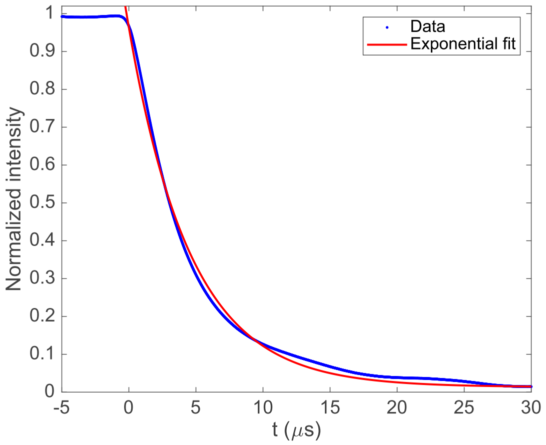

Figure 5.20: Decay of the transmission signal obtained by chopping the light at 2 kHz. The data is fit to an exponential to estimate the lifetime.

should be a direct measure of the lifetime of the excited state corresponding to the UV transition. The UV beam is chopped using an AOM and the decay signal is averaged over 10000 shots. The signal was recorded with an photodiode[2] used at a gain of 30 dB, which corresponds to a 3 dB bandwidth of $f_{3\,\mathrm{dB}} = 260\,\mathrm{kHz}$ leading to a rise time of $\tau_r = \frac{0.35}{f_{3\,\mathrm{dB}}} = 1.3\,\mu\mathrm{s}$. To account for the rise time of the photodiode and the AOM, the chopped UV beam is detected as a reference simultaneously with the same photodiode and with same bandwidth. By fitting an exponential to the detected reference signal, a time constant of $(\tau_1 = 1.200(64))\,\mu\mathrm{s}$ was determined. The obtained decay of the atoms is fit with a exponential containing two time constants τ_1 and τ_2, where τ_2 gives an estimate of the lifetime of the excited state of the atoms, which was found to be 3.182(141). An upperbound of the natural linewidth of the excited state of the UV transition was estimated to be $50 \pm 2\,\mathrm{kHz}$, which is close to the value measured in [32].

In our case, the transit time, the AOM switching time and the rise time of the photodiode, all are of the same order of the lifetime. It was ensured that the transit time is greater than the lifetime and photodiode rise time and the AOM switching time is smaller than the lifetime. The AOM rise time is included in the model, which is only a rough estimation and cannot be extensively justified. Also, the AOM rise time is estimated by observing the chopped UV beam whereas we detect the blue beam. But the photodiode has a difference response for different wavelengths and this is not included in our estimate. A better estimate can be obtained by increasing the transit time and by decreasing the AOM and the photodiode rise

---

[2] PDA36A2 (Thorlabs)

time.

5.6 Discussion of the uncertainty in the measurements

Table 5.8: Isotope shifts with errors for the 358.946 nm transition

$\Delta\nu_{164-163}$ (MHz)	$\Delta\nu_{164-162}$ (MHz)	$\Delta\nu_{164-161}$ (MHz)	$\Delta\nu_{164-160}$ (MHz)
-270 ± 90	-414 ± 94	-724 ± 102	-856 ± 106

.

Table 5.9: Hyperfine shifts with errors for the 358.946 nm transition

F	$\Delta\nu_{F,164-163}$ (MHz)	$\Delta\nu_{F,164-161}$ (MHz)
5.5	68 ± 82	-1154 ± 144
6.5	38 ± 83	-970 ± 109
7.5	-39 ± 84	-795 ± 104
8.5	-182 ± 88	-647 ± 100
9.5	-412 ± 94	-542 ± 97
10.5	-750 ± 103	-502 ± 96

Table 5.10: The ratio of FS parameters and the SMS for $i = 359$ nm estimated using the j =457 nm reference transition

Transition i	$\frac{E_i}{E_j}$	$\Delta\nu_{i\,\mathrm{SMS}}^{164,162}$ (MHz)
359 nm	0.359 ± 0.271	-88 ± 117

Here, we are going to discuss the different sources of error and their contribution to the measurement of frequency which is the primary quantity measured in this work. The linewidth of the Ti:Sa beam was specified to be 100 kHz over 100 μs. Each UV frequency scan is for about one second. The integration of the laser linewidth to this time is not straight forward but its contribution is expected to be small as the observed width is larger. The error in frequency measurement of the blue beam is from the determination of the resonance frequency position of the ^{164}Dy transition, because for the other positions we use the measured isotope shifts. An estimate on the error in determination of the resonance frequency position is given as 2 MHz

Table 5.11: Hyperfine coefficients A and B for the excited state of 359 nm transition

Isotope	A_e (MHz)	B_e (MHz)
^{161}Dy	-101.608 ± 171	803.224 ± 178
^{163}Dy	142.669 ± 152	826.745 ± 158

coming from the largest uncertainty in determining the peak position by fitting it. One of the largest contributions to the uncertainty in the UV frequency measurements arises from the frequency scan of the Ti:Sa laser of the UV beam. As discussed in section 4.2.1, we use the ULE cavity transmission peaks for the calibration of the frequency. The uncertainty in identifying the cavity peak positions can be estimated by the FWHM of the peaks which was about 2 MHz. The drifts of the center frequency position over time are compensated by ULE cavity peaks. However the non-linearity of the scan can only be estimated but not compensated using the ULE cavity. Across the scans a maximum non-linearity of about 3.3% was estimated and this is so far the largest contributor to the error in frequency. Hence fixing the error on the absolute frequency from the non-linearity of the scan, the error for the shifts can be estimated using simple error propagation. The isotope shifts with respect to the ^{164}Dy transitions frequency, along with the error are shown in Table 5.8. The the frequency shifts for hyperfine structure with respect to ^{164}Dy with error are shown in Table 5.9. Due to the error in the determination of isotope shifts, the King plot would have a corresponding error. The uncertainty in the determinig the ratio of field shift parameters and the specific mass shift is shown in Table 5.10. By simple error prorogation, the estimated error in determining the excited state hyerfine coefficients is summarized in Table 5.11.

6 Conclusion and Outlook

In the work presented as a part of this thesis, a powerful spectroscopic technique to detect weak transitions by means of a strong transition was demonstrated by extensive characterization of a UV transition at 359 nm in Dy atoms. This is an essential preliminary step for the realization of a predicted magic wavelength for the clock transition at 1001 nm to the realize the goal of single-site resolution using quantum gas microscope for ultracold Dy atoms in an UV lattice.

The success of the shelving method over conventional spectroscopic techniques to detect a weak transition was demonstrated by obtaining the UV spectrum in absorption and fluorescence. Using a modulation technique, a high resolution UV spectrum was obtained. By measuring the isotope shifts shown in Table 6.1, a King plot analysis was performed using a reference transition to obtain the ratio of field shift parameters and the specific mass shift. A small positive field shift parameter ratio of (0.359 ± 0.271) and a large negative specific mass shift of (-88 ± 117) MHz were obtained, which did not conclusively indicate to a previously know excited state configuration in Dy. This could be a hint towards the theoretically predicted doubly excited state, well within the ionization limit, for the UV transition from $4f^{10}6s^2 \rightarrow 4f^9 5d^2 6s$. From the assignment of the hyperfine transitions, the hyperfine constants for the excited state of the fermionic isotopes were determined and are shown in Table 6.2. All the frequency measurements are presented with a conservative error estimate coming predominantly from the non-linearity of the frequency scan. By measuring the decay of the excited state atoms, the upper bound of the natural linewidth of the transition was estimated to be (50 ± 2) kHz. To the best of our knowledge, this is the first extensive characterization of the UV transition in Dy at 359 nm including measurements on the isotope shifts and the excited state hyperfine constants.

TABLE 6.1: Isotope shifts with errors for the 358.946 nm transition

$\Delta\nu_{164-163}$ (MHz)	$\Delta\nu_{164-162}$ (MHz)	$\Delta\nu_{164-161}$ (MHz)	$\Delta\nu_{164-160}$ (MHz)
-270 ± 90	-414 ± 94	-724 ± 102	-856 ± 106

Table 6.2: Hyperfine coefficients A and B for the excited state of 359 nm transition

Isotope	A_e (MHz)	B_e (MHz)
^{161}Dy	-101.608 ± 171	803.224 ± 178
^{163}Dy	142.669 ± 152	826.745 ± 158

Further improvements can be done by correcting the non-linearity of the frequency scan, which would decrease the error in the frequency measurements. In order to have an atomic beam with smaller divergence, the mechanical design of the collimation scheme using apertures can be improved upon. This would reduce the residual Doppler broadening and should improve the assignment procedure of the peaks.

It would be interesting to explore the theoretical aspects of such doubly excited states, to understand its origin and the consequences on the spectral properties. This is because the theory in the case of auto-ionization states explains the observed highly asymmetric absorption profiles in terms of interference between the autoionization state and a continuum [51] [52]. In our case, as the excited state of the UV transition is a doubly excited state within the ionization limit, it would be interesting to compare the spectral properties to that of an autoionization state or to a singly excited state. A better understanding of such an excited state can be helpful in predicting the trends in ratio of field shift parameters and specific mass shift which are the benchmarks to describe the electronic nature of the excited state.

As we have already seen by adding a retro-reflected UV beam, the spectrum showed a doublet which exhibits an avoided crossing kind of a feature across the blue resonance, of about 32 MHz much larger than the Rabi frequencies of the blue beams. A further investigation on the origin of this feature by verifying the dependence of the minimum on the Rabi frequency can be helpful in understanding the origin of such a feature. A similar spectrum was obtained for an additional retro-reflected UV beam and by scanning the UV frequency and is shown in Figure 6.1. Such a feature has to be investigated in detail considering any possible interference effects. An improved spectrum obtained by frequency modulation of such a feature, which shows a derivative signal can be used to lock the laser.

Furthermore, there are reportedly two more UV transitions around the region at 362 nm and 370 nm [32], both of which can be addressed using our UV laser system and hence can be investigated. The 362 nm transition is two times weaker than the 359 nm transition but thanks to shelving method which gives an amplification of the signal inversely proportional to the natural linewidth of the transition, the

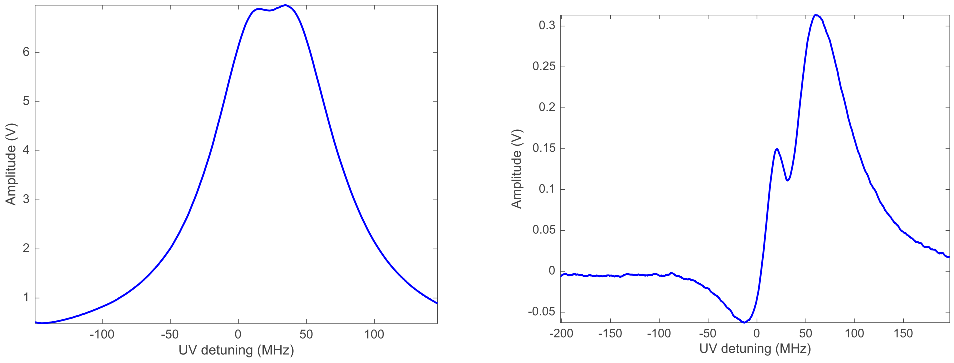

(A) (B)

FIGURE 6.1: Transition corresponding to ^{164}Dy upon adding a retro-reflected UV beam by (A) amplitude modulation and (B) frequency modulation

transition could well be detected. The 370 nm transition is a very broad transition comparable to the blue transition in Dy. This is also an interesting transition to probe because theoretical predictions disagree with existence of this transition as it would cause significant change in the polarizability of ^{164}Dy at 1064 nm[1] and does not appear in any neighboring lanthanide [83].

In the far future, an UV lattice is planned to be implemented for ultracold Dy atoms at the magic wavelength. For this, the first step would be to characterize the other ground state transitions in the UV region followed by the characterization of the 1001 nm transition. The next step would be to find the optimal magic wavelength by performing extensive polarizability measurements using the UV and the 1001 nm beams which would then be used to characterize the proposed imaging for single-site resolution using a quantum gas microscope.

---

[1] Maxence Lepers [private communication]

Bibliography

[1] M. H. Anderson, J. R. Ensher, M. R. Matthews, C. E. Wieman, and E. A. Cornell. Observation of bose-einstein condensation in a dilute atomic vapor. *Science*, 269(5221):198–201, 1995.

[2] K. B. Davis, M. O. Mewes, M. R. Andrews, N. J. van Druten, D. S. Durfee, D. M. Kurn, and W. Ketterle. Bose-einstein condensation in a gas of sodium atoms. *Phys. Rev. Lett.*, 75:3969–3973, Nov 1995.

[3] B. DeMarco and D. S. Jin. Onset of fermi degeneracy in a trapped atomic gas. *Science*, 285(5434):1703–1706, 1999.

[4] M. R. Andrews, C. G. Townsend, H.-J. Miesner, D. S. Durfee, D. M. Kurn, and W. Ketterle. Observation of interference between two bose condensates. *Science*, 275(5300):637–641, 1997.

[5] K. W. Madison, F. Chevy, W. Wohlleben, and J. Dalibard. Vortex formation in a stirred bose-einstein condensate. *Phys. Rev. Lett.*, 84:806–809, Jan 2000.

[6] M. W. Zwierlein, J. R. Abo-Shaeer, A. Schirotzek, C. H. Schunck, and W. Ketterle. Vortices and superfluidity in a strongly interacting fermi gas. *Nature*, 435(7045):1047–1051, 2005.

[7] Christian Gross and Immanuel Bloch. Quantum simulations with ultracold atoms in optical lattices. *Science*, 357(6355):995–1001, 2017.

[8] Markus Greiner, Olaf Mandel, Tilman Esslinger, Theodor W. Hänsch, and Immanuel Bloch. Quantum phase transition from a superfluid to a mott insulator in a gas of ultracold atoms. *Nature*, 415(6867):39–44, 2002.

[9] Juliette Billy, Vincent Josse, Zhanchun Zuo, Alain Bernard, Ben Hambrecht, Pierre Lugan, David Clément, Laurent Sanchez-Palencia, Philippe Bouyer, and Alain Aspect. Direct observation of anderson localization of matter waves in a controlled disorder. *Nature*, 453(7197):891–894, 2008.

[10] Waseem S. Bakr, Jonathon I. Gillen, Amy Peng, Simon Fölling, and Markus Greiner. A quantum gas microscope for detecting single atoms in a hubbard-regime optical lattice. *Nature*, 462(7269):74–77, 2009.

[11] S. Inouye, M. R. Andrews, J. Stenger, H.-J. Miesner, D. M. Stamper-Kurn, and W. Ketterle. Observation of feshbach resonances in a bose-einstein condensate. *Nature*, 392(6672):151–154, 1998.

[12] Axel Griesmaier, Jörg Werner, Sven Hensler, Jürgen Stuhler, and Tilman Pfau. Bose-einstein condensation of chromium. *Phys. Rev. Lett.*, 94:160401, Apr 2005.

[13] J. Stuhler, A. Griesmaier, T. Koch, M. Fattori, T. Pfau, S. Giovanazzi, P. Pedri, and L. Santos. Observation of dipole-dipole interaction in a degenerate quantum gas. *Phys. Rev. Lett.*, 95:150406, Oct 2005.

[14] Jürgen Stuhler, Axel Griesmaier, Tobias Koch, Marco Fattori, and Tilman Pfau. Magnetostriction in a degenerate quantum gas. *Journal of Magnetism and Magnetic Materials*, 316(2):429 – 432, 2007. Proceedings of the Joint European Magnetic Symposia.

[15] T. Lahaye, J. Metz, B. Fröhlich, T. Koch, M. Meister, A. Griesmaier, T. Pfau, H. Saito, Y. Kawaguchi, and M. Ueda. d-wave collapse and explosion of a dipolar bose-einstein condensate. *Phys. Rev. Lett.*, 101:080401, Aug 2008.

[16] M. Fattori, T. Koch, S. Goetz, A. Griesmaier, S. Hensler, J. Stuhler, and T. Pfau. Demagnetization cooling of a gas. *Nature Physics*, 2:765 EP –, Oct 2006. Article.

[17] Mingwu Lu, Nathaniel Q. Burdick, Seo Ho Youn, and Benjamin L. Lev. Strongly dipolar bose-einstein condensate of dysprosium. *Phys. Rev. Lett.*, 107:190401, Oct 2011.

[18] K. Aikawa, A. Frisch, M. Mark, S. Baier, A. Rietzler, R. Grimm, and F. Ferlaino. Bose-einstein condensation of erbium. *Phys. Rev. Lett.*, 108:210401, May 2012.

[19] Igor Ferrier-Barbut, Holger Kadau, Matthias Schmitt, Matthias Wenzel, and Tilman Pfau. Observation of quantum droplets in a strongly dipolar bose gas. *Phys. Rev. Lett.*, 116:215301, May 2016.

[20] Matthias Schmitt, Matthias Wenzel, Fabian Böttcher, Igor Ferrier-Barbut, and Tilman Pfau. Self-bound droplets of a dilute magnetic quantum liquid. *Nature*, 539:259 EP –, Nov 2016.

[21] L. Santos, G. V. Shlyapnikov, and M. Lewenstein. Roton-maxon spectrum and stability of trapped dipolar bose-einstein condensates. *Phys. Rev. Lett.*, 90:250403, Jun 2003.

[22] L. Chomaz, R. M. W. van Bijnen, D. Petter, G. Faraoni, S. Baier, J. H. Becher, M. J. Mark, F. Wächtler, L. Santos, and F. Ferlaino. Observation of roton mode population in a dipolar quantum gas. *Nature Physics*, 14(5):442–446, 2018.

[23] L. Tanzi, E. Lucioni, F. Famà, J. Catani, A. Fioretti, C. Gabbanini, R. N. Bisset, L. Santos, and G. Modugno. Observation of a dipolar quantum gas with metastable supersolid properties. *Phys. Rev. Lett.*, 122:130405, Apr 2019.

[24] Fabian Böttcher, Jan-Niklas Schmidt, Matthias Wenzel, Jens Hertkorn, Mingyang Guo, Tim Langen, and Tilman Pfau. Transient supersolid properties in an array of dipolar quantum droplets. *Phys. Rev. X*, 9:011051, Mar 2019.

[25] L. Chomaz, D. Petter, P. Ilzhöfer, G. Natale, A. Trautmann, C. Politi, G. Durastante, R. M. W. van Bijnen, A. Patscheider, M. Sohmen, M. J. Mark, and F. Ferlaino. Long-lived and transient supersolid behaviors in dipolar quantum gases. *Phys. Rev. X*, 9:021012, Apr 2019.

[26] Mingyang Guo, Fabian Böttcher, Jens Hertkorn, Jan-Niklas Schmidt, Matthias Wenzel, Hans Peter Büchler, Tim Langen, and Tilman Pfau. The low-energy goldstone mode in a trapped dipolar supersolid. *Nature*, 574(7778):386–389, 2019.

[27] G. Natale, R. M. W. van Bijnen, A. Patscheider, D. Petter, M. J. Mark, L. Chomaz, and F. Ferlaino. Excitation spectrum of a trapped dipolar supersolid and its experimental evidence. *Phys. Rev. Lett.*, 123:050402, Aug 2019.

[28] L. Tanzi, S. M. Roccuzzo, E. Lucioni, F. Famà, A. Fioretti, C. Gabbanini, G. Modugno, A. Recati, and S. Stringari. Supersolid symmetry breaking from compressional oscillations in a dipolar quantum gas. *Nature*, 574(7778):382–385, 2019.

[29] S. Baier, M. J. Mark, D. Petter, K. Aikawa, L. Chomaz, Z. Cai, M. Baranov, P. Zoller, and F. Ferlaino. Extended bose-hubbard models with ultracold magnetic atoms. *Science*, 352(6282):201–205, 2016.

[30] D. Studer, L. Maske, P. Windpassinger, and K. Wendt. Laser spectroscopy of the 1001-nm ground-state transition in dysprosium. *Phys. Rev. A*, 98:042504, Oct 2018.

[31] N. Lundblad, M. Schlosser, and J. V. Porto. Experimental observation of magic-wavelength behavior of ^{87}Rb atoms in an optical lattice. *Phys. Rev. A*, 81:031611, Mar 2010.

[32] G. Nave M.E. Wickliffe, J.E. Lawler. Atomic transition probabilities for Dy I and Dy II. *Journal of Quantitative Spectroscopy Radiative Transfer*, 66:242, 1999.

[33] J.F. Wyart. Interpretation du spectre de dy i: I. etude des configurations impaires. *Physica*, 75(2):371 – 385, 1974.

[34] Warren Nagourney, Jon Sandberg, and Hans Dehmelt. Shelved optical electron amplifier: Observation of quantum jumps. *Physical Review Letters*, 56(26):2797–2799, 1986.

[35] J C Bergquist, Randall G Hulet, Wayne M Itano, and D J Wineland. PHYSICAL REVIEW LETTERS Observation of Quantum Jumps in a Single Atom. 57(14):2–5, 1986.

[36] Arman Cingöz Nathan Leefer and Dmitry Budker. Measurement of hyperfine structure and isotope shifts in the dy 421nm transition. *Optics Letters*, 34(17):2548–2550, 2009.

[37] *CRC Handbook of Chemistry and Physics.* CRC Press, New York, 2010.

[38] B. H. Billings and D. E. Gray. *American Institute of Physics handbook.* series:McGraw-Hill handbooks. (McGraw-Hill, New York, Oxford, 1972.

[39] http://www.webelements.com/dysprosium/.

[40] H.Haken and H. Wolf. *The Physics of Atoms and Quanta.* Springer Verlag, 2005.

[41] R. W.C. Martin and L.Hagan. *Atomic Energy Levels - The Rare-Earth Elements.* NSRDS-NBS, 1978.

[42] Mingwu Lu, Seo Ho Youn, and Benjamin L. Lev. Spectroscopy of a narrow-line laser-cooling transition in atomic dysprosium. *Phys. Rev. A*, 83:012510, Jan 2011.

[43] Henn E. A. L. Billy J Kadau H Maier T Griesmaier A Schmitt, M and T Pfau. Spectroscopy of a narrow-line optical pumping transition in atomic dysprosium. *Optics Letters*, 38(5):637–639, 2013.

[44] V. A. Dzuba and V. V. Flambaum. Theoretical study of some experimentally relevant states of dysprosium. *Phys. Rev. A*, 81:052515, May 2010.

[45] A. Kramida, Yu. Ralchenko, J. Reader, and and NIST ASD Team. NIST Atomic Spectra Database (ver. 5.6.1), [Online]. Available: `https://physics.nist.gov/asd` [2019, September 23]. National Institute of Standards and Technology, Gaithersburg, MD., 2018.

[46] Gregor Tanner, Klaus Richter, and Jan-Michael Rost. The theory of two-electron atoms: between ground state and complete fragmentation. *Rev. Mod. Phys.*, 72:497–544, Apr 2000.

[47] F. G. Fender and J. P. Vinti. Doubly-excited states in helium. *Phys. Rev.*, 46:77–78, Jul 1934.

[48] J. D. Garcia and J. E. Mack. Doubly excited states in lithium. *Phys. Rev.*, 138:A987–A991, May 1965.

[49] I. Sánchez and F. Martín. The doubly excited states of the h2 molecule. *The Journal of Chemical Physics*, 106(18):7720–7730, 1997.

[50] R. P. Madden and K. Codling. New autoionizing atomic energy levels in he, ne, and ar. *Phys. Rev. Lett.*, 10:516–518, Jun 1963.

[51] Ph Durand, I Paidarová, and F X Gadéa. Theory of fano profiles. *Journal of Physics B: Atomic, Molecular and Optical Physics*, 34(10):1953–1966, may 2001.

[52] J P Connerade and A M Lane. Interacting resonances in atomic spectroscopy. *Reports on Progress in Physics*, 51(11):1439–1478, nov 1988.

[53] T. F. Gallagher. Doubly excited states. *J. Opt. Soc. Am. B*, 4(5):794–804, May 1987.

[54] D. Studer, P. Dyrauf, P. Naubereit, R. Heinke, and K. Wendt. Resonance ionization spectroscopy in dysprosium. *Hyperfine Interactions*, 238(1):8, Dec 2016.

[55] G.K. Woodgate. *Elementary Atomic Structure.* Oxford University Press, Oxford, 2002.

[56] Christopher J. Foot. *Atomic Physics.* Oxford University Press, Oxford, 2005.

[57] Aage Bohr and V. F. Weisskopf. The influence of nuclear structure on the hyperfine structure of heavy elements. *Physical Review*, 77(1), 1950.

[58] D. L. Clark, M. E. Cage, and G. W. Greenlees. The hyperfine structure and hyperfine anomaly of 161Dy and 163Dy. *Physics Letters A*, 62(6), 1977.

[59] J. Ferch, W. Dankwort, and H. Gebauer. Hyperfine structure investigations in DyI with the atomic beam magnetic resonance method. *Physics Letters A*, 49(4):287–288, 1974.

[60] Wei Guo Jin, Takashi Wakui, Toshiaki Endo, Haruko Uematsu, Tatsuya Minowa, and Hidetsugu Katsuragawa. Specific Mass Shift in Gd I and Dy I. *Journal of the Physical Society of Japan*, 70(8):2316–2320, 2001.

[61] G. J. Zaal, W. Hogervorst, E. R. Eliel, K. A.H. Van Leeuwen, and J. Blok. A study of the spectrum of natural dysprosium with the laser-atomic-beam technique. I. Isotope shifts. *Journal of Physics B: Atomic and Molecular Physics*, 13(11), 1980.

[62] W.H. King. *Isotope Shifts in Atomic Spectra.* Springer Science, 1984.

[63] V. V. Flambaum, A. J. Geddes, and A. V. Viatkina. Isotope shift, nonlinearity of King plots, and the search for new particles. *Physical Review A*, 97(3), 2018.

[64] Julian C. Berengut, Dmitry Budker, Cédric Delaunay, Victor V. Flambaum, Claudia Frugiuele, Elina Fuchs, Christophe Grojean, Roni Harnik, Roee Ozeri, Gilad Perez, and Yotam Soreq. Probing New Long-Range Interactions by Isotope Shift Spectroscopy. *Physical Review Letters*, 120(9), 2018.

[65] Daniel Adam Steck. *Quantum and Atom Optics.* 2007.

[66] Bernhard Huber. *Coherent Rydberg dynamics and interaction above room temperature: The frozen gas regime and beyond.* PhD Thesis, University of Stuttgart, 2014.

[67] E. L. Lewis. Collisional relaxation of atomic excited states, line broadening and interatomic interactions. *Physics Reports*, 58(1):1–71, 1980.

[68] G. Lindblad. On the generators of quantum dynamical semigroups. *Communications in Mathematical Physics*, 48(2):119–130, Jun 1976.

[69] Thomas Baluktsian. *Rydberg interaction between thermal atoms: Van der Waals-type Rydberg-Rydberg interaction in a vapor cell experiment.* PhD Thesis, University of Stuttgart, 2013.

[70] Christian Tomschitz. *A photoionization scheme to create cold ionic impurities from Rydberg atoms.* Master Thesis, University of Stuttgart, 2018.

[71] Fabian Ripka. *A room-temperature single-photon source based on strongly interacting Rydberg atoms.* PhD Thesis, University of Stuttgart, 2018.

[72] Artur Skljarow. *Evanescent Two Photon Spectroscopy of Rubidium Atoms for Integrated Silicon Structures at Telecom Wavelength.* Master Thesis, University of Stuttgart, 2018.

[73] Drake (Ed.) Gordon W. F. *Springer Hanbook of Atomic, Molecular and Optical Physics.* Springer, 2006.

[74] Wolfgang Demtröder. *Laser Spectroscopy Vol. 2: Experimental techniques.* Springer, 2008.

[75] Wolfgang Demtröder. *Laser Spectroscopy Vol. 1: Basic Principles.* Springer, 2008.

[76] Matthias Schmitt. *High Resolution Laser Spectroscopy of Dysprosium.* Master Thesis, University of Stuttgart, 2012.

[77] Claude Cohen-Tannoudji and David Guery-Odelin. *Advances in atomic physics _ an overview.* World Scientific Publishing, 2011.

[78] Thomas Maier. *Interactions in a quantum gas of Dysprosium atoms.* PhD Thesis, University of Stuttgart, 2015.

[79] M.C. Saleh, B.E.A & Teich. *Fundamentals of photonics.* vol. 22 Wiley New York, 1991.

[80] Florian Gerhard Huber. *Site-resolved imaging with the Fermi-gas microscope.* Doctoral Dissertation, Harvard University, 2014.

[81] Yasuzi Suzaki and Atsushi Tachibana. Measurement of the micrometer sized radius of gaussian laser beam using the scanning knife edge. *Appl. Opt.*, 14(12):2809–2810, Dec 1975.

[82] James M. Supplee, Edward A. Whittaker, and Wilfried Lenth. Theoretical description of frequency modulation and wavelengthmodulation spectroscopy. *Appl. Opt.*, 33(27):6294–6302, 1994.

[83] H Li, J-F Wyart, O Dulieu, S Nascimbène, and M Lepers. Optical trapping of ultracold dysprosium atoms: transition probabilities, dynamic dipole polarizabilities and van der WaalsC6coefficients. *Journal of Physics B: Atomic, Molecular and Optical Physics*, 50(1):014005, dec 2016.

Acknowledgments

Here I would like to acknowledge all those who have made this thesis possible. In particular, I wish to thank:

- Prof. Dr. Tilman Pfau for giving me an opportunity to complete my master thesis in the Dysprosium lab. His passion towards physics and care for his students has always inspired me. I am thankful to him for introducing me to this fascinating field of atomic physics and especially for his guidance at a point during my thesis where I was wondering if I would be having anything at all to present to my readers.

- Prof. Dr. Jörg Wrachtrup for his assistance as my second adviser.

- The entire team of the Dysprosium experiment especially Jan-Niklas Schmidt, Fabian Böttcher and Dr. Mingyang Guo for introducing me to a variety of skills and patiently guiding me through the challenges that I have encountered during my thesis. These are the bunch of people who's help and support are the reason that the reader (apart from themselves, who also proofread this thesis) is interested in reading this work. It has been an immense learning experience for me from all of them. I would also like to thank Dr. Tim Langen for his insights and interaction during the seminar course.

- Clémence Briosne-Fréjaville and Pierre Bataille for the insightful discussion on shelving spectroscopy in Sr atoms, which has helped me in my work.

- The entire 5th Physics Institute for the wonderful working atmosphere especially the administrative staff for guiding me through the bureaucracy.

- All my teachers who have inspired me in my journey.

- My parents and my brother back home and the Sai family in Stuttgart away my home for their constant love and support and for all the wonderful time spent.

- Bhagwan Sri Sathya Sai Baba.